Dipl.-Phys. Berit Behnke

A Directed Search for Continuous Gravitational Waves from Unknown Isolated Neutron Stars at the Galactic Center

A Directed Search for Continuous Gravitational Waves from Unknown Isolated Neutron Stars at the Galactic Center

Dipl.-Phys. Berit Behnke

geboren am 13.06.1983
in Wolfenbüttel

2013

Eigenständigkeitserklärung

Hiermit versichere ich, dass ich die vorliegende Arbeit selbstständig verfasst und keine anderen als die angegebenen Hilfsmittel verwendet habe. Die Stellen, die anderen Werken wörtlich oder sinngemäß entnommen sind, sind als solche kenntlich gemacht. Ich versichere weiterhin, dass ich weder unmittelbar noch mittelbar geldwerte Leistungen für Vermittlungstätigkeiten oder für die inhaltliche Ausarbeitung der vorliegenden Arbeit erbracht habe. Ich bin damit einverstanden, dass die Dissertation einer Überprüfung der Einhaltung allgemein geltender wissenschaftlicher Standards unterzogen wird, insbesondere auch unter Verwendung elektronischer Datenverarbeitungsprogramme.

Ich versichere weiterhin, dass die Arbeit in gleicher oder ähnlicher Form noch keiner anderen Prüfungsbehörde vorgelegen hat. Die Promotionsordnung ist mir bekannt und mit einer Prüfung nach den Bestimmungen der Promotionsordnung bin ich einverstanden.

Berit Behnke
Hannover, April 2013

A Directed Search for Continuous Gravitational Waves from Unknown Isolated Neutron Stars at the Galactic Center

Zusammenfassung

Gravitationswellen gehören zu den zentralen Vorhersagen der Einstein'schen Allgemeinen Relativitätstheorie. Durch ihre direkte Messung könnten auf einzigartige Weise die treibenden Kräfte hochenergetischer, astrophysikalischer Ereignisse erforscht werden. Doch aufgrund ihrer schwachen Wechselwirkung mit Materie ist bisher kein solcher Nachweis gelungen.

Diese Arbeit präsentiert die bislang erste Suche nach kontinuierlichen Gravitationswellen von unbekannten Neutronensternen im Zentrum unserer Galaxie. Für die Suche wurden fast zwei Jahre Daten zweier LIGO Detektoren aus dem fünften Science Run ausgewertet. Das galaktische Zentrum wurde ausgewählt weil die hohe Anzahl vorhandener massereicher Sterne, die nach heutigen Kenntnissen die Vorgänger von Neutronensternen sind, einen Überfluss an Neutronensternen selbst im Zentrum der Galaxie verspricht.

Da dies eine blinde Suche ist muss ein enormer Parameterraum berücksichtigt werden. Dieser stellt die Hauptschwierigkeit dar: durch den großen Frequenzbereich und den entsprechenden Bereich in erster Ableitung ist die Sensitivität selbst für eine einzelne Himmelskoordinate durch die verfügbare Rechenleistung limitiert. Eine Optimalfilter-Suchtechnik über angemessen lange Beobachtungszeiten würde die beste Sensitivität erzielen, ist aber zur heutigen Zeit und in absehbarer Zukunft mit den verfügbaren Rechenkapazitäten nicht möglich. Daher wird eine Methode verwendet, bei der zunächst 630 einzelne, 11.5 Stunden lange Datensegmente kohärent analysiert werden. Im Anschluss werden die Einzelergebnisse inkohärent kombiniert. Dieser Vorgang ermöglicht es einen Gravitationswellenfrequenzbereich von 78 bis 496 Hz und einen Bereich in erster Ableitung, der definiert ist durch $\dot{f} = -f/200$ yr, abzudecken.

Es wurde kein Gravitationswellensignal entdeckt. Daher werden 90% Konfidenz-Obergrenzen auf die Gravitationswellenamplitude für Quellen im galaktischen Zentrum angegeben. Dies sind die bislang einschränkendsten existierenden Grenzen einer Suche nach kontinuierlichen Gravitationswellen mit einem derart großen Parameterraum.

Schlagworte: *Gravitationswellen, Datenanlyse, Galaktisches Zentrum*

A Directed Search for Continuous Gravitational Waves from Unknown Isolated Neutron Stars at the Galactic Center

Abstract

Gravitational waves are one of the key predictions of Einstein's Theory of General Relativity. Direct observation of gravitational waves would allow us to probe the engines for highly energetic astrophysical events. However, since gravitational waves interact very weakly with matter, there have been no direct observations to date.

In this work the results of a directed search for continuous gravitational waves from unknown, isolated neutron stars at the Galactic Center, performed on almost two years of data from the fifth Science Run from two LIGO detectors are presented. The Galactic Center is believed to host an abundance of neutron stars that is reflected by the high number of massive stars known to be present in this area. According to current evolutionary scenarios, massive stars are the progenitors of neutron stars.

The main obstacle is the enormous parameter space that has to be searched over. Even for known sky positions the search sensitivity is computationally limited, because a large range in frequency and one or more frequency derivatives has to be covered, depending on the age of the potential source. A coherent optimal matched filter search for realistically long observation times would gain the highest sensitivity, but is not computationally feasible at the present time, or in the foreseeable future. Therefore, one requires methods which are computationally inexpensive, at the cost of being somewhat less sensitive. The search uses a semi-coherent approach, coherently analyzing 630 segments, each spanning 11.5 hours, and then incoherently combining the results of the single segments. It covers gravitational wave frequencies in a range from 78 to 496 Hz and a range of first order spindown values corresponding to $\dot{f} = -f/200$ yr.

No gravitational waves were detected. Therefore, 90% confidence upper limits on the gravitational wave amplitude of sources at the Galactic Center are placed, which are the most constraining to date for a large-parameter-space search for continuous gravitational wave signals.

Keywords: *Gravitational Waves, Data Analysis, Galactic Center*

x

Acknowledgments

THIS WORK WOULD NOT HAVE BEEN POSSIBLE without the great help and support of a variety of people who contributed in many different ways.

First of all, I would like to express my deepest appreciation to Professor Bernard Schutz, the director of the Albert-Einstein-Institut and my doctorate supervisor, for the opportunity to work and learn in such an inspiring environment. It is most exciting to be part of a world's leading research group in gravitational wave physics at a time, so close to the first detection. I am proud to call him my supervisor and I appreciate all the opportunities he gave me. I thank the Max-Planck-Gesellschaft and the International Max Planck Research School for the support and the many opportunities to travel.

I owe special thanks to my closest scientific advisor, Dr. Maria Alessandra Papa, who offered her continuous advice and encouragement throughout the course of this research work and supported me in every possible way. I thank her for the systematic guidance and the patience and great effort she put into training me in the scientific field. Without her support I could not have overcome all obstacles and challenges that occurred during the last years.

I would like to give special thanks to the people who have agreed to referee this work: Professor Bruce Allen, Professor Graham Woan and Dr. Pia Astone.

The Continuous Waves working groups at the AEI and the LSC are stimulating work environments and I am grateful to be part of this. During numerous meetings "at home" and worldwide, a large number of people, who I can't possibly itemize, inspired me in various ways. I had the chance to learn from their experience, benefit from thought-provoking discussions, and obtain useful input and guidance.

Contents

Listing of Figures

Listing of Tables

UNTIL ONE IS COMMITTED, there is hesitancy, the chance to draw back. Concerning all acts of initiative, there is one elementary truth, the ignorance of which kills countless ideas and splendid plans: that the moment one definitely commits oneself, then providence moves too. All sorts of things occur to help one that would never otherwise have occurred. A whole stream of events issues from the decision, raising in one's favor all manner of unforeseen incidents and meetings and material assistance, which no man could have dreamed would have come his way. Whatever you can do, or dream you can do, begin it. Boldness has genius, power, and magic in it. Begin it now.

— by W.H. Murray, a Scottish mountaineer

All great achievements require time.

Maya Angelou

1

Introduction

For more than 50 years, scientists have been attempting to directly detect gravitational waves. Although the knowledge of their existence is the result of formal mathematical reasoning, different astrophysical scenarios have been developed to predict where these waves are emitted and indirect evidence of their existence could be achieved [119]. The best hope for detecting gravitational waves involves large masses moving with near-relativistic speeds and accelerations. Unlike the experiment Hertz did in 1888 to prove the existence of electromagnetic waves predicted by Maxwell, generating electromagnetic waves and detecting them instantly, laboratory generation of detectable gravitational waves is impossible.

In the past several years gravitational wave detectors have undergone major improvements in their sensitivity and duty factor. This is important because the sensitivity of the detectors is a limiting factor for the reach of gravitational wave searches. Another way to improve the sensitivity lies in the development of sophisticated analysis techniques to process the recorded data. The particulars of a specific analysis method depend critically on the expected waveform of the gravitational wave

signal.

This work is concerned with *continuous* gravitational waves, emitted by young, rapidly rotating neutron stars. The waveform of such waves is a nearly monochromatic sinusoid that changes frequency very slowly over time. These waves are emitted over long timescales, typically much longer than the observation time. One way in which a neutron star can emit continuous gravitational waves is if its shape deviates from axial symmetry, for example if it exhibits a small "mountain" on its surface. As the star spins, this generates a time-varying quadrupole moment of inertia which, in turn, generates gravitational waves.

A variety of searches for continuous gravitational waves from neutron stars have been performed. Some searches have aimed to detect signals from known objects [33], like the low-mass X-ray binary Scorpius X-1 [23, 24], the Cassiopeia A central compact object [7], and the Crab and Vela pulsars [12, 26, 28]. Besides the known objects, extensive all-sky searches have been performed in recent years [3, 16, 22, 25, 27, 29, 30]. This work presents the first directed search for continuous gravitational waves from unknown, isolated neutron stars at the Galactic Center. The term Galactic Center is used here as a synonym for the sky coordinates of Sagittarius A* (Sgr A*). Out of about 2000 known pulsars, five are located within ~ 240 pc of Sgr A*[77] of which three are within $\sim 24 \text{-} 36$ pc of Sgr A*[56]. The existence of these five pulsars supports the belief that the Galactic Center might harbor a large population of pulsars not apparent to radio surveys because of the dispersion of the radio signal by dust or ionized plasma along the line of sight. Current stellar evolutionary models predict that neutron stars are born in supernova explosions of massive stars [61]. At least three stellar clusters in the Galactic Center region contain massive stars, potential progenitors of neutron stars [56].

A primary obstacle in searches like the one presented in this work is the small amplitude of the putative gravitational wave signal. Long observation times of order months to years are required to detect a signal above the noise. When the frequency and frequency evolution of the potential objects are unknown, the parameter space to search is large. A coherent search that uses matched filtering of the data against single templates over long observation times and covering a large parameter space is computationally infeasible. To overcome this limitation, techniques have been developed to maximize the attainable sensitivity at fixed com-

puting cost. This search uses a *hierarchical search technique* [51, 97] consisting of a coherent step over short duration data segments, using a maximum-likelihood statistic [55, 76], that is then followed by an incoherent combination of the results from the coherent step [52]. This allows the analysis to cover a wide range of different signals, defined by the frequency and the frequency derivative (spindown). No other search for signals from unknown neutron stars has ever considered as large a range in spindown values as this search.

The large parameter space is one of the strengths of this search. Another strong point is the elaborate post-processing that allows one to consider candidates with significance values three standard deviations below the expectation value for pure Gaussian noise. A huge number of candidates is tested by a series of vetoes.

No search has yet resulted in the detection of a gravitational wave signal. However, the absence of a detection allows one to draw conclusions on the maximum possible strength of continuous gravitational waves from the searched population. The current most sensitive upper limit on the gravitational wave strain amplitude for sources in the direction of the Galactic Center comes from the all-sky searches and is (with 90% confidence) $h_0 = 7.6 \times 10^{-25}$ [3]. The search presented here improves the limits of [3] by about a factor of two and presents the most constraining upper limits ever set in a large parameter space search like this.

Outline

The outline of the thesis is as follows: the first chapters give a broad overview of the various aspects that, all together, provide the basis for a gravitational wave search. First, a brief description of gravitational waves in the Theory of General Relativity is given, followed by an introduction on neutron stars and pulsars and the Galactic Center (Chapter 2). Chapter 3 is an overview of gravitational wave detectors and their basic method of operation. The last of the introductory chapters illustrates the main principles of the data analysis methods, derives the detection statistic and presents the concept of the search technique used for this search (Chapter 4). In Chapter 5 the preparation of the search, the setup of the covered parameter space, and the selection of the data segments are presented. The various stages of post-processing and a coherent follow-up search are presented in Chapter 6. No can-

didate is confirmed by the follow-up. Therefore, 90% confidence upper limits are placed on the gravitational wave amplitude (Chapter 7). In subsequent Chapter 8 a thorough discussion of the implication of the fact that no second time derivative of the frequency was considered in this search is given. Finally, the results and their implications are discussed in Chapter 9.

*Poets say science takes away from the beauty of the stars –
mere globs of gas atoms. I, too, can see the stars on a desert
night, and feel them. But do I see less or more?*

Richard P. Feynman

2

Gravitational Waves

2.1 Gravitational Waves in General Relativity

The theoretical description of gravitational waves was first formulated by Albert Einstein with his development of the General Theory of Relativity (hereafter general relativity). Within this theory a new understanding of gravity in terms of a unity of space and time was born – *spacetime*. In general relativity mass and energy *curve* spacetime. While in Newton's theory the Earth orbits the Sun as a result of the gravitational force that the Sun exerts on the Earth, in Einstein's theory the mass of the Sun curves the spacetime and the Earth follows a straight trajectory along that curved spacetime [71]. And small fluctuations in spacetime curvature can propagate with the speed of light through otherwise empty space – gravitational waves.

In the following, a very brief description of the gravitational wave phenomenon in the context of general relativity shall be given. A detailed discussion can be found in the standard textbooks [71, 91, 108, 115, 118].

2.1.1   THE EINSTEIN EQUATION

One of the most fundamental concepts in the Special Theory of Relativity is the expression of the line interval (the distance) $\mathrm{d}s$ between two neighboring points in spacetime [53]:

$$\mathrm{d}s^2 = -c^2\mathrm{d}t^2 + \mathrm{d}x^2 + \mathrm{d}y^2 + \mathrm{d}z^2, \ \ \mathrm{or} \ \ \mathrm{d}s^2 = \eta_{\mu\nu}\mathrm{d}x^\mu\mathrm{d}x^\nu, \qquad (2.1)$$

where $\eta_{\mu\nu}$ is the it Minkowski metric which, expressed in Cartesian coordinates, has the form

$$\eta_{\mu\nu} = \begin{pmatrix} -1 & 0 & 0 & 0 \\ 0 & 1 & 0 & 0 \\ 0 & 0 & 1 & 0 \\ 0 & 0 & 0 & 1 \end{pmatrix}. \qquad (2.2)$$

This concept is carried over to general relativity with only one key difference: while in the Special Theory of Relativity the spacetime is flat (namely the spacetime described by the Minkowski metric), in general relativity the spacetime is curved in order to represent gravitation. The more general statement of the line element is then [106]:

$$\mathrm{d}s^2 = g_{\mu\nu}\mathrm{d}x^\mu\mathrm{d}x^\nu, \qquad (2.3)$$

where $g_{\mu\nu}$ represents a generic metric that keeps the information about the spacetime curvature. The relation between the curvature and the mass-energy distribution is described by the Einstein equation (with $c = 1$) [71]:

$$R_{\alpha\beta} - \frac{1}{2}g_{\alpha\beta}R = 8\pi G T_{\alpha\beta}. \qquad (2.4)$$

The Ricci curvature $R_{\alpha\beta}$ is a measure of local spacetime and the Ricci curvature scalar R is the trace of the Ricci curvature. The measure of energy density at the right hand side of the Einstein equation is the stress-energy tensor $T_{\alpha\beta}$.

2.1.2 GENERATION OF GRAVITATIONAL WAVES

The Einstein equation 2.4 comprises ten nonlinear, partial differential equations for ten metric coefficients, $g_{\alpha\beta}(x)$. There is not one general solution to these nonlinear equations, but a whole variety of possible and valid solutions for particular circumstances. However, it is possible to give complete solutions of the Einstein equation for spacetimes whose geometries differ only slightly from flat spacetime. In this *weak-field limit* the nonlinear Einstein equations can be approximated as linear equations. For a flat spacetime the metric is $g_{\alpha\beta} = \eta_{\alpha\beta}$. When the metric is close to flat it can be described by the Minkowski metric plus a small perturbation $h_{\alpha\beta}(x)$:

$$g_{\alpha\beta}(x) = \eta_{\alpha\beta} + h_{\alpha\beta}(x). \tag{2.5}$$

An adequate formulation of "small" is in this regard $|h_{\mu\nu}| \ll 1$. A major simplification for the calculation of the linearized Einstein equation can be achieved by a careful choice of the coordinates in which the equation is expressed. This freedom in the choice of coordinates is called *gauge* freedom. It can be shown that a metric as given by Equation 2.5 can be gauge transformed into:

$$h'_{\alpha\beta} = h_{\alpha\beta} - \partial_\alpha \xi_\beta - \partial_\beta \xi_\alpha, \tag{2.6}$$

which has the same form but new perturbations. The $\xi^\alpha(x)$ are arbitrary, but small functions which can be used to simplify the form of the transformed $h_{\alpha\beta}$. By keeping only first order terms in $h_{\alpha\beta}$ and applying the Lorentz gauge condition,

$$\partial_\beta h_\alpha^\beta(x) - \frac{1}{2}\partial_\alpha^\beta(x) = 0, \tag{2.7}$$

the Einstein equation takes the simple form:

$$\Box h_{\alpha\beta}(x) = 0, \tag{2.8}$$

where the d'Alembertian operator is defined as:

$$\Box = -\frac{\partial^2}{\partial t^2} + \nabla^2. \tag{2.9}$$

The solutions to Equation 2.8 are gravitational waves. It can be shown, assuming the wave vector k to lie along the z-axis and with the *transverse-traceless gauge*, that the most general solution of the linearized Einstein equation is:

$$h_{\alpha\beta}(x) = \begin{pmatrix} 0 & 0 & 0 & 0 \\ 0 & h_+ & h_\times & 0 \\ 0 & h_\times & -h_+ & 0 \\ 0 & 0 & 0 & 0 \end{pmatrix} e^{i(kz-\omega t)}, \qquad (2.10)$$

where $\omega = kc$ and where h_+ and $h_\times$ are constant amplitudes [103] which refer to two polarizations of the gravitational wave, the *plus-* and *cross*-polarization. Therefore, gravitational waves are solutions of the linearized Einstein equation, which represent transverse metric perturbations which propagate in vacuum at the speed of light.

2.1.3   The Effect of Gravitational Waves on Test Particles

To understand the effect of gravitational waves, consider a circle of free falling test masses in space. It can be shown that their interaction with a gravitational wave would manifest itself as a change in the relative distances between them. The two polarizations of a gravitational wave differ by a rotation of 45 degrees around the rotation axis. As a gravitational wave passes perpendicularly to the circle of test particles, it changes their position in the way it is shown in Figure 2.1.1. The area of the deformed ellipse is equal to that of the original circle. The shape of the deformation is independent of the size of the circle of test masses. Thus, the measure of the strength of a gravitational wave is the *relative* change in distance between the test particles which is expressed as the dimensionless *gravitational wave strain* $h(t)$:

$$h(t) = \frac{\delta L(t)}{L}, \qquad (2.11)$$

where L is the radius of the circle and $\delta L(t)$ is the imposed displacement due to the gravitational wave. The *gravitational wave amplitude* is then defined as twice the strain. As will be discussed in Chapter 3, gravitational wave detectors measure this change in distances, for example, through approximately freely hanging mirrors
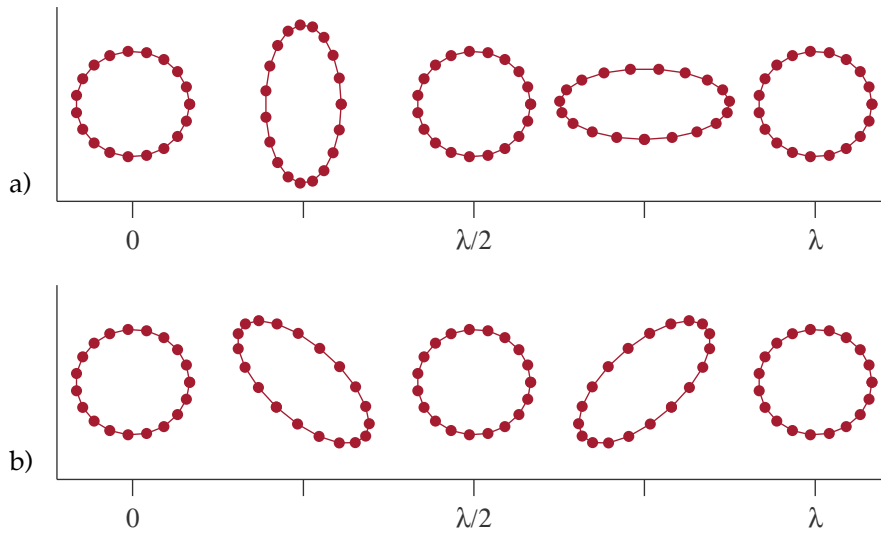
Figure 2.1.1: Illustration of the effect that a gravitational wave traveling in z-direction has on a circular ring of test particles in the (x, y)-plane. The circle of particles is stretched and compressed into ovals by the gravitational wave according to the two polarizations permitted by general relativity: (a) the plus-polarization and (b) the cross-polarization.

which are opposed to the displacement caused by a passing gravitational wave. A standing light wave between these mirrors experiences a phase shift proportional to the strength of the passing wave which can then be measured.

Gravitational waves are produced by accelerated mass quadrupoles Q. The amplitude of a gravitational wave is proportional to the second derivative of the mass quadrupole and inversely proportional to the distance r between the source and the observer [108]:

$$h \sim \frac{2G}{c^4} \frac{\ddot{Q}}{r},\qquad(2.12)$$

where G is the gravitational constant and c the speed of light. The first fraction at the right hand side of Equation 2.12 is of the order $1.7 \times 10^{-44}\,\mathrm{s^2/(kg\,m)}$, hence, extremely small. Therefore, large masses and accelerations are required to produce gravitational waves strong enough to be measurable. The only imaginable sources to produce gravitational waves that are detectable on Earth are astrophysical phenomena.

2.2   Gravitational Waves Sources

Possible sources to create gravitational waves strong enough to be measurable involve large masses and accelerations. The only imaginable phenomena are astrophysical phenomena, including for example binary star systems, supernovae, black holes, pulsars, and the relic stochastic background of gravitational waves from the Big Bang. It is useful to divide the anticipated gravitational waves into four broad categories [76, 112]: 1) long-lived and well defined, for example continuous waves, which are nearly sinusoids with frequencies that are more or less constant over times long compared to an observing run; 2) short-lived and well defined, for example coalescing binaries, whose signals are only measurable in the last seconds before the collision; 3) short-lived and a priori poorly known, like a supernova explosion; and 4) long-lived and stochastic, for example primordial gravitational waves from the Big Bang.

For the existing and upcoming terrestrial detectors, the most promising sources are those of the second category. Detectable event rates promise the first detection of a compact binary coalescence with the advanced LIGO and Virgo detector [103]. Future space-based detectors will be more sensitive at lower frequencies than terrestrial detectors. With such detectors even the coalescence of binary super-massive black holes, for example from galaxy mergers, should be detectable [105]. A different approach for the detection of gravitational waves is the use of pulsar timing arrays, which can potentially detect a stochastic astrophysical background from the superposition of signals from cosmologically distant super-massive black hole binary systems at very low frequencies [88].

We will concentrate only on signals in category 1) which are the target of this work. For a review of other emission mechanisms we refer the reader to a recent review [48].

The main source for the signals of category 1) are fast spinning neutron stars with a small deviation from axial symmetry. This is the kind of source this search aims to discover. Therefore, in the following sections the basic properties of neutron stars shall be presented.

2.2.1 Neutron Stars and Pulsars

Neutron stars are some of the best systems to observe the effects of general relativity. The first indirect evidence for gravitational waves was obtained in 1974 by studying the timing residuals of the binary pulsar PSR B1913+16 – and has brought the Nobel price to Russell Hulse and Joseph Taylor (1993). This search, too, is concerned with gravitational waves from (yet unknown) neutron stars and, therefore, a short introduction to this special class of stars shall be given below.

The first to anticipate neutron stars was Lev Landau in 1931 [82]. He suggested that *all stars heavier than* $1.5 M_\odot$ *certainly possess regions in which the laws of quantum mechanics (and therefore quantum statistics) are violated. [...] The density of matter becomes so great that atomic nuclei come in close contact, forming one gigantic nucleus.* Landau – without really knowing – described correctly the dense matter in neutron stars at a time when not even the neutron had been discovered. The first prediction of neutron stars followed only a year later, when Walter Baade and Fritz Zwicky proposed that in supernova explosions a huge amount of energy is released [42]: *With all reserve we advance the view that supernovae represent the transitions from ordinary stars to neutron stars, which in their final stages consist of extremely closely packed neutrons.* This is a precise description of the nature of supernova explosions. It took further 30 years from these predictions to the first discovery of a neutron star. The theoretical work during that time concentrated on four major lines of study [70]: 1) the construction of model *equation of state* (EOS) for dense matter; 2) theoretical predictions of superfluidity of neutron star interiors; 3) models for neutrino emission from stellar interiors due to the neutron star cooling; and 4) the thermal evolution of neutron stars. The discovery of the first cosmic X-ray source, Sco X-1 (in the Scorpius constellation), succeeded in 1962 [67] but it took five further years to identify Sco X-1 as an accreting neutron star. Shortly after Sco X-1, the Crab Nebula was discovered [50] and another year later, the first detection of a *rapidly rotating radio source* was published by Antony Hewish and Jocelyn Bell – the first pulsar, PSR B1919+21 [73]. Within ten months more than 100 articles explaining this new phenomenon had been published [121]. Finally, the idea that *pulsars are rotating magnetized neutron stars* [69] was established. Important was in this regard the discovery of the Crab pulsar and the understanding, that

pulsars are rapidly rotating neutron stars, with magnetic moments inclined with respect to their spin axis. The radio emission is beamed along the magnetic axis and, as the star rotates, the star is visible to observers only when this beam sweeps over the Earth. Since this scientific breakthrough the development of neutron star physics in both observations and theoretical models has grown immensely. In the following, a short description of today's knowledge about the main properties of neutron stars and pulsars is presented. These descriptions are heavily based on the treatment of [70].

Neutron Star Structure

Neutron stars are compact stars that contain matter of supranuclear density, which is assumed to consist of neutrons. The typical mass of a neutron star is $M \sim 1.4\,M_\odot$ and typical radii are $R \sim 10$ km. The density of the star is:

$$\overline{\rho} \simeq \frac{3M}{4\pi R^3} \simeq 7 \times 10^{14}\,\mathrm{g\,cm^{-3}} \sim (2\text{-}3)\rho_0, \qquad (2.13)$$

where $\rho_0 = 2.8 \times 10^{14}$ g cm^{-3} is the *normal nuclear density*, i.e. the density of nucleon matter in heavy atomic nuclei. In the center of the neutron star values up to $(10\text{-}20)\rho_0$ can be reached. This makes neutron stars the most compact stars known.

   The structure of a neutron star is illustrated in Figure 2.2.1. The outmost layer is the atmosphere. The spectrum of thermal electromagnetic neutron star radiation comes from this thin plasma layer. It contains information about the effective surface temperature, surface gravity, chemical composition, strength and geometry of the surface magnetic field, and the mass and radius of the neutron star. The thickness of the atmosphere varies from only a few millimeters in a cold star $(T_s \sim 3 \times 10^5$ K) to a few tens of centimeters in a hot star $(T_s \sim 3 \times 10^6$ K). Very cold neutron stars may even have a solid or liquid surface. Going towards the center, the next region is the outer crust. Its thickness is some hundred meters. It reaches densities at the base of $\rho_{ND} \sim 4 \times 10^{11}$ g cm^{-3} and its matter consists of ions and electrons. A very thin layer (of only a few meters) contains a non-degenerate electron gas, while in deeper layers the gas is almost ideal. Electrons,
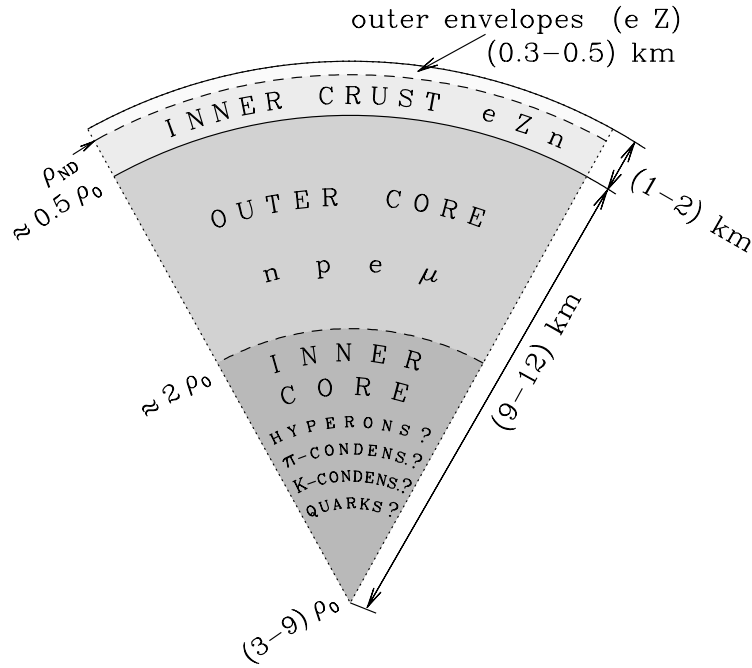
Figure 2.2.1: Schematic illustration of a neutron star. The explicit numbers vary strongly with the assumed model of the EOS. (Credit: [70])

free neutrons, and neutron-rich atomic nuclei form the inner crust, which can be about one kilometer thick. The density varies from ρ_{ND} to $\rho_0/2$ at the base. The several kilometers thick outer core consists of neutrons with several per cent additions of protons, electrons, and probably muons. The density ranges from $\rho_0/2$ at the upper boundary to $2\rho_0$ at the bottom. The inner core can also extend for a few kilometers. The density is generally $\rho \gtrsim 2\rho_0$ and can take values up to $(10$ - $15)\rho_0$ at the center. The composition and the resulting EOS of the inner core are very model dependent. Various hypotheses exist which predict different compositions, like the existence of hyperons, pions, kaons, or quark matter.

Current evolutionary scenarios predict that neutron stars are born in supernova explosions and are the final stage of stars with masses greater than four to eight times that of the Sun [61]. After these stars have finished burning their nuclear fuel, they undergo a gravitational collapse. This explosion blows off the outer layers of the star in an expanding shock wave, producing a supernova remnant. The central region of the star collapses under gravity so heavily that protons and electrons

combine to form neutrons and produce a neutron star. These events are usually called *type II supernova explosions* [75]. During the first several years after birth the neutron star remains hidden behind the expanding supernova; this prevents the observation of very young neutron stars. During the supernova explosion the emission of neutrinos can be detected. Very soon after the explosion (order of minutes) the flux is already too small to be observed. However, the loss of energy by the emission of neutrinos provides an efficient cooling mechanism of the new-born neutron star.

Neutron stars radiate in all bands of the electromagnetic spectrum. Electromagnetic radiation ranges from radio, infrared, optical, ultraviolet, and X-ray to gamma-ray spectral bands. Several ground- and space-based telescopes exist to observe in all spectral bands. Different oscillation modes can be present in a neutron star, including fundamental (f), pressure (p), gravity (g), and Rossby (r) modes (analogous to Rossby waves in the Earth's oceans) [90, 111]. Observations of these modes can provide insight in the internal structure of neutron stars [78]. Some modes can be unstable. This applies particularly to the r-modes [41, 84]. If the neutron star is rapidly rotating, it can lose axial symmetry and, as a result to this r-mode instability, emit a substantial amount of energy in gravitational waves.

PULSARS

Pulsars are rotating neutron stars which produce an emission in different spectral bands that propagates along the magnetic field. Due to a misalignment of the star's magnetic axis with respect to its spin axis it is possible that the beam of radiation crosses the Earth for short durations in a regular repetition. Pulses of radiation can be detected which gave that class of neutron stars its name. Most pulsars can be subdivided by their observed spectral range into *radio pulsars, X-ray pulsars*, and *gamma-ray pulsars*. The majority of known neutron stars belongs to the class of radio pulsars. The periods of all known pulsars as of today are between 11.78 - 1.40×10^{-3} s [89]. The average spin period of isolated pulsars is longer than that of binary pulsars. Pulsars with spin periods shorter than $30\,\mathrm{ms}$ are called *millisecond pulsars*. Due to the conversion of rotational kinetic energy into electromagnetic radiation (and possibly gravitational wave radiation), the pulsar

spins down. The spindown rate of all known pulsars is within $\sim 10^{-21}$ Hz/s and -3.86×10^{-8} Hz/s [89]. Some pulsars, mostly young ones, show sudden jumps of their spin frequencies, called *glitches*. Different models exist to explain and interpret pulsar glitches, but so far there is no definitive general understanding [83]. The same applies to random irregularities of the pulses, known as *pulsar timing noise* [54].

All known pulsars are located within our galaxy, the Large and Small Magellanic Clouds, and globular clusters [86]. Although many neutron stars are assumed to be born in binary systems, the majority is born as an *isolated* (meaning solitary) neutron star. The evolution differs dramatically between isolated and binary pulsars. The main factors that regulate the evolution are [70]: rotation, accretion, and the magnetic field. The evolution of pulsars is often described in a P-$\dot{P}$-*diagram*, where P is the spin period and $\dot{P}$ the time derivative of the spin period (Figure 2.2.2) as in a Hertzsprung-Russell-diagram for normal stars. Pulsars are born with short spin periods and high spindown values, hence, start their life in the upper left corner of the diagram. Due to the mentioned conversion of rotational energy into radiation, the star spins down and the spin periods become longer and longer. The star slowly moves to the lower right corner of the diagram. At some point it is believed that the pulsar reaches a point at which the rotation can not power the radio emission mechanism anymore. The star is no longer visible as a pulsar. This region in the P-$\dot{P}$-diagram is called the *death-line*. The typical lifetime of a pulsar before it becomes radio-invisible is $\sim 10^7$ yr [87].

2.2.2 THE EMISSION OF CONTINUOUS GRAVITATIONAL WAVES

Different mechanisms are predicted by which spinning neutron stars could emit detectable continuous gravitational waves: one possibility is that the star presents a small deviation from perfect axial symmetry because its crust broke up due to, for example, the cooling of the star [95] or because of a non-axisymmetric distribution of the magnetic field below the crust [122]. Continuous gravitational waves could furthermore be emitted through *r*-mode excitation [39, 47, 63, 94]. *r*-modes may be important in hot young neutron stars: gravitational radiation couples to these modes so strongly that the viscous forces present in such stars are not suffi-
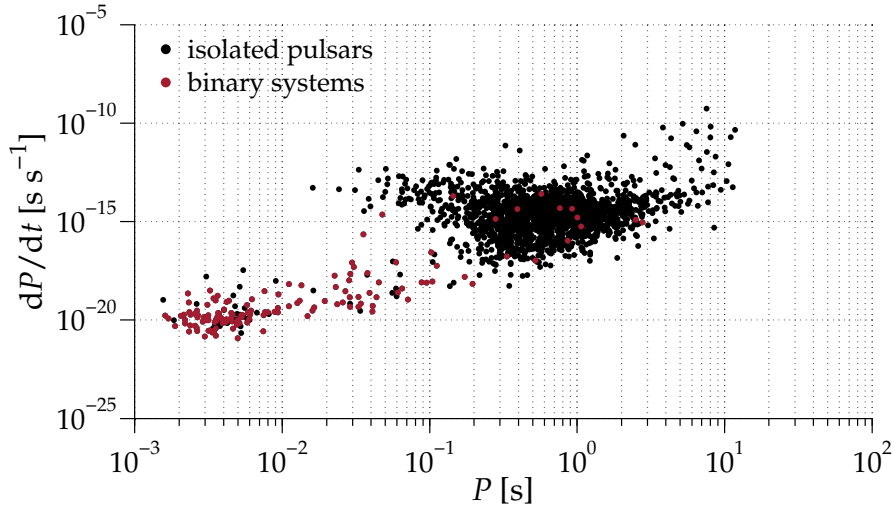
Figure 2.2.2: This plot shows all known pulsars as of today [89]. Black color denotes isolated pulsars, red color denotes binary systems. The majority of all pulsars is born as an isolated pulsar.

cient to suppress the gravitational radiation driven instability [94]. Gravitational radiation is therefore expected to carry away most of the angular momentum of hot young neutron stars [40]. In addition, binary neutron stars may experience non-axisymmetry from non-isotropic accretion [103].

2.3   THE GALACTIC CENTER

This section gives a very brief overview of the innermost region of the Galactic Center, followed by the explanation of why we believe that it is a promising target for our search.

Figure 2.3.1 shows two pictures of the central region around the strong radio source Sagittarius A. The image on the left hand side of Figure 2.3.1 spans $\sim 20\,\mathrm{pc}$ and was taken by the Chandra X-ray Observatory. It gives an overview of the three components of Sgr A: the largest of them is Sgr A East, a supernova remnant with an age of 100 - 5000 yr. The X-ray emission from Sgr A East is concentrated in the central $2 - 3$ pc within a 6×9 pc radio shell and offset about 2 pc from Sgr A* [43]. Sgr A West is a typical H II-region with a diameter of ~ 2 pc which lies (for an observer on the Earth) in front of Sgr A East. Its complex structure is shown in

the right hand side image of Figure 2.3.1, which is a 6 cm observation taken by the Very Large Array. Sgr A West consists of ionized gas and is called the *minispiral* for its morphology. It can be subdivided into three components, the Northern Arm, Western Arc and Eastern Arm (when looking at the image, the Eastern arm is the arm at the *left* from the center, while the Western Arc is the long structure that surrounds the center from the *right* to the bottom). The minispiral is surrounded by a thick ring called the *circumnuclear disk*. It extends no further than 7 pc and has a sharp inner edge at a radius of 1.5 pc [59]. Far infrared observations of the heated dust and the molecular lines in the radio band show that the circumnuclear disk is made up of molecular gas and dust and is inclined by about $\sim$ 20 - 25 degrees against the galactic plane. Matter within this disk is clumped together. Finally, the point source Sgr A* which has a diameter of 0.001 - 0.005 pc is *the* dynamical center of the Milky Way and is located at:

$$\text{RA}\,(2000) = 17^\text{h}45^\text{m}40^\text{s}.0409$$
$$\text{Dec}\,(2000) = -29°0'28''.118. \tag{2.14}$$

Within the inner $R \leq 0.38$ pc exists the *central cluster* which has a mass of 5×10^5 M$_\odot$. The innermost arcsecond centered on Sgr A* hosts a remarkable concentration of mainly B-stars, the so-called *S-star cluster*[1] [64]. Since the 1990s, observations have provided deep insight into the motion of the stars within these clusters [66]. Proper motions and even accelerations can be measured to high precision (±850 AU for the S-stars). The observed movements can be well explained with a gravitational field of a mass distribution which corresponds to that of the central cluster plus a central point source – the central black hole – with $M_0 = 4.4 \times 10^6$ M$_\odot$ [64].

---

[1]The naming of the *S-stars* originated in [58] to denote those remarkably fast moving stars in the *Sgr A*(IR)-cluster* that were known at that time. Since that time the number of S-stars has grown to over 200 [65, 68]; unfortunately, the MPE and UCLA groups have been using different nomenclature. (Cf. [64])
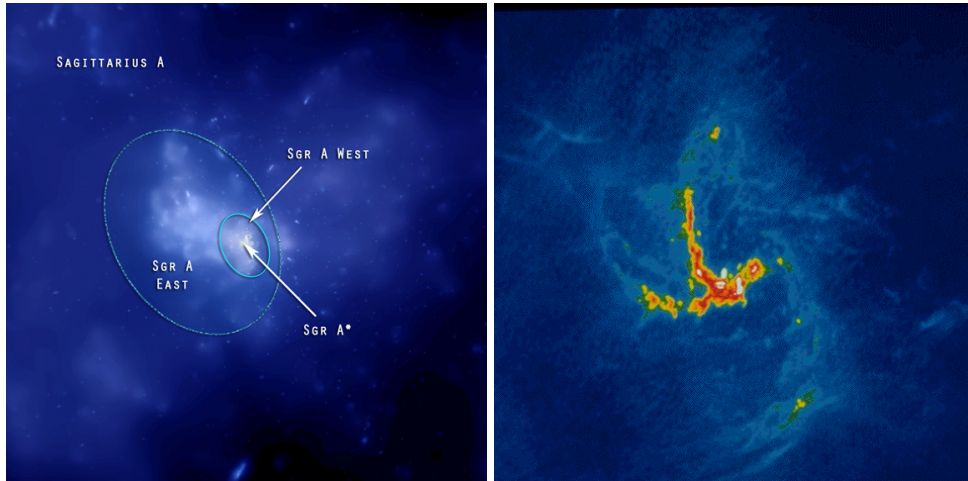
Figure 2.3.1: Left: X-ray observation of the three parts of Sgr A, the point source Sgr A* which is the dynamical center of the Galaxy, the HII-region Sgr A West which has the morphology of a minispiral, and the supernova remnant Sgr A East. The image is ~ 20 pc on a side. Right: The 6 cm image taken by the Very Large Array shows the spiral structure of Sgr A West. Credit: NASA/CXC/MIT/F.K.Baganoff et al. (left) and NRAO/AUI (right).

2.3.1   Pulsars at the Galactic Center

Rapidly rotating neutron stars with small deviations from perfect axial symmetry are the most promising sources for continuous gravitational wave emission. No search for gravitational waves from such sources, however, has resulted in a detection yet. A possible explanation is that the neutron stars we are looking for are of an unusual kind. Therefore, the most interesting regions are those that contain a large number of neutron stars. Among such a large population it might be possible to find a neutron star that is unusual enough to be emitting gravitational waves that are detectable.

The innermost Galactic Center area is believed to be such a region. Because it contains an overabundance of massive stars, it may well contain also a large number of neutron stars [77]. Massive stars are believed to be the progenitors of neutron stars: the star undergoes a supernova explosion and leaves behind the neutron star [61]. The wide Galactic Center area ($R \leq 200$ pc) contains more stars with initial masses above $100\,M_\odot$ than anywhere else known in the Galaxy plus three of the most massive young star clusters [62]. One of these is the central cluster,

which is concentrated around the center of the Galaxy and contains at least 80 massive stars [62]. The innermost 1 pc contains a dense, rich cluster of stars and a few supergiants [44], centered around Sgr A*. Among the brightest stars are 20 hot, massive supergiants with effective temperatures of 25000 K and luminosities $\leq 10^6$ L$_\odot$. These stars form a sub-group concentrated strongly towards the center. The other bright stars are > 200 K- and M-giants. The main fraction of the mass comes from a few 10^6 cool giants and dwarfs. The core radius of the entire central cluster is about 0.38 pc [114]. The formation of so many massive stars in the central parsec remains a mystery [62], but current estimates predict roughly as many pulsars within 0.02 pc distance to Sgr A* as there are massive stars [96]. Current estimates assume at least ~ 100 radio pulsars to be presently orbiting Sgr A* within this distance [96].

An experiment is a question which science poses to Nature,
and a measurement is the recording of Nature's answer.

<div align="right">Max Planck</div>

3

Gravitational Wave Detectors

The great challenge of detecting gravitational waves is to measure the extremely minute effect that gravitational waves have on the detector. The amplitude of gravitational waves falls off as the inverse of the distance from the source (see Equation 2.12). Therefore, even the strongest gravitational waves, produced for example by merging binary black holes, die out to very small amplitude by the time they reach the detector on Earth.

The first attempt to detect gravitational waves was done by Joseph Weber in the 1960s [117]. He used a large, solid piece of metal (colloquially known as a *Weber bar*, ~ 1 m diameter, 2 m length of aluminium) whose elastic modes would be excited by a passing gravitational wave. A transducer then converts the motion into a measured electrical signal. The high sensitivity band of a bar detector is very small and spans only a few tens of Hertz. Modern forms of the Weber bar are still in operation [38, 104], but are not sensitive enough to detect anything but extremely powerful gravitational waves.

A more sensitive instrument for gravitational wave detection is a laser interfer-

ometer with separate masses placed many hundreds of meters to several kilometers apart, acting as two ends of an imaginary bar. A passing gravitational wave stretches one arm and shortens the other by a tiny amount. If its travel path is along a vector standing orthogonal on the plane of the two detector arms, the detector responds in the most sensitive way. Several ground-based interferometers are in operation today, like Virgo, a 3-km-long gravitational wave detector in Cascina, Italy, GEO600, a 600-m-long gravitational wave detector in Hanover, Germany, and TAMA300, a gravitational wave detector located at the Mitaka campus of the National Astronomical Observatory of Japan. The currently most sensitive gravitational wave detectors are the two LIGO detectors at two separate observatory sites, in Livingston, Louisiana, and Hanford, Washington, respectively. LIGO was founded in 1992. Each observatory operates one of the two nearly identically designed interferometers which have two orthogonal 4-km-long light storage arms that keep the laser light inside the arm cavities for many round trips. This amplifies the effect of the gravitational wave and increases the sensitivity of the instruments. Upgrades to LIGO will increase the sensitivity further.

Plans for future gravitational wave detectors exist, like KaGra[1], which will be located in the Kamioka mine, Japan, and is expected to start its operation in 2018 [110], and for the operation of a third LIGO detector in India[2] [60]. The expansion of the gravitational wave detector network has significant scientific benefits: at fixed detection confidence the expected event rates will increase and source-localization accuracies will improve dramatically.

All detectors are limited at high frequencies by shot noise of the photons of the laser beam. If there are not enough photons arriving in a given time interval (that is, if the laser is not intense enough), it is impossible to tell whether a measurement is due to a gravitational wave, or just random fluctuations in the number of photons. At low frequencies all ground-based detectors are limited by seismic noise (earthquakes, large storms) as well as anthropogenic activities and must be very well isolated from those disturbances. For this and other reasons space-based gravitational wave detectors are under development as well. The *Laser Interferometer Space Antenna* (LISA) [109] will be able to detect gravitational waves at frequencies as low

---

[1]Website: http://gwcenter.icrr.u-tokyo.ac.jp/en/
[2]Website: http://www.gw-indigo.com
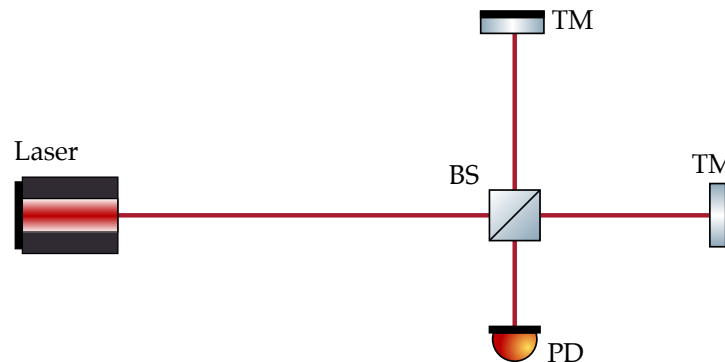
Figure 3.1.1: Schematic of a simple Michelson Interferometer. BS = beam splitter, PD = photo diode, TM = test mass.

as millihertz. The initial plans for LISA comprised three satellites with distances of about five million kilometers. LISA was a common project from the National Aeronautics Space Administration (NASA) and European Space Agency (ESA). Unfortunately, NASA had to put this mission on hold in 2011. The scientific team is proposing to ESA a reduced version of that observatory, possibly under a new name like *evolved LISA* (eLISA) or *New Gravitational Wave Observatory* (NGO).

3.1 THE BASIC CONCEPT OF FREE MASS INTERFEROMETERS

The basic Michelson interferometer (Figure 3.1.1) consists of two *test masses* (TM) which are installed at about a distance L far from a *beam splitter* (BS) along two perpendicular directions. In reality, of course, the mirrors that are used as test masses can not be completely free falling, but a very good approximation can be attained by hanging the mirrors as pendulums. The horizontal motion of the test masses is approximately free and this is the important motion, when the waves are reaching the detector perpendicular to the plane stretched by the two arms.

The following considerations are based on [106]. To analyze what happens when a gravitational wave impinges the interferometer, consider a beam of light, that travels from the laser to the beam splitter. At the beam splitter, one component of the incident light is reflected along one arm and the other is transmitted along the other arm. The light travels with the speed of light c and therefore the

time a wave front needs for the round trip from the beam splitter to one of the test masses and back is:

$$\tau = \frac{L}{c} + \frac{L}{c} = \frac{2L}{c}. \tag{3.1}$$

In this ideal interferometer the arms have the exact same length and the two beams arrive precisely at the same time back at the beam splitter. Now, consider a passing gravitational wave as a step function $h(t) = h_0 H(t - \tau)$, where h_0 is the amplitude of the wave and $H(t - \tau)$ is the unit step function commencing at the time τ. At the moment the gravitational wave arrives at the beam splitter the local spacetime is distorted by the gravitational wave, which produces a relative length change in the two arms: one detector arm is shortened, the other is lengthened. The gravitational wave also stretches the wave length of the laser light source accordingly. The change in the spacetime metric in the two arms is equal and opposite and therefore the travel time the light needs in each of the arms differs. This results in a difference between the arrival times:

$$\Delta\tau = h(t)\frac{2L}{c}. \tag{3.2}$$

where $h(t)$ is the dimensionless strain of the gravitational wave (see Section 2.1.3). In practice, the beam of light is made of coherent laser light and a phase shift of the interfering light is measured at the photo diode, which is dependent on the strength of the gravitational wave:

$$\Delta\Phi(t) = h(t)\frac{4\pi L}{\lambda}. \tag{3.3}$$

3.2   THE LIGO DETECTORS

Today, LIGO comprises two detectors, H1 and L1. At the time the data for this research was collected, a third, 2-km-long detector existed, co-located in the vacuum system of the 4-km-detector in Hanford, called H2. Both detectors are power-recycled Michelson interferometers with *Fabry-Perot arm cavities*. An arial picture of the LIGO Hanford observatory is shown in Figure 3.2.1. The two LIGO sites are about 3030 km apart, to minimize the occurrence of uncorrelated disturbances
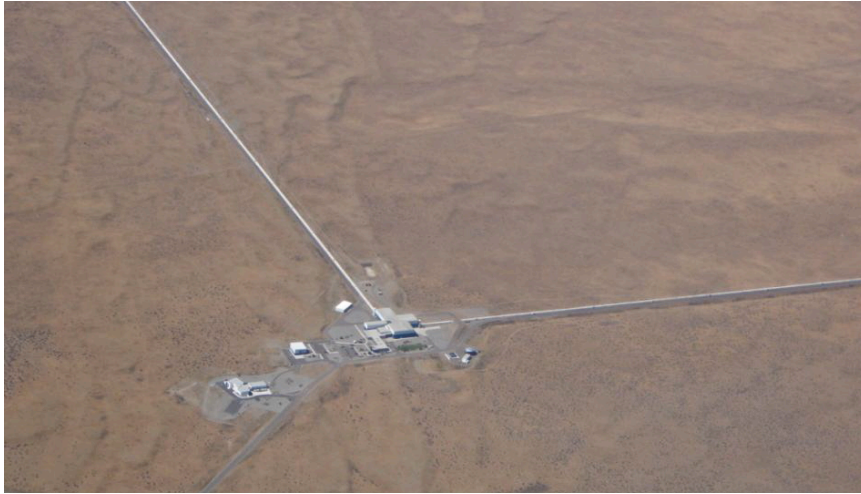
Figure 3.2.1: Aerial photograph of the LIGO Hanford Observatory. The site is located about 300 kilometers southeast of Seattle. The main central building hosts the *Laser Vacuum Equipment Area*: the origin of the beam tubes, the laser source, most of the optics, and the photo diodes.

which are mostly of local origin.

The time periods in which the detectors are focused on collecting science data, only interrupted by four hours weekly maintenance work, are called *Science Runs*. Until today, the LIGO detectors have performed six Science Runs. For this work data from the *fifth Science Run* (S5) has been used. During S5, over one year of science data coincident among all three detectors was recorded, with an average triple-interferometer duty factor of 52.5%.

3.2.1 Basic Operation Mode of a LIGO Interferometer

Figure 3.2.2 shows a schematic of the LIGO interferometers. The detectors have undergone multiple updates and major changes over the last years. The description of this work concentrates on the setup that was present during the fifth Science Run, because the data analyzed in this search was collected during that time. In the following, the main components of the interferometer are described by tracking the path of the laser light through the detector.

The source of the laser beam is a diode-pumped Nd:YAG laser. It emits a continuous wave laser beam of $10\,\mathrm{W}$ in a single frequency at the wavelength of $1064\,\mathrm{nm}$.

The *mode cleaner* (MC) is basically a 12 m long triangular transmissive cavity that improves the quality of the light. That is, it provides a stable, diffraction-limited beam, filters laser noise, and serves as an intermediate reference for frequency stabilization. The light in the resonator will reflect several times from the two plane mirrors and the spherical mirror. If $L = n\lambda$, where L is the distance from the mode cleaner mirror MC 1 to mirror MC 2 to MC 3 and back to MC 1, n is an integer and λ is the wavelength of the laser light, standing waves can build and a resonance will occur. Once the cavity is *locked* (i.e. digital servo loops are closed and the cavity is maintained on a fundamental mode resonance), the higher order modes of the resonator are not in resonance and are therefore strongly attenuated in transmission. As a consequence, only certain frequencies are sustained in the resonator and only the transversal electro-magnetic mode TEM_{00} passes through the last mirror MC 3. The transmission is therefore dependent on L and λ. After passing the mode cleaner, a Faraday isolator permits the light to pass through in only one direction, thus preventing back-reflections from reaching the laser.

In the *mode matching telescope* (MMT) the coupling between the Gaussian beam and the TEM_{00} mode of the interferometer is maximized by matching the parameters of the laser beam to the parameters of the interferometer. In addition to that, the beam is expanded in a way that it travels 4 km without diffracting beyond the size of the optic hanging at that distance from the beam splitter. MMT 3, the third and last optic of the mode matching telescope, is the mirror that directs the beam into the interferometer. After leaving the mode matching telescope, the laser is in its most stable state. All the optics it passed through so far are for intensity stabilization, widening of the beam and improvement of the beam quality. Before going through the beam splitter, the light passes the *recycling mirror* (RM). The optic prevents the light from being reflected back to the mode matching telescope and instead sends it back into the arm cavities, increasing the resonance within these cavities. This technique is known as *power recycling*.

As in a simple Michelson interferometer, the beam splitter is the origin of the two arms. The arm cavities are each made of two mirrors which act as the test masses. Each Fabry-Perot arm cavity contains an *input test mass* (ITM) and an *end test mass* (ETM). These test masses mark out coordinates in spacetime (see
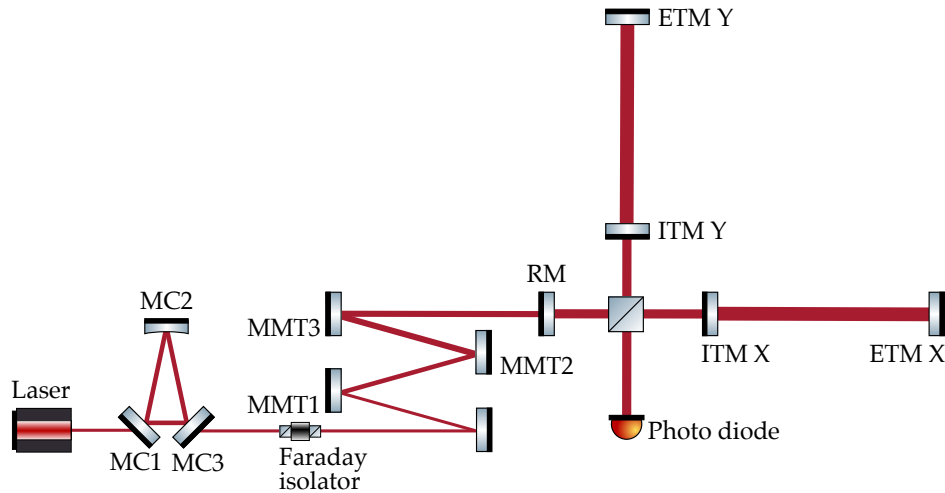
Figure 3.2.2: Schematic of the LIGO interferometers. The 10 W laser light is emitted at 1064 nm. Before the light enters the interferometer, the quality of the laser light is improved by the mode cleaner (MC), the beam is widened, and coupled to the TEM_{00} mode of the interferometer in the mode matching telescope (MMT). A Faraday isolator prevents the beam from being reflected back to the laser source. The beam splitter (BS) divides the beam in two halves, sending one half into the x-arm, the other half into the y-arm of the interferometer. Both parts reflect multiple times between the input test masses (ITM) and the end test masses (ETM). A recycling mirror (RM) couples light back into the interferometer Fabry-Perot cavity arms. The coherent sum of the promptly reflected beam, that bounces off the first mirror and never enters the cavity, and the leakage beam, which is the small part of the standing wave inside the cavity, that leaks back through the first mirror, is measured at the photo diode (PD). A gravitational wave signal would be noticed by a phase shift between the two beams.

Section 2.1). The input test masses are partially transmitting mirrors, the end test masses highly reflecting mirrors. In the arms, the light is retained for many round trips, leading to a magnification of the phase difference by about a factor of 100 for a gravitational wave with a frequency of 100 Hz. When the detector is in operation mode (the detector is in lock) an integer amount of half wavelengths is kept between the mirrors of the cavity. To keep the number of half wavelengths constant over a long time the optics need to be hold at very nearly the same distance. This is difficult because local noise sources cause a mirror motion and thus inject length noise into the interferometer, or can break the interferometer lock. In addition, the

laser frequency needs to be stable because servo controls keep the detector in lock by modulating the laser frequency. This technique is called the *Pound-Drever-Hall locking technique* [49, 57]: since the intensity of the reflected beam is symmetric about the resonance and, hence, does not provide a usable error signal, the anti-symmetric derivative of the reflected intensity must be used to lock the laser. The derivative can easily be measured by imposing small variations on the laser frequency. If the reflected beam is above resonance, the intensity is positive. If the laser's frequency is changed sinusoidally over a small range, the reflected intensity will also vary sinusoidally, in phase with the variation in frequency. Below resonance the derivative is negative. The reflected intensity will vary $180°$ out of phase from the frequency. On resonance the reflected intensity is at a minimum and a small frequency variation will produce no change in the reflected intensity. This method is used for multiple cavities in the instrument.

The test masses have a size of 25 cm diameter $\times$ 10 cm and their weight is 10.3 kg [36]. They are suspended as pendulums to be isolated from seismic noise and approximately free falling. Additionally, they are mounted on stacks of masses and strings for further noise suppression. Seismic noise is one of the main noise sources, limiting observations at frequencies below $\lesssim 40$ Hz. Servo loops control their position, pitch, and yaw motion through electromagnetic controllers that are installed on the suspension support structure to compensate for unwanted motion due to noise. Almost all optics, including the arm cavities, are embedded in an ultra high vacuum system with a pressure of about 10^{-9} Torr. This isolates the system from acoustical effects and limits the scattering of the beam on gas particles.

The beam that reflects back from the beam splitter to the *photo diode* (PD) is the coherent sum of the promptly reflected beam, that bounces off the first mirror and never enters the cavity, and a leakage beam, which is the small part of the standing wave inside the cavity, that leaks back through the first mirror, which is never perfectly reflecting. If the cavity is resonant, the promptly reflected beam and the leakage beam have the same amplitude and are exactly $180°$ out of phase. In this case the two beams interfere destructively and the totally reflected beam vanishes. In case a gravitational wave passes the interferometer, the cavity is not quite perfectly resonant. The phase shift will not allow destructive interference and can be measured at the photo diodes. Figure 3.2.3 shows a camera image of the anti-

Figure 3.2.3: This picture shows a camera image of the anti-symmetric port of the former 2-km-long detector at LIGO Hanford. The existence of a faint luminous spot is due to junk light, sidebands, and seismic noise.

symmetric port of H2. In case of a perfectly stable lock, perfect cavities, no junk light, and no seismic disturbances no light would be seen at the photo diodes and the image would be all dark.

3.2.2 THE SENSITIVITY OF THE LIGO DETECTORS

The LIGO detectors are designed to be sensitive to gravitational wave signals between ~ 40 Hz and ~ 7 kHz. Around ~ 150 Hz, where the detectors are most sensitive, the detectors have a differential strain noise approaching 10^{-23} Hz$^{-1/2}$. The main limitation at lower frequencies is, as mentioned above, seismic noise and at higher frequencies the main noise source is shot noise of the laser.

The sensitivity of a gravitational wave detector is determined by the power spectral density of its instrumental strain noise, normalized to an equivalent gravitational wave amplitude $h(t)$ [116]. This is the Fourier power spectrum of $h(t)$, usually indicated with $S_h(\nu)$. It is conventional to plot $h(\nu) = \sqrt{S_h(\nu)}$, which
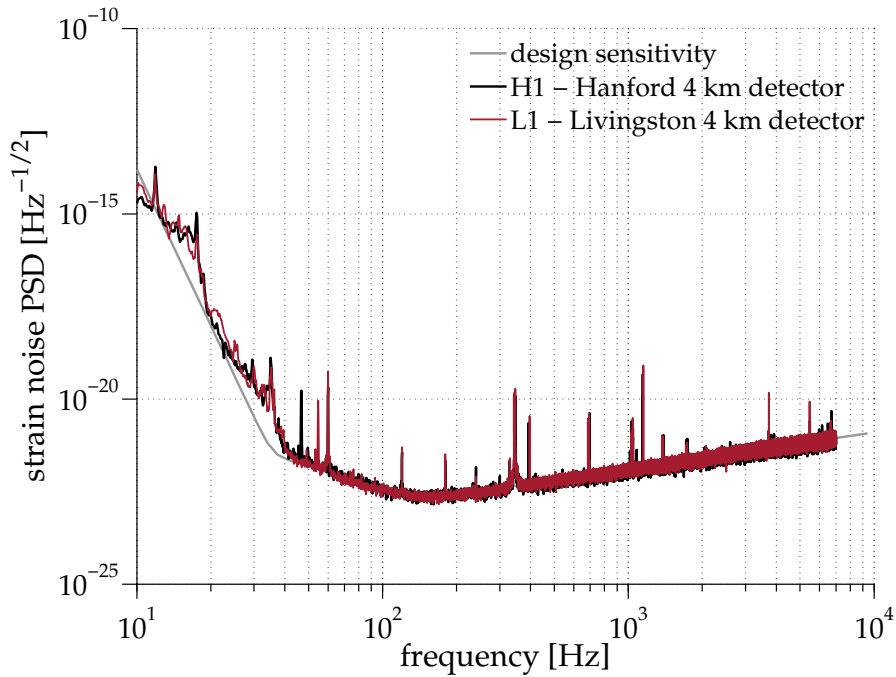
Figure 3.2.4: The plot shows the sensitivity curves of the LIGO detectors H1 and L1 during the fifth Science Run. Beneath the two curves the design sensitivity is shown as the gray line. The two detectors operated near their design sensitivities in almost the full frequency band.

allows to compare the noise with the signal's amplitude for a known signal bandwidth. The sensitivity curves of H1 and L1 during the fifth Science Run are compared to their initial design sensitivity in Figure 3.2.4[3]. It shows that the LIGO detectors during S5 were operated near their design sensitivity in almost the full frequency band.

---

[3]Source for the averaged power spectra data that was used to produce the plots is the website http://www.ligo.caltech.edu/~jzweizig/distribution/LSC_Data/.

The mathematician, carried along on his flood of symbols, dealing apparently with purely formal truths, may still reach results of endless importance for our description of the physical universe.

Karl Pearson

4

Search Methods

4.1 Detector Response to a Gravitational Wave

As discussed in Section 2.1, gravitational waves become measurable through the lengthening and shortening of spacetime, according to the two possible polarizations. To understand the detector response to a passing gravitational wave, consider the following setup of two different right-handed, orthonormal reference frames (see Figure 4.1.1): one, denoted by (x_d, y_d, z_d), is the detector reference frame. The unit vectors $\mathbf{n}_1$ and $\mathbf{n}_2$ point along the detector arms (x_d, y_d). The vector $\mathbf{z} = \mathbf{n}_1 \times \mathbf{n}_2$ stands orthogonal on the $\mathbf{n}_1$-$\mathbf{n}_2$-plane and points outwards from the surface of the Earth. The second reference frame is that of the gravitational wave source, (x_w, y_w, z_w), in which a gravitational wave would travel along the z_w-direction.

Assume that the length of the detector arms is much smaller than the reduced wavelength $\lambda/(2\pi)$ of the gravitational wave (what is called the *long wavelength*
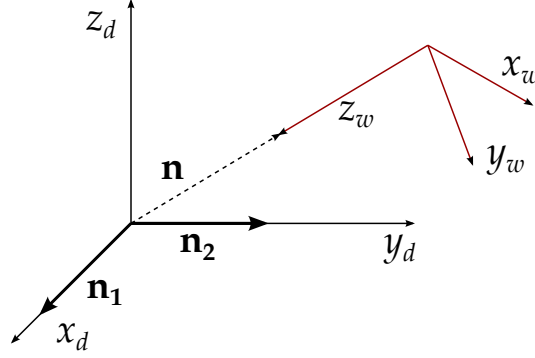
Figure 4.1.1: The plot shows the two reference frames: the detector frame (x_d, y_d, z_d), where the unit vectors $\mathbf{n_1}$ and $\mathbf{n_2}$ point along the detector arms, and the reference frame of the source, (x_w, y_w, z_w) (cf. [79]).

approximation). The relative length change of the two interferometer arms is the dimensionless response function $h(t)$ of the detector which can be written as [76]:

$$h(t) = \frac{1}{2}\mathbf{n_1} \cdot [\tilde{H}(t)\mathbf{n_1}] - \frac{1}{2}\mathbf{n_2} \cdot [\tilde{H}(t)\mathbf{n_2}], \tag{4.1}$$

where t is the time in the detector frame and $\tilde{H}$ is the three-dimensional matrix of the spatial metric perturbation, the gravitational wave, in the proper reference frame of the detector. It is given by

$$\tilde{H}(t) = M(t)H(t)M(t)^T, \tag{4.2}$$

where M is a three-dimensional orthogonal matrix which transforms the coordinates (x_w, y_w, z_w) of the gravitational wave reference frame to the coordinates (x_d, y_d, z_d) in the reference frame of the detector. T denotes matrix transposition. If the gravitational wave travels in the z_w-direction, then:

$$H = \begin{pmatrix} h_+(t) & h_\times(t) & 0 \\ h_\times(t) & -h_+(t) & 0 \\ 0 & 0 & 0 \end{pmatrix}, \tag{4.3}$$

where the functions h_+ and $h_\times$ describe the plus- and the cross-polarization (compare Figure 2.1.1) [91]. By combining the above equations it can be shown that

the response function $h(t)$ is linear in $h_+(t)$ and $h_\times(t)$:

$$h(t) = F_+(t)h_+(t) + F_\times(t)h_\times(t). \tag{4.4}$$

An arriving gravitational wave signal is amplitude-modulated by the varying sensitivity of the detector, as it rotates with the Earth and, hence, changes its orientation with respect to the source over time. This is expressed in the *antenna pattern functions*, $F_+(t)$ and $F_\times(t)$, which depend on the relative position of the detector and the source through **n** and on the polarization of the source with respect to the detector through ψ. The polarization angle ψ is the angle between the rotation axis of a star projected onto the sky sphere and the observer reference frame. The antenna pattern functions take values between $-1 \leq F_{+,\times} \leq 1$ and, because of the daily rotation of the Earth, they are periodic functions of time with a period equal to one sidereal day. It is possible to re-express them in terms of gravitational wave source coordinates, i.e. as a function of (α, δ, ψ), the right ascension, declination, and polarization angle. The complete coordinate transformation can be found in [76], which takes into account the angle between the detector arms ζ and the latitude of the detector site λ. The result is:

$$F_+ = \zeta \left(a(t)\cos(2\psi) + b(t)\sin(2\psi) \right), \tag{4.5}$$

$$F_\times = \zeta \left(b(t)\cos(2\psi) - a(t)\sin(2\psi) \right), \tag{4.6}$$

where $a(t)$ and $b(t)$ are defined as:

$$\begin{aligned}
a(t) = &\frac{1}{16}\sin 2\gamma(3 - \cos 2\lambda)(3 - \cos 2\delta)\cos[2(\alpha - \phi_r - \Omega_r t)] \\
&- 1/4\cos 2\gamma \sin \lambda(3 - \cos 2\delta)\sin[2(\alpha - \phi_r - \Omega_r t)] \\
&+ 1/4\sin 2\gamma \sin 2\lambda \sin 2\delta \cos[\alpha - \phi_r - \Omega_r t] \\
&- 1/2\cos 2\gamma \cos \lambda \sin 2\delta \sin[\alpha - \phi_r - \Omega_r t] \\
&+ 3/4\sin 2\gamma \cos^2 \lambda \cos^2 \delta,
\end{aligned} \tag{4.7}$$

and

$$\begin{aligned}
b(t) = &\cos 2\gamma \sin \lambda \sin \delta \cos[2(\alpha - \phi_r - \Omega_r t] \\
&+ 1/4 \sin 2\gamma (3 - \cos 2\lambda) \sin \delta \sin[2(\alpha - \phi_r - \Omega_r t)] \\
&+ \cos 2\gamma \cos \lambda \cos \delta \cos[\alpha - \phi_r - \Omega_r t] \\
&+ 1/2 \sin 2\gamma \sin 2\lambda \cos \delta \sin[\alpha - \phi_r - \Omega_r t].
\end{aligned} \qquad (4.8)$$

Ω_r is the angular velocity of the Earth due to its spin. The sum $\phi_r + \Omega_r t$ denotes the local sidereal time of the detector site, which is the angle between the local meridian and the vernal point. γ specifies the orientation of the detector arms with respect to local geographical directions: γ is measured counter-clockwise from East; its value indicates the direction that exactly bisects the two interferometer arms. This gives $h(t)$ in the gravitational wave source reference frame.

For a continuous gravitational wave signal the waveforms for the two polarizations $h_{+,\times}$ are given by [100]:

$$h_+(t) = A_+ \cos \Phi(t), \qquad (4.9)$$

$$h_\times(t) = A_\times \sin \Phi(t), \qquad (4.10)$$

with the two polarization amplitudes:

$$A_+ = \frac{1}{2} h_0 (1 + \cos^2 \iota), \qquad (4.11)$$

$$A_\times = h_0 \cos \iota. \qquad (4.12)$$

ι is the angle between the neutron star's spin axis and the line of sight, $-\mathbf{n}$, and h_0 is the characteristic gravitational wave amplitude at the detector.

The targeted sources of this search are isolated, rapidly spinning neutron stars with negligible proper motion and a deviation of their shape from perfect axial symmetry. The signal is an almost monochromatic sinusoid in the solar system barycenter frame (SSB). As the star emits gravitational waves, it loses angular momentum and, as a consequence, the star's intrinsic frequency decreases over time.

The time derivates of the frequency are given by:

$$f^{(s)} \equiv \frac{\mathrm{d}^{(s)} f}{\mathrm{d} t^{(s)}},\qquad (4.13)$$

with $s = 0$ indicating the frequency. If the star spins at rotational frequency ν, the gravitational waves are emitted at a frequency $f = 2\nu$. In addition to the amplitude-modulation will the signal at the detector be Doppler-shifted due to the orbital motion and rotation of the Earth. The phase of the signal is expected to be:

$$\Phi(\tau) = \phi_0 + \phi(\tau) = \phi_0 + 2\pi \sum_{s=0}^{s_{\mathrm{max}}} \frac{f^{(s)}(\tau)}{(s+1)!} \tau^{s+1},\qquad (4.14)$$

where s_{max} is the maximum spindown and τ is the arrival time of a wave front in the SSB that arrives at the time t at the detector:

$$\tau = t + \frac{\mathbf{n} \cdot \mathbf{r}}{c}.\qquad (4.15)$$

$\mathbf{r}$ denotes the vector pointing from the SSB to the detector position. Substituting Equation 4.15 into Equation 4.14 we obtain

$$\Phi(t) = \phi_0 + 2\pi \left[\sum_{s=0}^{s_{\mathrm{max}}} \frac{f^{(s)}(t)}{(s+1)!} t^{s+1} + \frac{\mathbf{n} \cdot \mathbf{r}}{c} \sum_{s=0} \frac{f^{(s)}(t)}{s!} t^{s} \right],\qquad (4.16)$$

the phase as a function of the detector time.

Combining the phase model and the antenna pattern functions, the final model of the gravitational wave signal can be written in the following form [76]:

$$h(t; \mathcal{A}, \boldsymbol{\lambda}) = \sum_{i=1}^{4} \mathcal{A}^i h_i(t; \boldsymbol{\lambda}),\qquad (4.17)$$

where $\boldsymbol{\lambda}$ denotes the set of Doppler-parameters, $\boldsymbol{\lambda} = \{f^{(s)}, \mathbf{n}\}$. The detector

dependent wave components $h_i(\alpha, \delta, f, f^{(s)}; t)$ are:

$$h_1(t; \boldsymbol{\lambda}) = a(t; \mathbf{n}) \cos \phi(t; \boldsymbol{\lambda}),$$
$$h_2(t; \boldsymbol{\lambda}) = b(t; \mathbf{n}) \cos \phi(t; \boldsymbol{\lambda}),$$
$$h_3(t; \boldsymbol{\lambda}) = a(t; \mathbf{n}) \sin \phi(t; \boldsymbol{\lambda}),$$
$$h_4(t; \boldsymbol{\lambda}) = b(t; \mathbf{n}) \sin \phi(t; \boldsymbol{\lambda}), \tag{4.18}$$

and the elements of the amplitude vector $\mathcal{A}^i$ are:

$$\mathcal{A}^1 = A_+ \cos \phi_0 \cos(2\psi) - A_\times \sin \phi_0 \sin(2\psi),$$
$$\mathcal{A}^2 = A_+ \cos \phi_0 \sin(2\psi) + A_\times \sin \phi_0 \cos(2\psi),$$
$$\mathcal{A}^3 = -A_+ \sin \phi_0 \cos(2\psi) - A_\times \cos \phi_0 \sin(2\psi),$$
$$\mathcal{A}^4 = -A_+ \sin \phi_0 \sin(2\psi) + A_\times \cos \phi_0 \cos(2\psi). \tag{4.19}$$

The main achievement is the separation of the Doppler parameters $\boldsymbol{\lambda}$ from the amplitude parameters $\mathcal{A}$ in the expression for the gravitational wave strain 4.17.

4.2   The Optimal Detection Statistic

The main challenge of gravitational wave data analysis is the the recovery of very weak signals from the noise. This is a common problem in various scientific fields and, over many years, different approaches to its solution have been developed. One of these approaches, the *frequentist* approach, is used in the following to frame the problem of the gravitational wave search in detector data.

The frequentist approach is based on hypothesis testing. In our case there exist two point hypotheses: the *null* hypothesis $\mathcal{H}_0$ is the hypothesis that no signal is present in the data $(h(t) = 0)$ and the *alternative* hypothesis $\mathcal{H}_1$ is the hypothesis that a signal $h(t)$ is present that adds to the noise:

$$\mathcal{H}_0 : x(t) = n(t) \qquad \text{no signal is present,} \tag{4.20}$$
$$\mathcal{H}_1 : x(t) = n(t) + h(t) \quad \text{a signal } h(t) \text{ is present.} \tag{4.21}$$

The decision between the two hypotheses is made through the construction of

a detection statistic $\Lambda(x)$ which is a function of the data $x(t)$: if $\Lambda(x) \geq \Lambda_{\text{thr}}$, for a given threshold Λ_{thr}, we decide for $\mathcal{H}_1$, and if $\Lambda(x) < \Lambda_{\text{thr}}$ we decide for $\mathcal{H}_0$. The *Neyman-Pearson-lemma* [92] states that when performing a hypothesis test between two point hypotheses the optimal detection statistic is the *likelihood-ratio-test* defined as:

$$\Lambda(x) = \frac{p_1\left(x;t\right)}{p_0\left(x;t\right)}. \tag{4.22}$$

Given a measured data stream $x(t)$, then $p_0\left(x;t\right)$ is the probability density function for the data if there is no signal present in the data and $p_1\left(x;t\right)$ is the probability density function for the data if a signal $h(t)$ is present and adds to the noise. If the noise is Gaussian with variance $\sigma^2 = 1$ and mean $\mu = 0$, $p_0\left(x;t\right)$ can be written as:

$$p_0\left(x;t\right) = \frac{1}{\sqrt{2\pi}} \exp\left[-\frac{1}{2}x(t)^2\right]. \tag{4.23}$$

The probability of observing data $x(t)$ in the presence of a signal is:

$$p_1\left(x;t\right) = \frac{1}{\sqrt{2\pi}} \exp\left[-\frac{1}{2}\big(x(t) - h(t)\big)^2\right]. \tag{4.24}$$

Inserting the two probabilities into 4.22 gives:

$$\Lambda(x) = \frac{p_1\left(x;t\right)}{p_0\left(x;t\right)} = \exp\left[-\frac{1}{2}h(t)^2 + x(t)h(t)\right]. \tag{4.25}$$

For simplicity, the logarithm of the likelihood function is used, hence:

$$\ln\Lambda(x) = x(t)h(t) - \frac{1}{2}h(t)^2. \tag{4.26}$$

Two important quantities are in this regard the false alarm probability, $\alpha(\Lambda_{\text{thr}})$, and the false dismissal probability, $\beta(\Lambda_{\text{thr}}, h; t)$. Both are shown in Figure 4.2.1. $\alpha(\Lambda_{\text{thr}})$ is the probability that the detection statistic $\Lambda(x)$ exceeds the threshold Λ_{thr} despite $\mathcal{H}_0$ being true:

$$\alpha(\Lambda_{\text{thr}}) = \int_{\Lambda_{\text{thr}}}^{\infty} p(\Lambda(x)|\mathcal{H}_0)\mathrm{d}\Lambda(x). \tag{4.27}$$

accept $\mathcal{H}_0$ | accept $\mathcal{H}_1$

$p(\Lambda(x)|\mathcal{H}_1)$

$p(\Lambda(x)|\mathcal{H}_0)$

β α

Λ_{th}
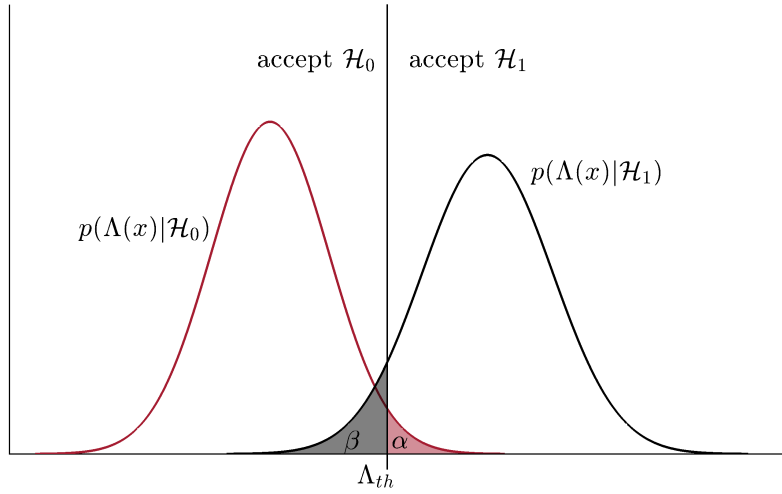
Figure 4.2.1: False alarm and false dismissal probabilities. The two curves show the probability density functions in the case of the acceptance of hypothesis $\mathcal{H}_0$ and $\mathcal{H}_1$, respectively. If the threshold Λ_{thr} is crossed, the hypothesis that a signal exists in the data is accepted. If hypothesis $\mathcal{H}_0$ is true, this assumption is wrong and the shaded red area shows the false alarm probability α. If a signal is present in the data there is still a chance to miss it because it does not cross Λ_{thr}. In this case the gray shaded area shows the false dismissal probability β.

In the same way, the false dismissal probability $\beta(\Lambda_{\mathrm{thr}}, h; t)$ of a signal $h(t)$ is defined as the probability that $\Lambda(x)$ does not cross the threshold Λ_{thr} even though $\mathcal{H}_1$ is true:

$$\beta(\Lambda_{\mathrm{thr}}, h; t) = \int_{-\infty}^{\Lambda_{\mathrm{thr}}} p(\Lambda(x)|\mathcal{H}_1)\mathrm{d}\Lambda(x). \tag{4.28}$$

Complementary to the false dismissal, the detection probability η is defined as:

$$\eta = 1 - \beta \ \ \text{or} \ \ \eta(\Lambda_{\mathrm{thr}}, h; t) = \int_{\Lambda_{\mathrm{thr}}}^{\infty} p(\Lambda(x)|\mathcal{H}_1)\mathrm{d}\Lambda(x). \tag{4.29}$$

In the following the application of this detection statistic to our problem is discussed.

4.3   THE $\mathcal{F}$-STATISTIC

In order to compute the log likelihood function 4.26 for out specific case the two distributions $p_0\,(x;t)$ and $p_1\,(x;t)$ must be known. However, $p_1\,(x;t)$ depends on both the Doppler and the amplitude parameters of the signal, which are unknown. In 1998, a way was found [76] to analytically maximize $\Lambda(x)$ over the amplitude parameters, producing a detection statistic that only depends on the Doppler parameters. In the following, their method and the main results, which are extensively used in our search, are briefly presented. The derivation is based on the treatment of [101]. Inserting the signal formulation of Equation 4.17 into the likelihood ratio $\ln \Lambda(x)$ of Equation 4.26 gives:

$$\ln \Lambda(x; \mathcal{A}, \boldsymbol{\lambda}) = (x|\mathcal{A}^a h_a) - \frac{1}{2}(\mathcal{A}^a h_a | \mathcal{A}^b h_b), \qquad (4.30)$$

where the scalar product is defined as:

$$(x|y) \equiv \frac{2}{S_n(f)} \int_0^{T_{\mathrm{obs}}} x(t)y(t)\mathrm{d}t. \qquad (4.31)$$

T_{obs} is the observation time and $S_n(f)$ is the single-sided power spectral density. The $\mathcal{A}$s depend neither on the detector properties nor on frequency or time. With the definition of the new variables:

$$H_a(\boldsymbol{\lambda}) = (x|h_a), \quad \mathcal{M}_{ab}(\boldsymbol{\lambda}) = (h_a|h_b), \qquad (4.32)$$

the detection statistic can be written as:

$$\ln \Lambda(x; \mathcal{A}, \boldsymbol{\lambda}) = \mathcal{A}^a H_a - \frac{1}{2}\mathcal{A}^a \mathcal{A}^b \mathcal{M}_{ab}. \qquad (4.33)$$

The next step is the maximization of $\ln \Lambda(x; \mathcal{A}, \boldsymbol{\lambda})$ over the amplitude parameters $\mathcal{A}$:

$$\left.\frac{\partial \ln \Lambda(x; \mathcal{A}, \boldsymbol{\lambda})}{\partial \mathcal{A}^a}\right|_{\mathcal{A}_{\mathrm{MLE}}} = 0, \qquad (4.34)$$

which results in:

$$H_a - \mathcal{A}^b_{\mathrm{MLE}}\mathcal{M}_{ab} = 0 \rightarrow \mathcal{A}^b_{\mathrm{MLE}} = (\mathcal{M}^{-1})^{ab}H_a. \tag{4.35}$$

The values of the A^a that are obtained when maximizing $\ln\Lambda(x;\mathcal{A},\boldsymbol{\lambda})$ are the *maximum likelihood estimators* (MLE) for the A^a. Combining 4.33 and 4.35 gives:

$$\ln\Lambda(x;\mathcal{A},\boldsymbol{\lambda})|_{\mathcal{A}_{\mathrm{MLE}}} = \mathcal{A}^a H_a - \frac{1}{2}\mathcal{A}^a\mathcal{A}^b\mathcal{M}_{ab}, \tag{4.36}$$

$$\mathcal{A}^a_{\mathrm{MLE}} = (\mathcal{M}^{-1})^{ab}H_b,$$

$$\mathcal{A}^b_{\mathrm{MLE}} = (\mathcal{M}^{-1})^{ab}H_a. \tag{4.37}$$

$$\ln\Lambda(x;\mathcal{A},\boldsymbol{\lambda})|_{\mathcal{A}_{\mathrm{MLE}}} = (\mathcal{M}^{-1})^{ab}H_b H_a - \frac{1}{2}(\mathcal{M}^{-1})^{ab}H_b(\mathcal{M}^{-1})^{ab}H_a(\mathcal{M})^{ab}$$

$$= \frac{1}{2}H_a(\mathcal{M}^{-1})^{ab}H_b. \tag{4.38}$$

The detection statistic that is used for this search, which is only dependent on the Doppler parameters $\boldsymbol{\lambda}$, is the so-called $\mathcal{F}$-statistic and is defined as the maximum logarithmic likelihood function:

$$\mathcal{F}(x;\boldsymbol{\lambda}) \equiv \ln\Lambda(x;\mathcal{A},\boldsymbol{\lambda})|_{\mathrm{MLE}} = \frac{1}{2}H_a(M^{-1})^{ab}H_b. \tag{4.39}$$

Because of its statistical properties one usually works with:

$$2\mathcal{F}(x;\boldsymbol{\lambda}) = H_a(\mathcal{M}^{-1})^{ab}H_b. \tag{4.40}$$

This formulation of the $\mathcal{F}$-statistic is commonly known as the $2\mathcal{F}$-*statistic*.

To find the expectation value of the $2\mathcal{F}$-statistic consider the case in which the Doppler parameters of the template $\boldsymbol{\lambda}$ are in perfect match with those of the signal $s(t)$ that is present in the data $x(t)$. The measured data can be described by:

$$x(t) = n(t) + s(t). \tag{4.41}$$

In this case Equation 4.32 takes the form:

$$H_a(\boldsymbol{\lambda}) = n_a(\boldsymbol{\lambda}) + s(\mathcal{A}, \boldsymbol{\lambda}), \tag{4.42}$$

with

$$n_a = (n|h_a) \quad \text{and} \quad s_a = (s|h_a). \tag{4.43}$$

Under the assumption of Gaussian noise the expectation value $\mathrm{E}[\ldots]$ takes the values:

$$\mathrm{E}[n_a] = 0 \quad \text{and} \quad \mathrm{E}[n_a n_b] = \mathcal{M}_{ab},$$
$$\mathrm{E}[x_a] = s_a \quad \text{and} \quad \mathrm{E}[x_a x_b] = \mathcal{M}_{ab} + s_a s_b. \tag{4.44}$$

That means, the four random variables x_a have a mean s_b and covariances $\mathcal{M}_{ab}$. The combination of Equation 4.44 with 4.40 gives the expectation value of the $2\mathcal{F}$-statistic:

$$\mathrm{E}[2\mathcal{F}] = 4 + \rho^2, \tag{4.45}$$

where the signal-to-noise ratio (SNR) ρ is given by

$$\rho^2 = s_a \mathcal{M}^{ab} s_b = \mathcal{A}^a \mathcal{M}_{ab} \mathcal{A}^b = (s|s). \tag{4.46}$$

The $2\mathcal{F}$-statistic can be written as the sum of the squares of four uncorrelated Gaussian variables. Therefore, the probability distribution of $2\mathcal{F}$ is a (non-central) χ^2-distribution with four degrees of freedom and, if a signal is present in the data, a non-centrality parameter λ:

$$\lambda = \rho^2. \tag{4.47}$$

4.4 THE STACK SLIDE SEARCH TECHNIQUE

The $2\mathcal{F}$-statistic is a matched-filter technique in which different templates are compared against the data. Templates are, in this regard, a number of different gravitational wave signals. If a gravitational wave signal is present in the data, the template with the best matching parameters will result in the highest $2\mathcal{F}$ value. In this search the targeted objects are unknown. That means, the parameters that define

the signal shape of the gravitational waves are unknown. Therefore, a large range of different values in frequency and spindown have to be considered, which results in a very large number of templates for which a $2\mathcal{F}$ value has to be computed. Performing such a search for realistically long observations times (of order months) is computationally infeasible. The $2\mathcal{F}$-statistic can, in this form, only be applied to problems in which the number of templates is limited or, equivalently, to searches that consider shorter observation times. A way to address this problem is to use a hierarchical search technique.

In a hierarchical search the data is divided into shorter duration segments (also called *stacks*) which are coherently analyzed and afterwards the results are incoherently combined. A *stack slide search* is a certain realization of this concept. In this method, which was first proposed by [51], the detection statistic values from the different segments are appropriately summed. This is somewhat less sensitive than a fully coherent search, but achieves the best sensitivity over a large parameter space at fixed computational cost.

In the approach used for this search (developed by [98]) the coherent analysis on the single segments is first performed on a coarse template grid. The combination of the results is then done on a refined template grid. At each fine grid point the final result is obtained by summing the $2\mathcal{F}$-statistic value determined at a suitable coarse grid point. The chosen coarse grid point can in principle be different in every segment and is the one that has the smallest metric separation to the fine grid point. Following the approach of [98] and taking into account that this search does not include different sky templates, the metric separation takes the simple form:

$$\frac{\mathrm{d}s^2}{\pi^2} = \frac{\mathrm{d}\nu^2 T_{\text{seg}}^2}{3} + \frac{\gamma^2 \mathrm{d}\dot{\nu}^2 T_{\text{seg}}^4}{180}, \tag{4.48}$$

where T_{seg} is the length of the single data segments and ν and $\dot{\nu}$ are defined as:

$$\nu(t) = f(t) + f(t)\frac{\mathbf{n} \cdot \dot{\mathbf{r}}}{c} + \dot{f}\frac{\mathbf{n} \cdot \mathbf{r}}{c},$$
$$\dot{\nu}(t) = \dot{f} + f(t)\frac{\mathbf{n} \cdot \ddot{\mathbf{r}}}{c} + 2\dot{f}\frac{\mathbf{n} \cdot \dot{\mathbf{r}}}{c}, \tag{4.49}$$

where $f(t) \equiv f(t_0) + (t - t_0)\dot{f}$, $t_0 = 1/N_{\text{seg}} \times \sum_{j=1}^{N_{\text{seg}}} t_j$ is the fiducial time,

and t_j is the detector time midpoint of segment j. N_{seg} is the number of data segments. The quantities $\nu(t)$ and $\dot{\nu}(t)$ can be interpreted as the source's instantaneous frequency and frequency derivative at the Earth's barycenter at time t. The incoherent combination of the results from the coherent analyses of the single data segments can then be done on a fine grid in the new coordinates. The spacing of the fine grid is determined from the metric for the fractional loss (*mismatch*) of the expected $2\mathcal{F}_{\text{sum}} = \sum_{j=1}^{N_{\text{seg}}} 2\mathcal{F}_j$ that results from offsets between the parameters of the template and the gravitational wave signal. It turns out that no refinement in frequency is necessary. The refinement in spindown is:

$$\gamma = \sqrt{1 + \frac{60 \sum_{j=1}^{N_{\text{seg}}} (t_j - t_0)^2}{N_{\text{seg}} T_{\text{seg}}^2}}. \tag{4.50}$$

The final result of the used search algorithm is the average of the single-segment $2\mathcal{F}$ values over the total number of data segments N_{seg}:

$$\langle 2\mathcal{F} \rangle \equiv \frac{\sum_{j=1}^{N_{\text{seg}}} 2\mathcal{F}_j}{N_{\text{seg}}}. \tag{4.51}$$

The combination of the template parameters and the resulting $\langle 2\mathcal{F} \rangle$ value is called a *candidate*.

The resulting $\langle 2\mathcal{F} \rangle$ value of a template depends on the mismatch between the template parameters and the parameters of the putative gravitational wave signal. Depending on how coarse (or fine) the template grid is, the search setup has a certain average mismatch. The average mismatch of this search is computed with an injection study (see Section 5.6) and is $\sim 15\%$.

Having chosen the analysis technique, the next step is to set up the searched parameter space.

The future depends on what we do in the present.

<div align="right">Mahatma Ghandi</div>

5

Setting up the Search

The goal of this search is to find gravitational wave signals from isolated, spinning, non-axisymmetric, and yet unknown neutron stars at the Galactic Center. We use a single sky template at the coordinates of Sgr A* and explicitly search over the remaining parameters of the gravitational wave signal, frequency and spindown, with a stack slide method (see Section 4.4).

In this chapter the setup of the search is defined. This is a non-trivial challenge, because the setup has to satisfy different constraints at the same time: it must cover an astrophysically interesting parameter space, yield a sensitivity that enables the detection of continuous gravitational wave signals, and be doable with available computational resources. A setup that contains long data segments will, in principle, yield a good sensitivity, but the length and number of the data segments are limited by the available computational resources. Large negative spindown values are associated with younger neutron stars that emit stronger gravitational wave signals and, hence, are easier to detect, but a large number of templates dramatically increases the computation time. This problem is solved by considering a variety of

different search setups and choosing the one that results in the best sensitivity for the given constraints.

5.1   THE ESTIMATED SEARCH SENSITIVITY

Among the parameters that determine the search sensitivity are the segment length T_{seg} and the number of the data segments N_{seg}. T_{seg} is the time spanned by a data segment: each segment contains at most T_{seg} seconds of data from each detector. It might well be that there is even less data in a segment, due to gaps in the detector output. The sensitivity estimate, however, is made with the assumption that there are no gaps in the data.

Following the estimate of the sensitivity for stack slide methods [79], the sensitivity of a this search is estimated with:

$$h_0^{\text{search}} = \frac{30}{N_{\text{seg}}^{(1/4)}} \sqrt{\frac{S_n}{N_{\text{det}} T_{\text{seg}}}}. \qquad (5.1)$$

where S_n is the single-sided power spectral density and N_{det} is the number of detectors from which data is analyzed which, in this search, is two.

5.2   THE SPINDOWN UPPER LIMIT

To determine if a chosen setup leads to a sensitivity good enough to detect gravitational wave signals the estimated search sensitivity is compared with the expected strength of a neutron star signal. Indirect limits on the strength of the gravitational wave emission from a non-axisymmetric, rapidly-rotating neutron star can be obtained under the assumption that the observed loss in rotational energy is entirely due to gravitational wave emission (see, for example [21]):

$$\frac{\mathrm{d}}{\mathrm{d}t} E_{\text{GW}} = \frac{32}{5} \frac{G}{c^5} I_{\text{zz}}^2 \epsilon^2 \left(\pi f\right)^6 \leq -\frac{\mathrm{d}}{\mathrm{d}t} E_{\text{ROT}} = -\frac{\mathrm{d}}{\mathrm{d}t} (2\pi^2 \nu^2 I_{\text{zz}}), \qquad (5.2)$$

where f is the gravitational wave frequency and ν is the neutron star's rotation frequency. Equation 5.2 assumes that the star rotates about its principal moment of inertia axis in the z-direction, I_{zz}. The equatorial ellipticity ϵ of the pulsar is the

fractional difference in moments of inertia:

$$\epsilon = \frac{I_{\mathrm{xx}} - I_{\mathrm{yy}}}{I_{\mathrm{zz}}}.$$ (5.3)

Solving Equation 5.2 (and taking the gravitational wave frequency to be twice the star's rotation frequency $f = 2\nu$) results in

$$\epsilon^{\text{upper limit}} = \sqrt{\frac{5}{32\pi^4} \frac{c^5}{GI_{\mathrm{zz}}} \frac{-\dot{f}}{f^5}}.$$ (5.4)

Equation 5.4 gives the ellipticity necessary for all the loss in rotational energy to go into gravitational wave emission. In general, however, other energy loss mechanisms might be at work in the star and $\epsilon < \epsilon^{\text{upper limit}}$.

Substituting Equation 5.4 in the expression of the gravitational wave amplitude of a neutron star signal (see, for example [76]),

$$h_0 = \frac{4\pi^2 G}{c^4} \frac{I_{zz} f^2}{r} \epsilon,$$ (5.5)

gives:

$$h_0^{\text{indirect upper limit}} = \frac{1}{r} \sqrt{\frac{5}{2} \frac{GI_{\mathrm{zz}}}{c^3} \frac{-\dot{f}}{f}}.$$ (5.6)

$h_0^{\text{indirect upper limit}}$ is the maximum expected strength of a gravitational wave emitted from a star at distance r from the Earth. As will be shown in the next section, the largest value that $h_0^{\text{indirect upper limit}}$ can take over the searched parameter space is:

$$h_0^{\text{indirect upper limit}} = \frac{1}{r} \sqrt{\frac{5}{2} \frac{GI_{\mathrm{zz}}}{c^3} \frac{1}{200 \, \mathrm{yr}}}.$$ (5.7)

5.3 THE SEARCHED SPINDOWN RANGE

The standard model for the frequency evolution of neutron stars is:

$$-\dot{f} = \frac{f}{\tau \langle n - 1 \rangle},$$ (5.8)

where n is the braking index and τ the spindown age. The braking index defines what emission mechanism is responsible for the energy loss measured through the spindown: $n = 3$ for electromagnetic radiation, $n = 5$ for gravitational wave radiation. The angled brackets denote that the braking index is averaged over the spindown age τ. Taking the average value of the braking index means that we don't require the instantaneous and the average value of n to be the same. The dominant emission mechanism of the targeted star could have changed over the star's lifetime. Therefore, different combinations of n and τ can yield the observed spindown. We use this model to set the spindown search range:

$$\frac{f}{\tau \langle n_{\mathrm{max}} - 1 \rangle} \leq -\dot{f} \leq \frac{f}{\tau \langle n_{\mathrm{min}} - 1 \rangle}. \tag{5.9}$$

with $n_{\mathrm{max}} = 5$ and $n_{\mathrm{min}} = 2$ (n_{min} is chosen to be smaller than 3 because all reliably measured braking indices are < 3). Rather than limiting the spindown at low values of $|\dot{f}|$ we increase the range in order to cover an as broad parameter space as possible and define the searched spindown range to start at $0\,\mathrm{Hz/s}$:

$$0\,\mathrm{Hz/s} \leq -\dot{f} \leq \frac{f_{\mathrm{max}}}{\tau \langle n_{\mathrm{min}} - 1 \rangle}. \tag{5.10}$$

Based on the computational feasibility of the search, as will be shown in the next section, we set:

$$\langle n_{\mathrm{min}} - 1 \rangle \tau = 200\,\mathrm{yr}. \tag{5.11}$$

Since $\langle n_{\mathrm{min}} - 1 \rangle \tau = 200\,\mathrm{yr}$ is constant for the targeted star population, larger spindown values are required at higher frequencies. This is implemented by dividing the total parameter space into smaller frequency bands and corresponding spindown ranges. The minimum spindown of each sub-band is set to zero and the maximum spindown value is derived from Equations 5.10 and 5.11, which results in the spindown range:

$$0\,\mathrm{Hz/s} \leq \dot{f} \leq -\frac{f_{\mathrm{max}}^{\mathrm{sub\text{-}band}}}{200\,\mathrm{yr}}. \tag{5.12}$$

With this setup the highest spindown value covered at $496\,\mathrm{Hz}$ is $\dot{f} = -7.86 \times$
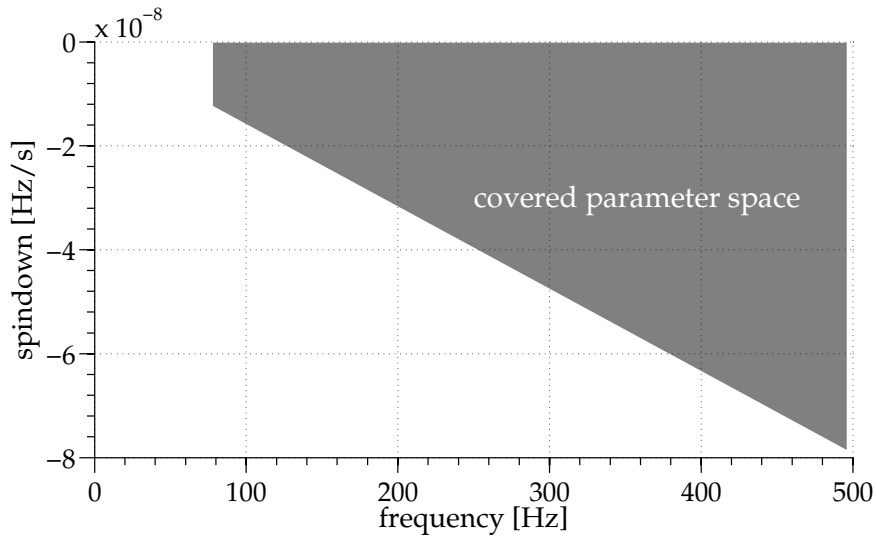
Figure 5.3.1: The plot shows the covered parameter range in frequency and spindown. The total parameter space is divided into smaller sub-spaces, each covering a certain frequency band and the corresponding spindown range. The first sub-band starts at 78 Hz and covers a spindown range of -1.25×10^{-8} Hz/s $\leq \dot{f} \leq 0$ Hz/s. The last sub-band ends with the last frequency at 496 Hz and covers a spindown range of -7.86×10^{-8} Hz/s $\leq \dot{f} \leq 0$ Hz/s.

10^{-8} Hz/s. Figure 5.3.1 illustrates the covered parameter space in frequency and spindown. The details about the exact partitioning will be given in Section 5.7, after the data segments have been selected and the template grid has been defined.

5.4 THE RESULTING SETUP

The expected search sensitivity (Equation 5.1) is now used together with the indirect limit on the maximum signal strength (Equation 5.6) to find the most sensitive search setup for a given search parameter space and computational resources. The setup is determined by the number N_{seg} and length T_{seg} of the data segments, the number of detectors N_{det} and the covered spindown range defined through $\langle n_{\text{min}} - 1 \rangle \tau$.

First, a decision is made in favor of using data from two different detectors. Provided that the detector noise floors are comparable, which is the case for the

two detectors chosen, using data from multiple detectors increases the sensitivity of the search. Besides the sensitivity improvement, taking data from more than one detector is useful at a later stage when separating real gravitational wave candidates from disturbances (see Section 6.3). To set the remaining parameters, a large number of different possible combinations of T_{seg}, N_{seg} and $\langle n_{\text{min}} - 1 \rangle \tau$ are chosen, and the computation time and search sensitivity are estimated. The range of tested parameter values is $T_{\text{seg}} = 10\,\text{h} \ldots 24\,\text{h}$, $N_{\text{seg}} = 340 \ldots 730$, and $\langle n_{\text{min}} - 1 \rangle \tau = 100\,\text{yr} \ldots 400\,\text{yr}$. Only combinations that lead to a total computation time of about two weeks, distributed over 1000 nodes of the ATLAS compute cluster are considered. Among the setups that satisfy this requirement the ones with the smallest $\langle n_{\text{min}} - 1 \rangle \tau$ is chosen (which is $\langle n_{\text{min}} - 1 \rangle \tau = 200\,\text{yr}$) and from those setups, again, the most sensitive one is identified. The resulting combination of parameters is $N_{\text{seg}} = 630$ segments, $T_{\text{seg}} = 11\,\text{h}$ and $\langle n_{\text{min}} - 1 \rangle \tau = 200\,\text{yr}$. The frequency range to cover is then the range where the estimated search sensitivity is lower than the indirect upper limit, $h_0^{\text{search}} \leq h_0^{\text{indirect upper limit}}$. This results in a frequency range with $f_{\text{min}} = 78\,\text{Hz}$ and $f_{\text{max}} = 485\,\text{Hz}$. Due to a mistake in the preparation of the data files the length of the segments was inadvertently increased to $11.5\,\text{h}$. This has a minor, positive impact on the search sensitivity while increasing the computational cost by an acceptable amount. Because of the improved sensitivity, the frequency range is slightly adjusted to cover frequencies up to $f_{\text{max}} = 496\,\text{Hz}$. f_{min} remains unchanged. Both sensitivity estimates and the expected signal strength in the spindown limit are shown in Figure 5.4.1. The final

N_{DET}	$\langle n_{\text{MIN}} - 1 \rangle \tau$	N_{SEG}	T_{SEG}	COMP. TIME	$h_0^{\text{IND. UL}}$@$150\,\text{Hz}$
2	200 yr	630	11.5 h	16.3 d	6.24×10^{-25}

Table 5.4.1: Summary of the search setup. The frequency band to cover is obtained by comparing the expected search sensitivity with the indirect spindown limit. The search sensitivity is defined by the number N_{seg} and length T_{seg} of the used data segments and the number of detectors N_{det} from which data is analyzed. The spindown range – and thus the covered star population – is defined through $\langle n_{\text{min}} - 1 \rangle \tau = 200\,\text{yr}$. The estimated runtime on 1000 nodes of the ATLAS compute cluster is 16.3 days.
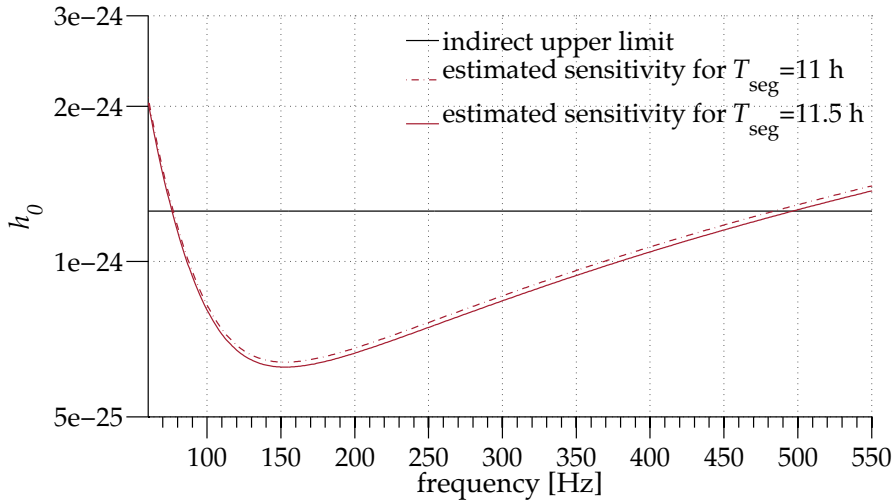
Figure 5.4.1: The expected sensitivities of the search for the two setups using 11 and 11.5 hours long data segments, respectively, are compared to the indirect spindown limit. The frequency range that the search covers is defined by the band in which the expected search sensitivity is lower than the indirect spindown limit. This range spans $78\ \text{Hz} \leq f \leq 496\ \text{Hz}$.

setup is given in Table 5.4.1.

The search does not cover a second order spindown. A thorough discussion of the consequences is given in Chapter 8. An estimate of the Doppler effects near the black hole on the spindown is given in Appendix A.8.

5.5 THE DATA

The data used for the search come from two of the three initial LIGO detectors, H1 and L1. The data was collected during the fifth Science Run (S5)[1] which started on November 4, 2005, at 16:00 UTC at Hanford and on November 14, 2005, at 16:00 UTC at Livingston. S5 ended on October 1, 2007, at 00:00 UTC. Various reasons exist for interruptions during the data collection period. The detectors can suffer unexpected loss of lock due to seismic disturbances, such as major earthquakes or large storms, or due to human activities. In addition to those lock losses, scheduled maintenance periods and commissioning work take place.

---

[1]See also Chapter 3. For more information about the detectors and the different Science Runs the interested reader is referred to [31].

The detector output is calibrated to produce a time series of gravitational wave strain $h(t)$ [29, 31]. Certain segments of the science data are excluded due to data quality concerns. The time series is then divided into $1800\,\mathrm{s}$ long segments, which are high-pass filtered above 40 Hz, Tukey windowed, and Fourier transformed to create Short Fourier Transform (SFT)s of $h(t)$. These SFTs are the input data to the presented data analysis pipeline.

During S5, the two detectors operated near their design sensitivities (see Figure 3.2.4). The average strain noise of H1 and L1 was $\lesssim 2.5 \times 10^{-23}\,\mathrm{Hz}^{-1/2}$ near 150 Hz. The strain sensitivity of the detectors and the duty factor improved over the S5 run.

5.5.1   Data Selection

As described in Section 5.4, the data is grouped into 630 segments, each spanning a period of $11.5\,\mathrm{h}$ and containing data from both detectors. In previous searches data segments have been chosen based on maximizing the number of SFTs per segment [29, 30]. This is a reasonable choice when observing the full sky: signals can originate from anywhere on the sky, and, hence, there is no further optimization possible. For this search, however, a different approach can be taken where the data segments can be chosen based on the expected $\langle 2\mathcal{F} \rangle$ values for a signal coming from the direction of the Galactic Center. In this section, both approaches are compared and the advantage of the latter segment selection criterion is demonstrated.

Consider a data set $\mathcal{C}$ which contains $\sim 35\,000$ segments that are created by grouping neighboring SFTs of the total available S5 data set into segments spanning $11.5\,\mathrm{h}$. Each segment overlaps the neighboring segments by $11\,\mathrm{h}$. For each segment in $\mathcal{C}$ the expected $\langle 2\mathcal{F} \rangle$ value is computed[2] on that data for a signal from the direction of the Galactic Center. Two different data sets are now created: set $\mathcal{A}$ is created by sorting the segments of set $\mathcal{C}$ in descending order by $\langle 2\mathcal{F} \rangle$. The segment with the highest $\langle 2\mathcal{F} \rangle$ value is chosen and overlapping segments are re-

---

[2]This is done by a program called `lalapps_PredictFStatistic`, which is available as part of the LSC Algorithm Library Suite (LALSuite). It analytically estimates the $\langle 2\mathcal{F} \rangle$ value for a given signal which, in our case, comes from the direction of the Galactic Center. The other parameters of the signal are chosen randomly within the possible range of variability of the target population. Also see Appendix A.2.

moved from the list. From the remaining segments the one with the highest $\langle 2\mathcal{F} \rangle$ is chosen and, again, all overlapping segments removed. This is repeated until 630 segments have been chosen. Set $\mathcal{B}$ is built in the same way as set $\mathcal{A}$, apart from the segment selection criterion which for set $\mathcal{B}$ is the number of SFTs contributing to each segment.

Because the data segments were selected according to the expected $\langle 2\mathcal{F} \rangle$ values, set $\mathcal{A}$ contains a list of segments that were recorded when the detector had a favorable orientation with respect to the sky location of Sgr A*. The dependence on favorable detector orientation can be quantified by the antenna pattern functions (see Equation 4.5) which take the highest value at times when the coupling between the detector and the sky position is especially good. Therefore, it is desirable to have as many data segments and, hence, SFTs as possible with large values of $\mathcal{S} \equiv F_+^2 + F_\times^2$. We quantify the advantage of set $\mathcal{A}$ by computing $\mathcal{S}$ at the midpoint of each SFT and normalizing over the number of SFTs. Consequently, the highest value that can be reached is 1. We obtain:

$$\mathcal{A} : \sum_{j=1}^{N_{\mathrm{SFT}}} \frac{(F_+^2 + F_\times^2)_j}{N_{\mathrm{SFT}}} = 0.58 \tag{5.13}$$

$$\mathcal{B} : \sum_{j=1}^{N_{\mathrm{SFT}}} \frac{(F_+^2 + F_\times^2)_j}{N_{\mathrm{SFT}}} = 0.39 \tag{5.14}$$

Thus, set $\mathcal{A}$ provides a more sensitive data set for a search in the direction of the Galactic Center than set $\mathcal{B}$ and will be used for this search[3].

Figure 5.5.1 shows $\mathcal{S}$ for each single SFT used in the search. In the zoom (right plot) the daily modulations of the antenna pattern functions are visible. The data points on top of the continuous function $\mathcal{S}(t)$ mark the selected SFTs. They are – when possible – centered around the peak of the daily pattern. Therefore, more SFTs with high values of $\mathcal{S}$ are chosen than with low values of $\mathcal{S}$.

---

[3]The exact start times of the used data segments are given in the Appendix in Tables A.3.1 to A.3.3
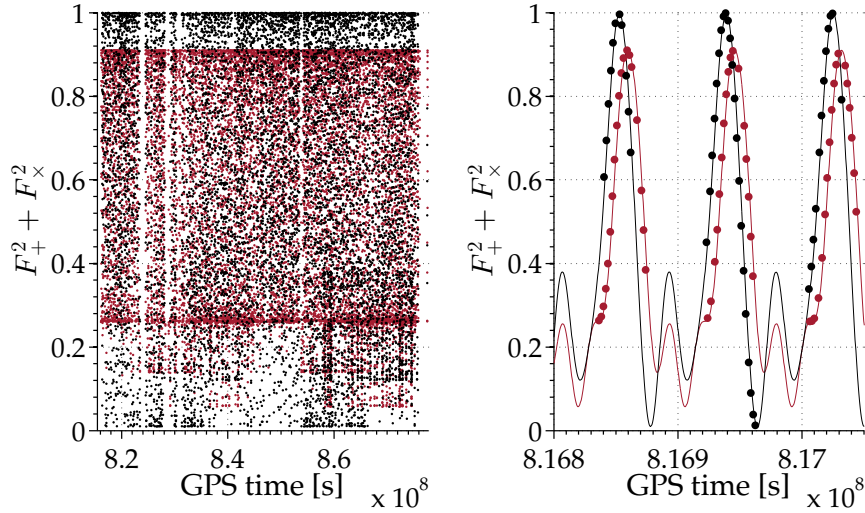
Figure 5.5.1: The antenna pattern functions $\mathcal{S} = F_+^2 + F_\times^2$ for the used data set. Red color shows the values for H1, black color stands for L1. The left plot shows the values of $\mathcal{S}$ for each single SFT used. The right plot shows the same, but zoomed in to a short time duration of 2.9 days within the first weeks of S5. The solid lines show $\mathcal{S}$ as a continuous function over time, while the data points denote the SFTs that were chosen (at the mid time of each SFT). The data selection procedure constructs segments composed of at most 23 contiguous SFTs spanning never more than 11.5 hours. If in a given 11.5 hour period there is not enough science data, that segment will comprise less than 23 SFTs. As described above, the segments are selected to maximize the expected $\langle 2\mathcal{F} \rangle$ value for a source at the Galactic Center. The expected $\langle 2\mathcal{F} \rangle$ values is proportional to $\mathcal{S}$, so every segment will be centered around the highest $\mathcal{S}$ SFTs. This is clearly visible in the right panel figure. Due to the shape of $\mathcal{S}$ as a function of time (faint continuous lines in the right panel) this results in an accumulation of SFTs with values of $\mathcal{S} \simeq 0.28$ for H1, as is clearly visible in the left plot. The reason that $\mathcal{S} < 1$ at all times for H1 is the latitude of Hanford ($46°17'8''$): the Galactic Center (which has a declination of $-29°0'28''$) can never reach the zenith.
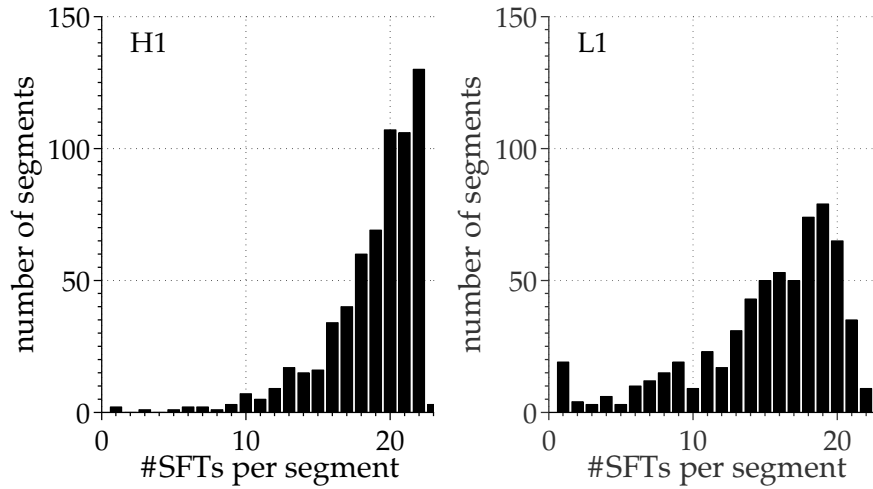
Figure 5.5.2: The distribution of the number of SFTs in the chosen data segments for H1 and L1, respectively. On average, the H1 segments are 82% filled (left plot) and the L1 segments 66% filled (right plot). The number of SFTs per segment from one detector can not exceed 11.5 h/1800 s = 23.

5.5.2 PROPERTIES OF THE SELECTED DATA SEGMENTS

Figure 5.5.2 shows the distributions of the number of SFTs per segment for H1 and L1, respectively, and for the chosen data set. On average, the H1 segments are 82% filled and the L1 segments 66% filled.

The distribution of SFT start times used in the segments with respect to local time is shown in Figure 5.5.3. Most of the data comes from night time periods. This is not surprising: the detectors' sensitivity and duty factor is higher at night, because human seismic noise is greatly reduced. In the histogram for L1 the sudden drop at ~ 2 o'clock in the morning is caused by a regularly-scheduled train that passes near to the observatory.

The sensitivity of H1 and L1 generally improved over the course of the Science Run due to commissioning work on the detectors. Figure 5.5.4 shows the number of SFTs used in the chosen segments for each week of the S5 run. Although the distribution of the SFTs is fairly uniform there is a slight trend to favor data near the end of the Science Run.
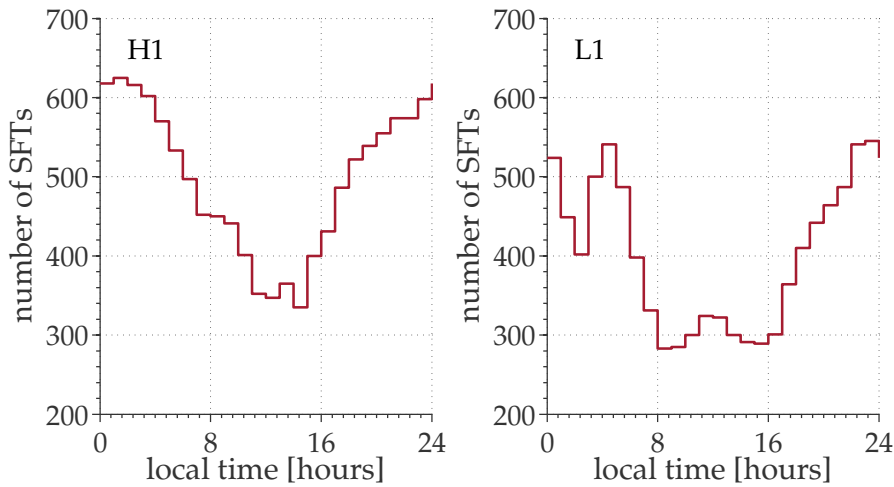
Figure 5.5.3: Distribution of the used SFTs over local time for H1 (left) and L1 (right), respectively. Most of the data have been taken during the night. This is mostly because human seismic noise is greatly reduced during the nights, but also because regular maintenance work of the detectors takes place during usual working ours. Thus, more data from night time periods are available and that data have higher quality. In the histogram for L1 a sudden drop at ~ 2 o'clock in the morning is due to a train regularly passing near to the site.
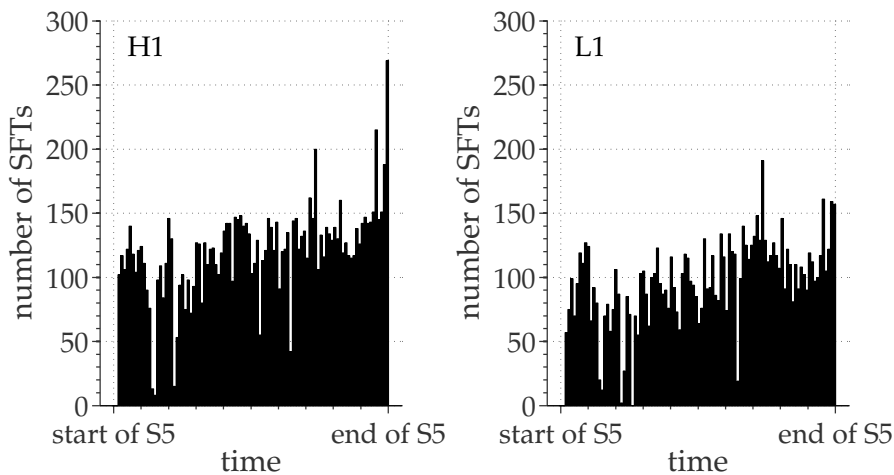
Figure 5.5.4: Distribution of the used SFTs over the whole S5 run in weeks for H1 (left) and L1 (right), respectively. Although the distribution of the SFTs is fairly uniform there is a slight trend to favor data near the end of the Science Run. This is because the general sensitivity of the detectors improved over the course of S5 as regular maintenance and commissioning work optimized the detector sensitivities over time.
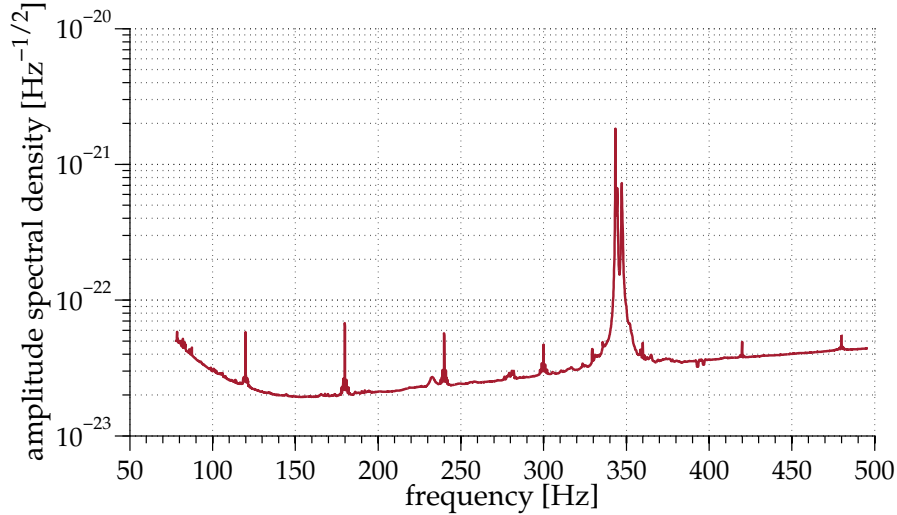
Figure 5.5.5: Amplitude spectral density of the used data set in 0.1 Hz bins, harmonically averaged over the two interferometers and harmonically summed over SFTs. The strength of a gravitational wave signal is proportional to the strain induced in the interferometer.

Finally, Figure 5.5.5 shows the amplitude spectral density (the square root of the power spectral density) of the chosen data set. The strength of a gravitational wave signal is proportional to the strain induced in the interferometer. The spectrum shows strong peaks every 60 Hz which are an artifact from the power lines and a broad peak around ~ 350 Hz which is due to violin modes.

For the search the SFTs have to be prepared in such a way that memory restrictions of the compute cluster are considered and the performance of the analysis program is optimized. Further, technical details on this preparation can be found in Appendix A.4.

5.6   THE MISMATCH OF THE TEMPLATE GRID

The given ranges in frequency and spindown are covered by a discrete template bank. As discussed in Section 4.4, the coherent analysis of the single segments uses a coarse grid, while the incoherent combination is done on a refined grid. The refinement takes place only in the frequency derivative, while the frequency

spacings remain unchanged. The spacings are:

$$\delta f = \frac{1}{T_{\text{seg}}} = 2.415 \times 10^{-5}\,\text{Hz}, \qquad\qquad (5.15)$$

$$\delta \dot{f}_{\text{coarse}} = \frac{1}{T_{\text{seg}}^2} = 5.834 \times 10^{-10}\,\text{Hz/s,}\ \ \text{and} \qquad (5.16)$$

$$\delta \dot{f}_{\text{fine}} = \frac{1}{\gamma T_{\text{seg}}^2} = 1.809 \times 10^{-13}\,\text{Hz/s.} \qquad\qquad (5.17)$$

The refinement factor is $\gamma = 3225$.

A gravitational wave signal will in general have parameters that lie between these points of the template grid. The *mismatch* m is the fractional loss in detection statistic due to the offset between the actual signal and the template parameters:

$$m = \frac{\langle 2\mathcal{F} \rangle^{\text{perfect match}} - \langle 2\mathcal{F} \rangle^{\text{best match}}}{\langle 2\mathcal{F} \rangle^{\text{perfect match}}}, \qquad\qquad (5.18)$$

where $\langle 2\mathcal{F} \rangle^{\text{perfect match}}$ is the value obtained for a template that has exactly the signal's parameters and $\langle 2\mathcal{F} \rangle^{\text{best match}}$ is the highest $\langle 2\mathcal{F} \rangle$ value obtained with the search template grid.

The distribution of the mismatch of the search with respect to the frequency and spindown parameters, $m_{f,\dot{f}}$, can be estimated through a Monte-Carlo study. For this, 5000 different realizations of fake data, each containing a continuous gravitational wave signal from the direction of the Galactic Center (and no noise) are created. The data sets comprise a frequency band of width $2\,\text{Hz}$ at $150\,\text{Hz}$. The signal parameters (frequency, spindown, intrinsic phase, polarization and inclination angle) are uniformly randomly distributed within the searched parameter space, the right ascension and declination are set to the coordinates of Sgr A*. The SFT timestamps of the fake data set coincide with the timestamps of the search data set. The fake data sets are then analyzed with the search template grid and the largest value $\langle 2\mathcal{F} \rangle^{\text{best match}}$ is identified. A second analysis is performed targeting the exact injection parameters to obtain $\langle 2\mathcal{F} \rangle^{\text{perfect match}}$. Figure 5.6.1 shows the normalized distribution of the 5000 mismatch values that are obtained with the described procedure. The average fractional loss is $\langle m_{f,\dot{f}} \rangle = 0.15$ and the maximum mismatch is $m_{f,\dot{f}}^{\text{max}} = 0.40$. This confirms that the used template grid
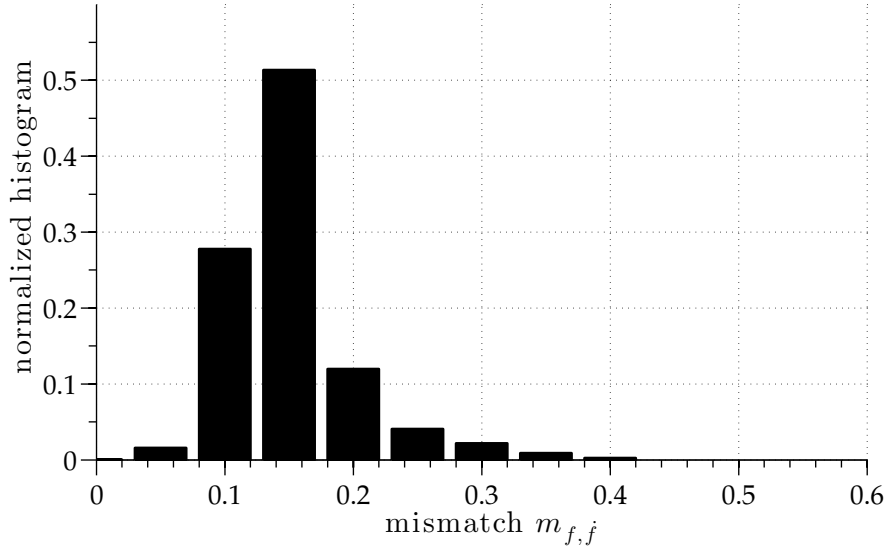
Figure 5.6.1: To obtain the average mismatch of the used search setup in frequency and spindown 5000 different realizations of data containing a continuous gravitational wave signal from the direction of the Galactic Center (and no noise) are created. The data sets are analyzed using the template grid of the search and the largest value $\langle 2\mathcal{F} \rangle^{\text{best match}}$ is identified. A second analysis targets the exact injection parameters and results in $\langle 2\mathcal{F} \rangle^{\text{perfect match}}$. The average mismatch obtained this way is $\langle m_{f,\dot{f}} \rangle = 0.15$.

spacings in frequency and spindown are reasonable: on average, due to the discrete nature of our template bank we expect to suffer a 15% loss in $\langle 2\mathcal{F} \rangle$ values. Only in a small fraction of cases (1%) the loss could be as high as 40%.

5.6.1 THE SKY LOCATION

Although $\mathcal{O}(100)$ neutron stars are expected to be located within the inner $1\,\text{pc}$ of the Galactic Center (see Section 2.3.1), no pulsars have yet been detected in that area. As a consequence, there are no known point targets for this search. However, a gravitational wave signal coming from the immediate neighborhood of Sgr A* will still show up with sufficiently large $\langle 2\mathcal{F} \rangle$ values, even though a single sky position template at the position of Sgr A* (Table 5.6.1) is used.

The distribution of fractional loss in detection statistic due to an offset in the

Targeted sky coordinates: the sky position of Sgr A*		
Right ascension	$17^{\mathrm{h}}\,45^{\mathrm{m}}\,40^{\mathrm{s}}.0409$	4.64985 rad
Declination	$-29°\,00''\,28'.118$	-0.50628 rad

Table 5.6.1: The coordinates of Sgr A*. These are the coordinates used for the only sky template in this search.

sky coordinates can be estimated by a Monte-Carlo study equal to the one just described. This time only the parameters of the sky position are mismatched with respect to the parameters used in the analysis. A set of 1000 realizations, each containing an injected continuous gravitational wave signal and no noise, is created. The sky coordinates of the injected signals vary within $R \leq 10^{-3}$ rad around the coordinates of Sgr A* (this translates into $R \lesssim 8$ pc). The remaining parameters are uniformly randomly distributed within the searched parameter space. As before, two analyses are performed: one targets the coordinates of the signal injection yielding $\langle 2\mathcal{F} \rangle^{\mathrm{perfect\ match}}$ and one targets the coordinates of Sgr A*, resulting in $\langle 2\mathcal{F} \rangle^{\mathrm{best\ match}}$. Both analyses used a single template in frequency and spindown equal to the parameters of the injection. Thus, the loss in detection statistic is only due to the mismatch in sky position m_s. The study results in an average loss of $\langle m_s \rangle = 5.5 \times 10^{-3}$ and a maximum loss of $m_s^{\mathrm{max}} = 0.06$.

The actual loss in detection statistic is the combination of the loss due to the parameter mismatch in frequency and spindown and the loss due to a mismatch in sky position. It is obtained in a third Monte-Carlo study, again on 1000 realizations of fake data. In this study the sky coordinates as well as the frequency and spindown parameters are mismatched with respect to the parameters of the search template grid. The total mismatch m of the search is obtained to be on average $\langle m \rangle = 0.15$ with a maximum of $m^{\mathrm{max}} = 0.40$. Figure 5.6.3 shows the resulting histogram. The obtained values do not differ much from the ones obtained in the first study. This is correct: the additional fractional loss due to a mismatch in sky position within $R \leq 10^{-3}$ rad is negligible.
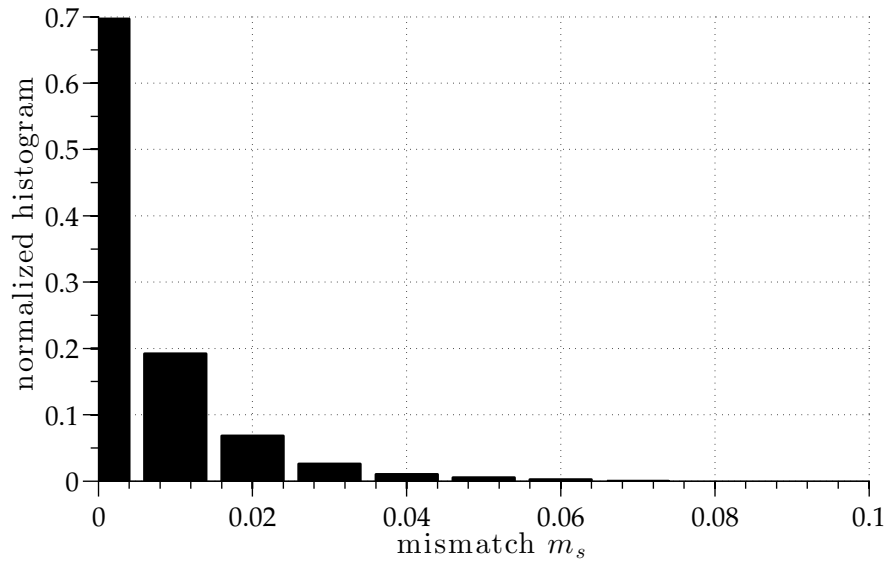
Figure 5.6.2: The histogram shows the fractional loss in detection statistic $\langle 2\mathcal{F} \rangle$ due to a mismatch in sky position between the coordinates of the source and the template. On average this loss is $\langle m_s \rangle = 5.5 \times 10^{-3}$.
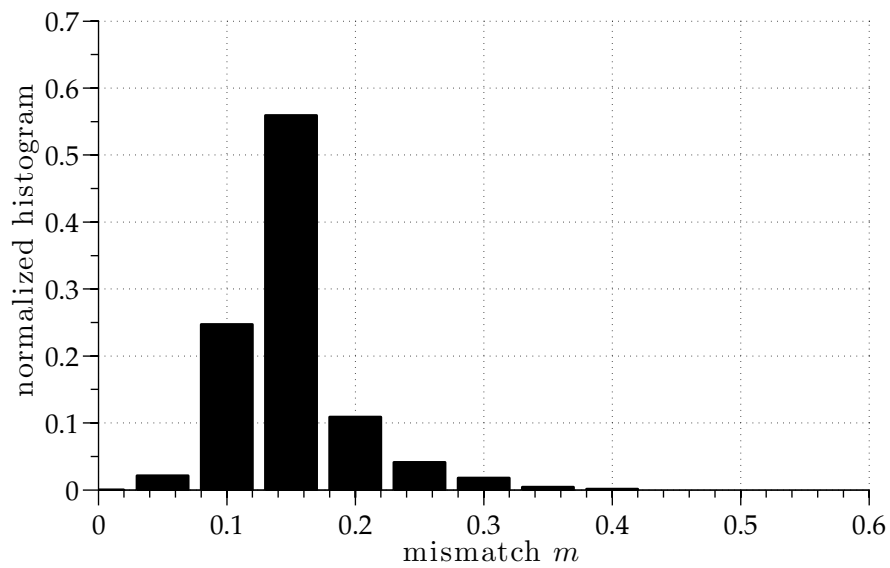
Figure 5.6.3: The histogram shows the fractional loss in detection statistic $\langle 2\mathcal{F} \rangle$ due to a mismatch in sky position, frequency, and spindown parameters between the injection parameters and the search template grid. On average this loss is $\langle m \rangle = 0.15$.

5.7   Partitioning the Parameter Space

The total number of templates of the search is defined by the covered ranges in frequency and spindown (Figure 5.3.1) and the corresponding spacings between the templates (Equation 5.15) which are placed in a simple, rectangular grid. To make the analysis computationally feasible this number of templates has to be distributed over smaller compute *jobs*. Each of these jobs is assigned a certain frequency band and a corresponding spindown band, as explained in Section 5.4, Equation 5.12[4]. Each job returns the values of the detection statistic at the most significant 10^5 points in parameter space. The total number of templates N can be computed by summing the number of templates in each job i[5]:

$$
\begin{aligned}
N &= \sum_{i=0}^{10677} \left(N_{f,i} \times N_{\dot{f},i} \times N_{\text{sky},i} \right) \\
&= \sum_{i=0}^{10677} \left(\frac{\Delta f_i}{\partial f} \times \frac{\Delta \dot{f}_i}{\partial \dot{f}} \right) \\
&= \sum_{i=0}^{10677} \left(\frac{f_{\text{max},i} - f_{\text{min},i}}{T_{\text{coh}}^{-1}} \times \frac{\dot{f}_{\text{max},i} - \dot{f}_{\text{min},i}}{\gamma T_{\text{coh}}^{-2}} \right) \\
&= \sum_{i=0}^{10677} \left((f_{\text{max},i} - f_{\text{min},i}) \, \gamma T_{\text{coh}}^3 \frac{f_{\text{max},i}}{\tau} \right) \\
&= 4\,355\,231\,668\,681 \sim 4.4 \times 10^{12}.
\end{aligned}
\tag{5.19}
$$

Figure 5.7.1 shows the number of templates per job versus the minimum frequency of the job. The number of templates per job is not constant but decreases with increasing frequency due to the internal structure of implementation of the used analysis program (see Appendix A.1 for details on the code structure). Figure 5.7.2 illustrates the relation between the frequency span and spindown range

---

[4]A reasonable setup that yields computation times for each job of $\sim$ 5 h on an Intel® Xeon® CPU X3220@2.40GHz results in 10678 jobs. The jobs are processed by the ATLAS compute cluster at the Max-Planck-Institut für Gravitationsphysik (Albert-Einstein-Institut) in Hanover, Germany.

[5]Since only one coordinate in sky is targeted, the number of sky templates N_{sky} is one.

of each job[6].

5.8 STATISTICAL VALIDATION OF THE ANALYSIS RESULTS

The search computes a $\langle 2\mathcal{F} \rangle$ value for each template and reports back a top list containing the most significant 10^5 candidates. To quantify the meaning of "significant" the expectation value and the variance for this search setup under the assumption of Gaussian noise are derived and compared to the analysis results.

5.8.1 THE EXPECTATION VALUE AND THE VARIANCE

As discussed in Section 4.4, the $2\mathcal{F}$-statistic in Gaussian noise is the sum of four squared Gaussian variables and therefore described by a χ^2 distribution with $n = 4$ degrees of freedom. The expectation value $\mathrm{E}[\ldots]$ and the variance $\mathrm{Var}[\ldots]$ of such a statistic are:

$$\mathrm{E}\left[\chi^2\right] = n \quad \text{and} \quad \mathrm{Var}\left[\chi^2\right] = 2n. \tag{5.20}$$

In the used analysis technique the resulting detection statistic value is the sum of the single $2\mathcal{F}_j$ values for each data segment j divided by the $N_{\mathrm{seg}} = 630$ data segments (compare Equation 4.51):

$$\langle 2\mathcal{F} \rangle = \frac{\sum_{j=1}^{N_{\mathrm{seg}}} 2\mathcal{F}_j}{N_{\mathrm{seg}}}. \tag{5.21}$$

Since the sum of m independent χ^2 variables each having n degrees of freedom is again a χ^2 variable with $m \times n$ degrees of freedom, $\sum_{j=1}^{N_{\mathrm{seg}}} 2\mathcal{F}_j$, follows again a χ^2 distribution with 4×630 degrees of freedom. The expectation value and variance

---

[6]The largest frequency band that is covered by a job is that of job 0, starting at the lowest frequency of the search. The size of that band is ~ 0.61 Hz. The spindown band covered by this job is the smallest of all spindown bands with $\sim 1.25 \times 10^{-8}$ Hz/s. The last job (ID 10677, ending at the last frequency of the search) has the smallest frequency band, ~ 0.015 Hz, and the largest spindown band of $\sim 7.86 \times 10^{-8}$ Hz/s.
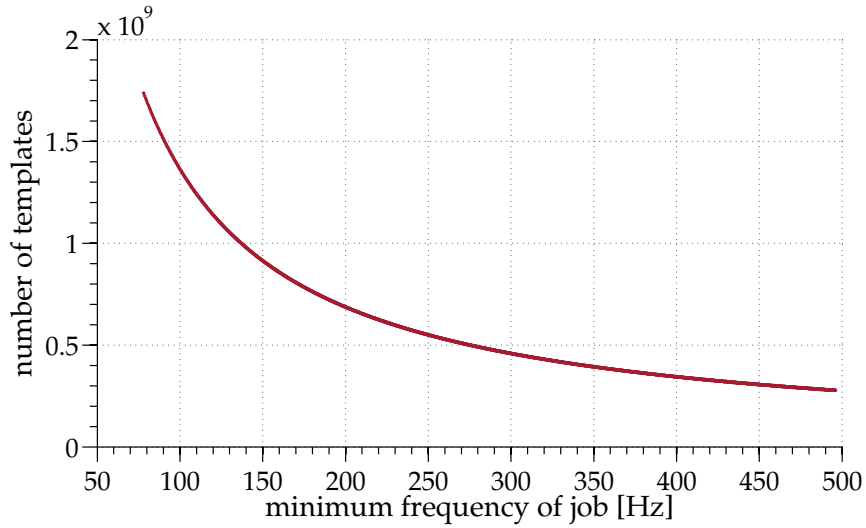
Figure 5.7.1: The number of templates in each job versus the minimum frequency in each job.
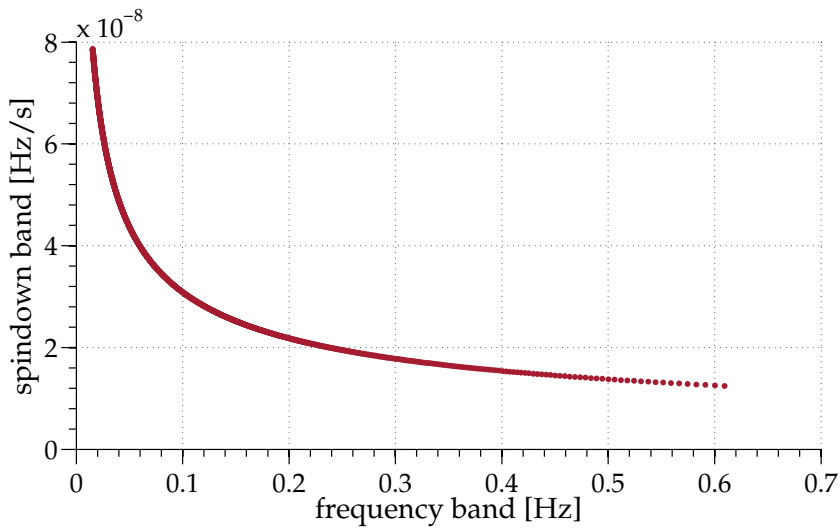
Figure 5.7.2: This plot gives a slightly different view on the jobs, showing the frequency bands covered by each job together with the spindown bands.

of such a variable are:

$$\mathrm{E}\left[\chi_1^2 + \chi_2^2 + \ldots + \chi_{N_{\mathrm{seg}}}^2\right] = N_{\mathrm{seg}}\,\mathrm{E}\left[\chi^2\right] = N_{\mathrm{seg}}n, \qquad (5.22)$$

$$\mathrm{Var}\left[\chi_1^2 + \chi_2^2 + \ldots + \chi_{N_{\mathrm{seg}}}^2\right] = N_{\mathrm{seg}}\,\mathrm{Var}\left[\chi^2\right] = 2N_{\mathrm{seg}}n. \qquad (5.23)$$

Dividing by the number of segments N_{seg} gives:

$$\mathrm{E}\left[\frac{\chi_1^2 + \chi_2^2 + \ldots + \chi_{N_{\mathrm{seg}}}^2}{N_{\mathrm{seg}}}\right] = \frac{N_{\mathrm{seg}}\,\mathrm{E}\left[\chi^2\right]}{N_{\mathrm{seg}}} = n = 4, \qquad (5.24)$$

$$\mathrm{Var}\left[\frac{\chi_1^2 + \chi_2^2 + \ldots + \chi_{N_{\mathrm{seg}}}^2}{N_{\mathrm{seg}}}\right] = \frac{N_{\mathrm{seg}}\,\mathrm{Var}\left[\chi^2\right]}{N_{\mathrm{seg}}^2} = \frac{2n}{N_{\mathrm{seg}}} = 0.0127. \qquad (5.25)$$

More generally, $\langle 2\mathcal{F}\rangle$ is a specific case of the a Γ-distribution with a mean of 4 and a variance of $8/630$.

5.8.2 THE LARGEST $\langle 2\mathcal{F}\rangle$ VALUE

In this section the largest expected detection statistic value for Gaussian noise is computed. The probability density $p^{\mathrm{loudest}}(2\mathcal{F}^*)$ for the largest summed $2\mathcal{F}$ value, $2\mathcal{F}^*$, is [7]:

$$p^{\mathrm{loudest}}(2\mathcal{F}^*) = N\,p(\chi_{4\times630}^2; 2\mathcal{F}^*)\left[\int_0^{2\mathcal{F}^*} p(\chi_{4\times630}^2; 2\mathcal{F})\mathrm{d}(2\mathcal{F})\right]^{(N-1)}. \qquad (5.26)$$

The expected value of the largest detection statistic value over N independent trials simply is:

$$\mathrm{E}\left[2\mathcal{F}^*\right] = \int_{-\infty}^{\infty} 2\mathcal{F}^*\,p^{\mathrm{loudest}}(2\mathcal{F}^*)\mathrm{d}(2\mathcal{F}^*), \qquad (5.27)$$

which translates for the expectation value of the largest value of the used statistic,

$\langle 2\mathcal{F}^* \rangle$, to:

$$E\left[\langle 2\mathcal{F}^* \rangle\right] = \frac{1}{N_{\text{seg}}} E\left[2\mathcal{F}^*\right], \tag{5.28}$$

and the standard deviation is:

$$\sigma = \sqrt{E\left[\langle 2\mathcal{F}^* \rangle^2\right] - \left(E\left[\langle 2\mathcal{F}^* \rangle\right]\right)^2}. \tag{5.29}$$

Taking N equal to the total number of templates of this search (Equation 5.19) the largest expected detection statistic value $\langle 2\mathcal{F}^* \rangle$ in absence of a signal in the data is:

$$E\left[\langle 2\mathcal{F}^* \rangle\right] = 4.881, \tag{5.30}$$

and the variance is:

$$\sigma^2\left[\langle 2\mathcal{F}^* \rangle\right] = 0.036. \tag{5.31}$$

These calculations assume that the N templates are independent. However, this assumption does not hold for the template grid used in this search. To estimate the number of *effective* templates, a Monte-Carly study is performed in which 1000 different realizations of pure Gaussian noise are analyzed with a small template grid (containing 40000 templates) that has the resolution of the search template grid. After each test search the loudest candidate $\langle 2\mathcal{F}^* \rangle$ is identified. Figure 5.8.1 shows the distribution of these values[7]. The gray solid line denotes the expectation value for $N = 40000$ templates, which is at 4.489 ± 0.035. The black solid line shows the probability density $p\left(\langle 2\mathcal{F}^* \rangle\right)$ for $N_{\text{eff}} = 0.48N$. The lower number of effective independent templates moves the distribution of $p\left(\langle 2\mathcal{F}^* \rangle\right)$ towards lower values of $\langle 2\mathcal{F} \rangle$, increasing the actual significance of candidates. The expectation value for the loudest candidate with N_{eff} is 4.468 ± 0.036. Assuming the templates of our search as independent leads to an overestimate of the expected loudest candidate. The largest value we would expect would accordingly be reduced by $\sim 0.5\%$. This is less than one standard deviation for this test search. However, this test search comprised only a tiny fraction of the templates used in the real search

---

[7]In order to conduct this comparison the resulting $\langle 2\mathcal{F} \rangle$ values have to be shifted by 0.02 towards lower values. This systematic bias is well understood and documented [99] and is due to an implementation detail of the $2\mathcal{F}$-statistic in the used analysis program. Also see Appendix A.5.
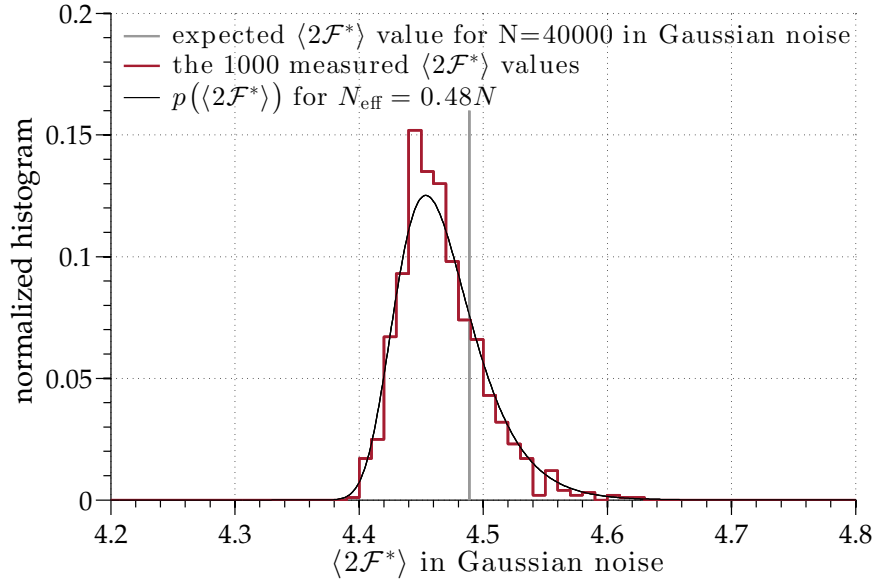
Figure 5.8.1: Estimation of the effective number of templates by fitting the probability density $p(\langle 2\mathcal{F}^*\rangle)$ (black line) to the distribution of the loudest candidate measured in 1000 searches over Gaussian fake data (red histogram). The gray line denotes the expectation value for $N = 40000$. The effective number of templates can this way be estimated to be $N_{\text{eff}} = 0.48N$.

and can not necessarily be extrapolated.

5.8.3 VALIDATION OF THE ANALYSIS RESULTS

To verify the outcome of the search a data set equivalent to the original data set is created which contains pure Gaussian noise. Then a search over $N = 290\,250$ templates located around 100 Hz is performed with the template resolution of the search, and the $\langle 2\mathcal{F}\rangle$-distribution is determined. The resulting distribution is compared with the expected Γ-distribution. The two distributions are shown in Figure 5.8.2. A Kolmogorow-Smirnov-Test, performed to verify the consistency of the two distributions, results in a value of 1.

Similar behavior is observed on real data in frequency bands that are not affected by disturbances. Figure 5.8.3 shows the results of a search equal to the one just
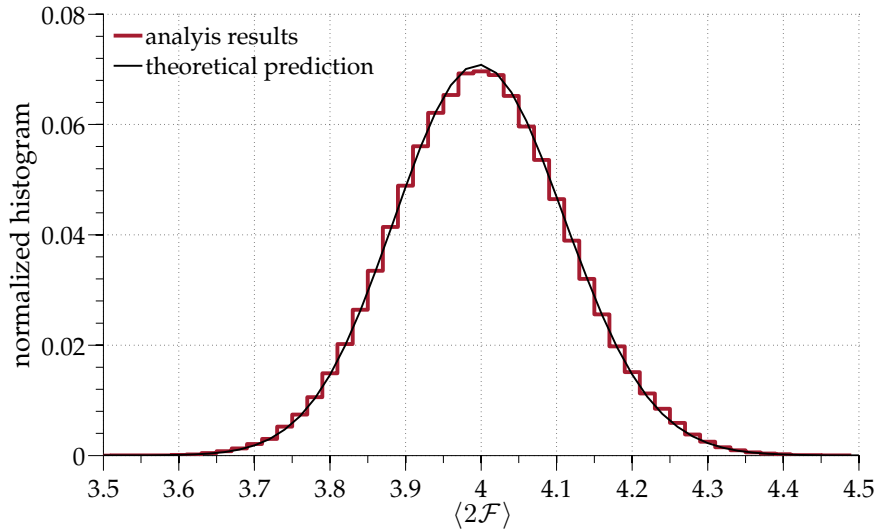
Figure 5.8.2: Verification of the search results: a set of fake data containing
pure Gaussian noise is created. The start times of the used SFTs equal those
of the search data set. The red histogram shows the resulting $\langle 2\mathcal{F} \rangle$ values.
The black line shows the theoretical prediction. The analysis results match the
theoretical expectation very well: a Kolmogorow-Smirnov-Test performed on the
two distributions results in a value of 1.

described on Gaussian data, but actually performed on the real data set. The results
indicate a very good agreement with the expectation. A Kolmogorow-Smirnow-
Test is performed again, yielding the same result of 1. The data can therefore largely
be assumed as Gaussian. However, certain frequency bands contain non-Gaussian
noise artifacts, but these noise outliers are removed during further processing of
the data (see Section 6.1). The number of frequency bands disturbed by strong
noise artifacts are about $\sim 7\%$ of the total.

As a point of comparison, the same analysis is repeated a third time on a set of
fake Gaussian data, but this time it includes an injected gravitational wave signal
with amplitude $h_0 = 3.5 \times 10^{-25}$. This signal is rather weak and represents a
population of signals that this search can detect only in a few frequency bands, as
will be shown in Section 7.3. The data is analyzed in the same way as before and the
results for the complete list of templates is stored. The outcome is a distribution of
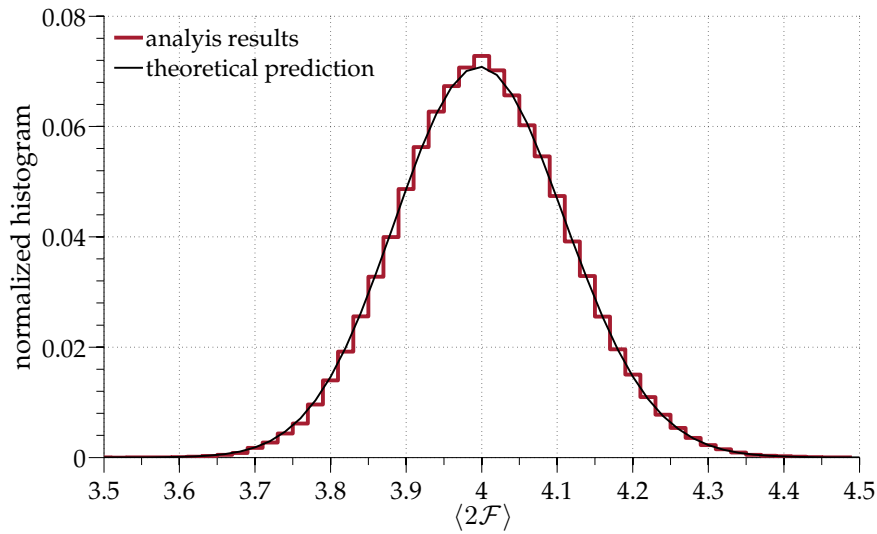
Figure 5.8.3: In this plot the theoretical expectation (black line) is compared with the result of an analysis on real data (red histogram). As before, the analysis results and the theoretical expectation match well. Also here, a Kolmogorow-Smirnow-Test results in a value of 1.

$\langle 2\mathcal{F} \rangle$ values that shows the typical characteristics of a weak signal (Figure 5.8.4): in addition to the typical distribution that results from the analysis of the Gaussian noise background, a few templates show increased $\langle 2\mathcal{F} \rangle$ values. Due to the signal that was injected into the data with $N = 290\,250$ templates the expectation value of the largest $\langle 2\mathcal{F} \rangle$ in pure noise can be calculated to be 4.54 ± 0.03. The largest $\langle 2\mathcal{F} \rangle$ value derived by this test search is 4.63. This signal is therefore detected with a $\langle 2\mathcal{F} \rangle$ value ~ 2.7 standard deviations above the noise. If the noise level of the real data is as clean as in the fake data set such a signal would be detected by the search.
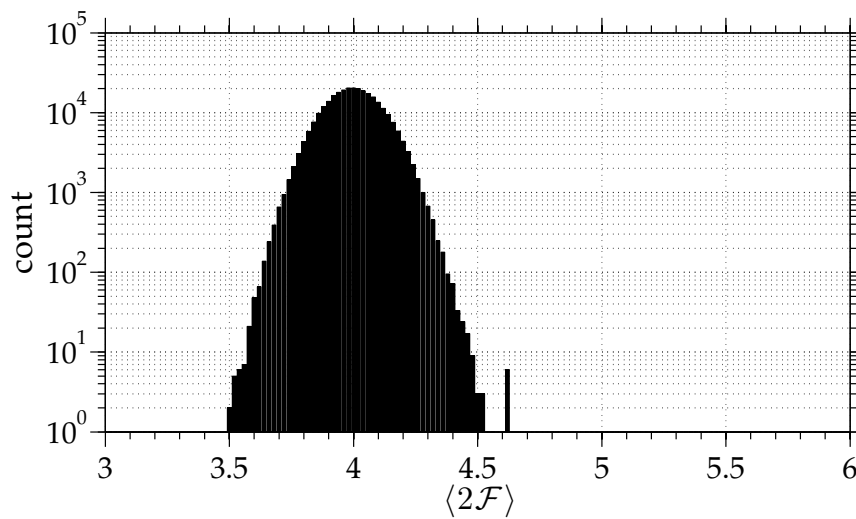
Figure 5.8.4: Histogram of the resulting $\langle 2\mathcal{F} \rangle$ values for a data set containing Gaussian noise and an additional gravitational wave signal injection. The signal is injected with strength $h_0 = 3.5 \times 10^{-25}$ (at the detection limit) at ~ 150 Hz. The distribution shows a typical peak at ~ 4 and a few increased $\langle 2\mathcal{F} \rangle$ values which are due to the signal injection. The largest $\langle 2\mathcal{F} \rangle$ value is ~ 2.7 standard deviations above the largest expected $\langle 2\mathcal{F} \rangle$ value for Gaussian noise.

Conducting data analysis is like drinking a fine wine. It is important to swirl and sniff the wine, to unpack the complex bouquet and to appreciate the experience. Gulping the wine doesn't work.

Daniel B. Wright

6

Post-Processing

Each of the 10678 jobs reports back the top 10^5 candidates of the processed templates. This gives a list of $\sim 10^9$ candidates in total. Out of these all candidates with a $\langle 2\mathcal{F} \rangle$ value higher than the largest expected value $\langle 2\mathcal{F}^* \rangle$ for Gaussian noise minus three standard deviations are investigated. This selection, however is done not at the beginning of the post-processing but at a later step and the reason for this will be explained (Section 6.4). At first, all $\sim 10^9$ candidates are examined to identify those that can be ruled out as being gravitational wave signals. A variety of reasons exist to discard candidates: in the first step candidates stemming from known detector artifacts are removed (Section 6.1). The remaining list is then reduced by clustering candidates that can be ascribed to the same possible signal (Section 6.2). The next steps aim to uncover candidates whose high significance is due to terrestrial disturbances. Those candidates do not display the signature that is expected from a continuous gravitational wave signal, for example amplitude consistency in both detectors and permanence in the data (Sections 6.3 and 6.5). The surviving candidates are followed up by a more sensitive coherent search (Section 6.6).

The aim of the post-processing is to identify promising gravitational wave candidates. While trying to design the different steps to be as effective as possible in rejecting disturbances, one has to make sure that a real gravitational wave signal does indeed pass all applied tests and vetoes. To account for that, the vetoes used in this post-processing are tested on a set of Gaussian data that contains additional injected gravitational wave signals. This test set contains 500 different realizations of signals in Gaussian noise. The parameters of these signals are uniformly, randomly distributed over the search parameter space as shown in Table 6.0.1.

The strength of the signals depends on their frequency and is set to a value close to $h_0^{90\%}$, the upper limit value[1] of the gravitational wave amplitude for that frequency (see Section 7). All vetoes of the post-processing are applied to this set of test data to evaluate the false dismissal rates.

---

[1]Early false dismissal studies were performed with more arbitrarily chosen h_0 values, to allow the testing of the vetoes before the $h_0^{90\%}$ values were established. After the upper limits have been derived, the false dismissal studies were repeated, folding in this information to give more precise false dismissal rates by injecting signals at that strength.

PARAMETER	RANGE
Signal strength	$h_0^{90\%}(f)$
Sky position [rad]	$\sqrt{\alpha^2 + \delta^2} \leq 10^{-3}$ rad from Galactic Center
Frequency [Hz]	$78\,\text{Hz} \leq f \leq 496\,\text{Hz}$
Spindown [Hz/s]	$0 \leq \dot{f} \leq (-f_{\text{max}}/200\,\text{yr})$, for a given f_{max}
Polarization angle	$0 \leq \psi \leq 2\pi$
Initial phase constant	$0 \leq \phi_0 \leq 2\pi$
Inclination angle	$-1 \leq \cos\iota \leq 1$

Table 6.0.1: Parameters of the false dismissal study test set. 500 signals have been injected into Gaussian noise. The parameters of the signals are uniformly randomly distributed within the searched parameter space.

6.1 Cleaning the Data from Known Disturbances

As discussed in Section 3.2, gravitational wave interferometers have to be extremely sensitive instruments to enable the measurement of the effect a gravitational wave has on the test masses. A large effort goes into the improvement of the suspension system of the test masses used in the interferometers. The ideal, freely hanging test mass, insensitive to any kind of impact from the outside world, however, can not be realized. The influence of terrestrial disturbances, like anthropogenic activities at the sites, and seismic noise, like earthquakes or large storms, affects the data in undesired ways. Another kind of disturbances are detector artifacts, like the violin modes of the suspension cables, the chiller that cools the laser, different control system components, and the power lines themselves, pulsing regularly like clocks at $60\,\mathrm{Hz}$ and at all harmonics. These stationary spectral lines may show up in the analysis results as suspiciously large $\langle 2\mathcal{F} \rangle$ values. Over the last years, knowledge about these hidden noise sources has been collected, mostly by searching for correlations between the gravitational wave channel of the detector and other auxiliary channels, like, for example, the input power channel for the $60\,\mathrm{Hz}$ harmonics. Only rarely, those noise sources can be mitigated. The process of uncovering those sources is time consuming and difficult. Every time that the detector is worked on things can change and new lines can appear while others may disappear. Some lines can only be traced after observing the data for the full length of the Science Run and therefore a – more or less – complete list can only be compiled after the run has finished. This makes it difficult, if not impossible, to reject corrupted data before starting the analysis. On the other hand, it would not necessarily be desirable to ban that data right away. Depending on the analysis, faint disturbances might be acceptable and the data worth being kept, as the following sections will show.

6.1.1 The Conservative Known Lines Cleaning

Tables A.6.1 and A.6.2 contain the frequency bands that are known to contain detector artifacts. The cleaning procedure, as it has been used for example in past all-sky searches [3], removes all candidates whose value of the detection statistic has had contributions from data contaminated by such disturbances. To identify

those candidates one has to take into account that over the course of the observation time (almost two years) the frequency of a signal at the detector can change due to Doppler effects within $\pm f v_{\text{orb}}/c$, where f is the frequency of the signal and v_{orb} is the orbital velocity of the Earth. In addition to that, the spindown of the signal moves the frequency by $|\dot{f}|(t_{\text{ref}} - t_{\text{start}})$, where t_{ref} is the reference time and t_{start} is the start time of the first data segment. To decide whether data from frequency bins in a corrupted band have contributed to the detection statistic at a parameter space point $\{f, \dot{f}\}$, one has to consider both the Doppler broadening and the spindown effect and compare it with the frequency band of the known detector artifact. If these two bands overlap in any way, there may have been contamination of the detection statistic value by the disturbance.

This cleaning process removes a certain fraction of the candidates and can usually be applied without problems. But the high spindown values covered by this search present a new challenge: the width of vetoed bands increases with larger spindown values and – if present – with higher harmonics. The conjunction of the large spindown values and the regular occurrence of the 1 Hz harmonics cause a huge loss in the number of candidates.

Figure 6.1.1 shows the impact of this problem: the total parameter space covered by this search is illustrated in gray color. On top, in red color, the candidates that survive the conservative known lines cleaning procedure are plotted. Figure 6.1.2 shows the amount of vetoed parameter space over spindown: all candidates with spindown values $|\dot{f}| \gtrsim 1.6 \times 10^{-8}$ Hz/s are removed by the cleaning procedure, if applied as described.

The application of the conservative known lines cleaning de facto removes a large fraction of the search parameter space and on this set of candidates results in a loss of $\sim 88.6\%$ of all candidates (only 121 927 183 out of 1 067 800 000 are left). This is unacceptable because the large range in spindown is one of the main strengths of the search, since such a parameter space is computationally infeasible for present all-sky searches. Such loss is also unnecessary as will be shown in the next section, and a more forgiving variation on this veto scheme can be derived.
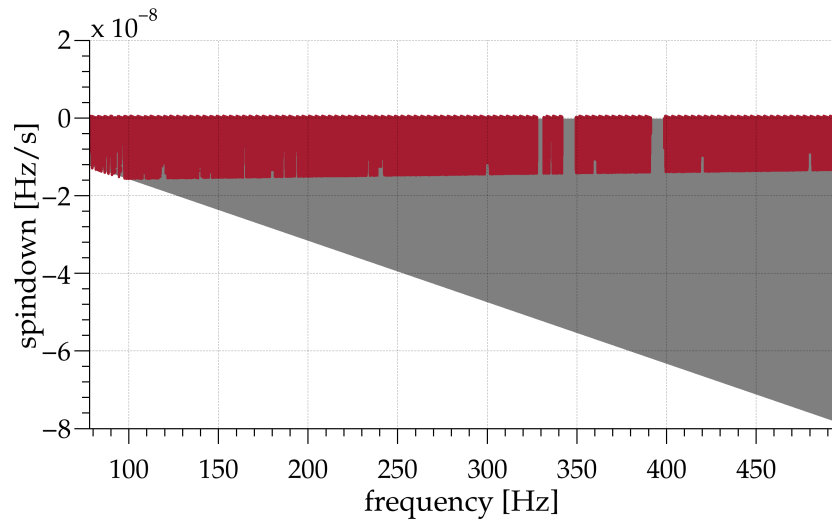
Figure 6.1.1: This plot illustrates the impact of the conservative known lines cleaning procedure on the parameter space that is covered by the search. The gray region shows the covered parameter space. On top, in red color, the candidates that survive the conservative known lines cleaning procedure are shown. All templates above $|\dot{f}| \gtrsim 1.6 \times 10^{-8}$ Hz/s are lost.
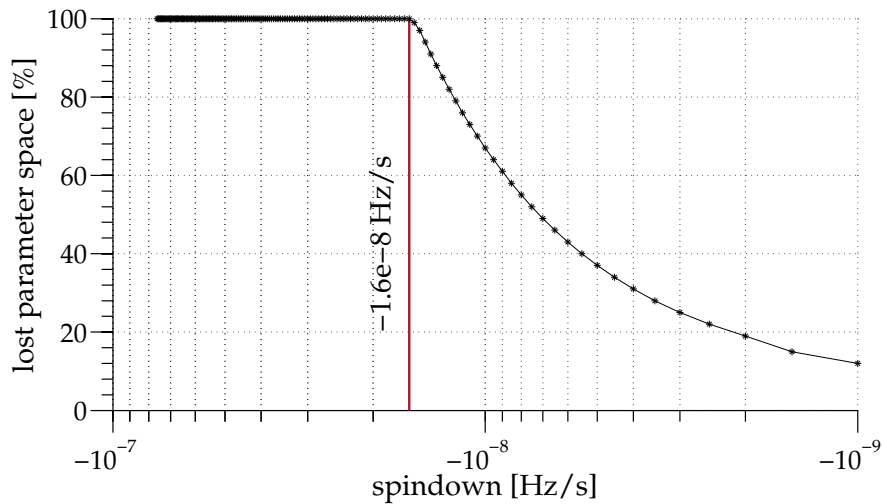
Figure 6.1.2: The vetoed band in percentage as a function of the spindown value. All candidates with spindown values $|\dot{f}| \gtrsim 1.6 \times 10^{-8}$ Hz/s will be removed by the conservative known lines cleaning procedure, if applied as described.

6.1.2   THE FLEXIBLE KNOWN LINES CLEANING

If a signal has a very large spindown value, its intrinsic frequency changes rapidly over time. Over the course of two years (which is about the time this search spans) in the worst case a signal's intrinsic frequency can change by at most ~ 5 Hz. The conservative cleaning procedure removes candidates regardless of the amount of potentially contaminated data used for their analysis. Consider an average spindown value covered by the search, $\dot{f}_{\mathrm{av}} = -5.9 \times 10^{-8}$ Hz/s. The 1 Hz harmonic has a width of $\Delta f = 1.6 \times 10^{-4}$ Hz at 1 Hz and 0.08 Hz in the worst case, at 496 Hz. The time needed to sweep through a band of that size with the given spindown is $\Delta t = \Delta f / \dot{f}_{\mathrm{av}} = 1\,355\,172$ s. Since one data segment spans 41400 s, at most about 33 of the 630 segments are affected by that artifact: $\sim 5\%$. That implies that only a very small percentage of the data used for the analysis of high spindown templates are potentially contaminated.

Additionally, the analysis technique is less sensitive to stationary lines. The wave forms used in the matched filtering step are Doppler-modulated sine curves with yearly modulations of the Earth's travel around the Sun and daily modulations for the spin of the Earth. Terrestrial disturbances are stationary spectral lines and, therefore, do *not* follow the described sine pattern. The analysis is much less sensitive to this kind of signals. To illustrate this statement a Gaussian data set (which matches the original data set in terms of SFT start times) is created and a stationary line is injected with $h_0 = 7.6 \times 10^{-25}$. The injection is present throughout the whole data set. This data set is then analyzed twice, once with the standard search technique and once using the same method, but with Doppler demodulation turned off. In the latter case, the search is sensitive to stationary lines and insensitive to gravitational wave signals. Figures 6.1.3 and 6.1.4 show the outcome of both searches. The expected maximum $\langle 2\mathcal{F} \rangle$ value for the case of Gaussian noise and the number of templates searched is ~ 4.7. The resulting $\langle 2\mathcal{F} \rangle$ values of the first analysis (including the Doppler demodulation step) are all below that value, as would be expected for the case of pure Gaussian noise. No signal (or disturbance) is detected. In contrast to that, the resulting $\langle 2\mathcal{F} \rangle$ values of Figure 6.1.4 are obtained by switching the Doppler demodulation off. The result is a sharp, well located peak, centered around the stationary spectral line that was injected at
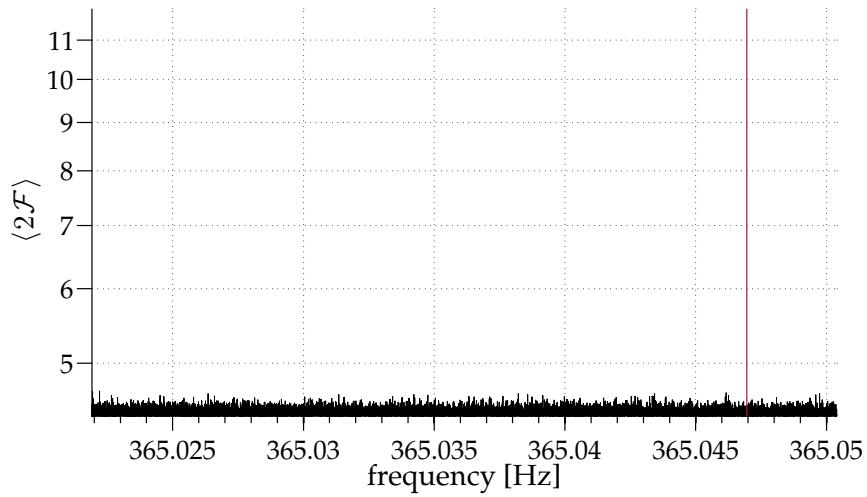
Figure 6.1.3: The $\langle 2\mathcal{F} \rangle$ values resulting from the standard search on data containing Gaussian noise and a stationary line. The red line shows the frequency of the injected spectral line, $f = 365.047$ Hz.
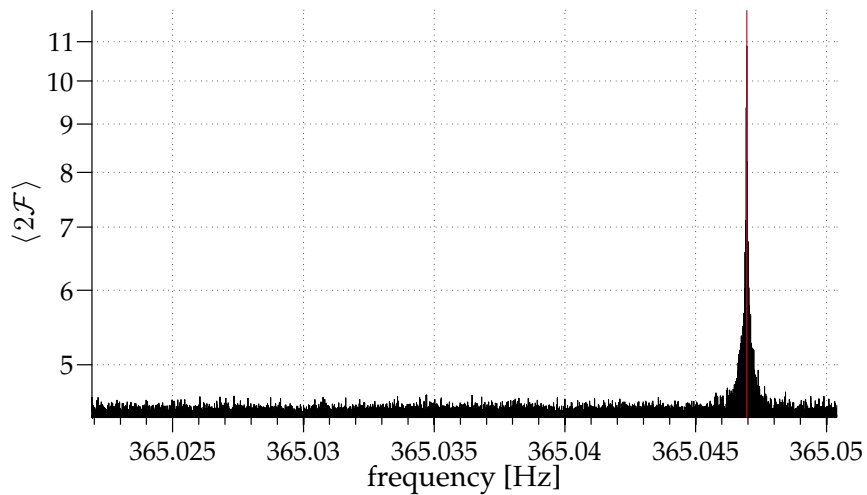
Figure 6.1.4: The $\langle 2\mathcal{F} \rangle$ values resulting from the search with the Doppler demodulation turned off of data containing Gaussian noise and stationary line. The red line shows the frequency of the injected spectral line, $f = 365.047$ Hz.

a frequency of 365.047 Hz.

A third factor that comes into play is the fact that the 1 Hz harmonics are very faint lines. The provided list of known disturbances includes not only lines which affect the data in terribly bad ways. It contains frequencies in which the data *may* be corrupted and hence, require appropriate attention. Some disturbances are known to be very strong, like the calibration lines. Candidates within these frequency bands clearly have to be discarded. However, this does not hold for the 1 Hz harmonics. Figure 6.1.5 shows random samples of frequency bands around multiples of 1 Hz. Each plot shows the resulting $\langle 2\mathcal{F} \rangle$ values of a search that used the same setup as the original search job that covered the corresponding frequency, but with the Doppler demodulation turned *off*. That is, the used analysis program is sensitive to stationary lines. The red solid lines show the center of the 1 Hz harmonics. Only in two plots are the lines visible at all. However, they are very sharp lines where increased $\langle 2\mathcal{F} \rangle$ values appear to show up only in a single frequency bin. The largest value is small ($<\ 4.8$). Comparing this with Figure 6.1.4 shows that the 1 Hz lines are clearly very weak lines. Of course, the shown lines present only a sub-group of all 1 Hz harmonics, but they give an idea of their typical strength. Having in mind that the standard search is much less sensitive to stationary lines, we conclude that the 1 Hz harmonics have negligible impact on the search results.

Based on these studies the line cleaning procedure is relaxed for the 1 Hz harmonics. In particular, all candidates with frequency and spindown values such that no more than 30% of the data used for the analysis of the candidate is potentially contaminated by a 1 Hz line are kept. One could easily argue for a larger threshold than 30%, given the negligible impact of the spectral lines. As a measure of safety, all candidates which pass this procedure only due to the relaxation of the line cleaning are labeled. Further investigations can then fold in that information, if necessary. Since the 1 Hz lines are the only artifacts with such major impact on the number of surviving candidates, the other known spectral lines can be vetoed conservatively.

After applying the flexible known lines cleaning, $889\,650\,421$ (about 83% of the) candidates are left. Figure 6.1.6 shows the number of candidates kept over
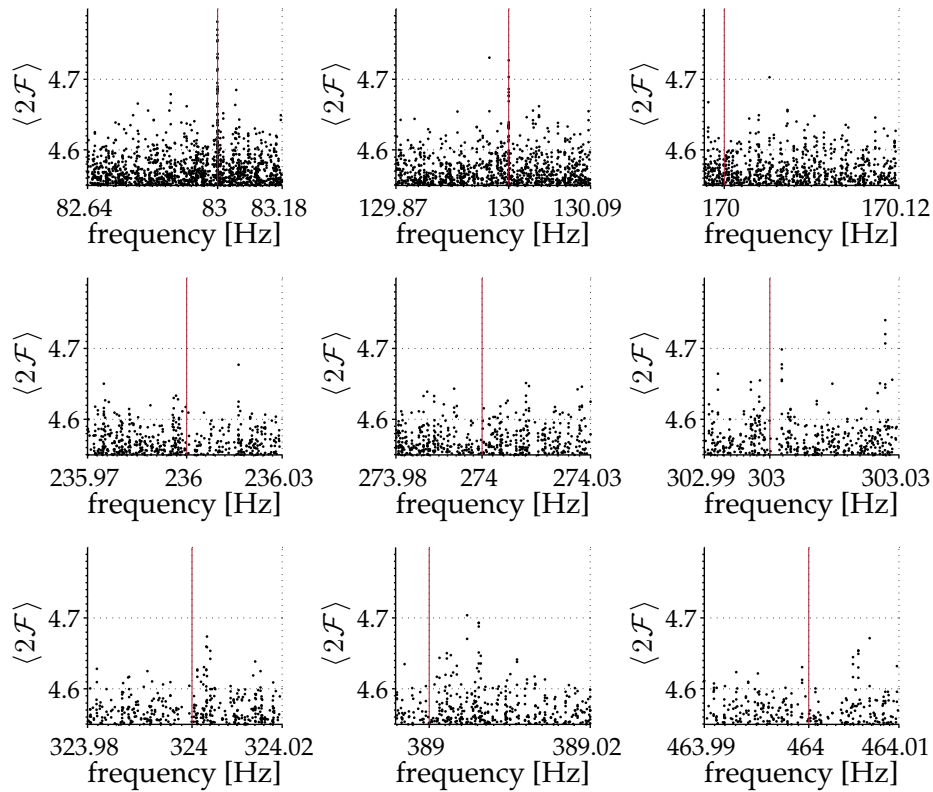
Figure 6.1.5: The nine sub-figures show random samples of frequency bands around 1 Hz harmonics. The plotted candidates are the result from nine test searches of the frequency regions around the 1 Hz harmonics with the Doppler demodulation turned off. That is, the search is more sensitive to stationary lines than the standard search. In each plot the result of one search job is plotted. The red solid lines mark the central frequency of each harmonic. Strong instrumental artifacts would be visible through an accumulation of candidates with increased $\langle 2\mathcal{F} \rangle$ values, close to the central frequency of the harmonic. In two of the random examples (at 83 and 130 Hz) a sharp line with increased $\langle 2\mathcal{F} \rangle$ values is visible. However, the maximum values they reach are below 4.8. For comparison, the maximum value obtained in the injection study (Figure 6.1.4) resulted in $\langle 2\mathcal{F} \rangle$ values of the order 11. We conclude that the 1 Hz lines are very weak lines that have negligible effect on the search results.
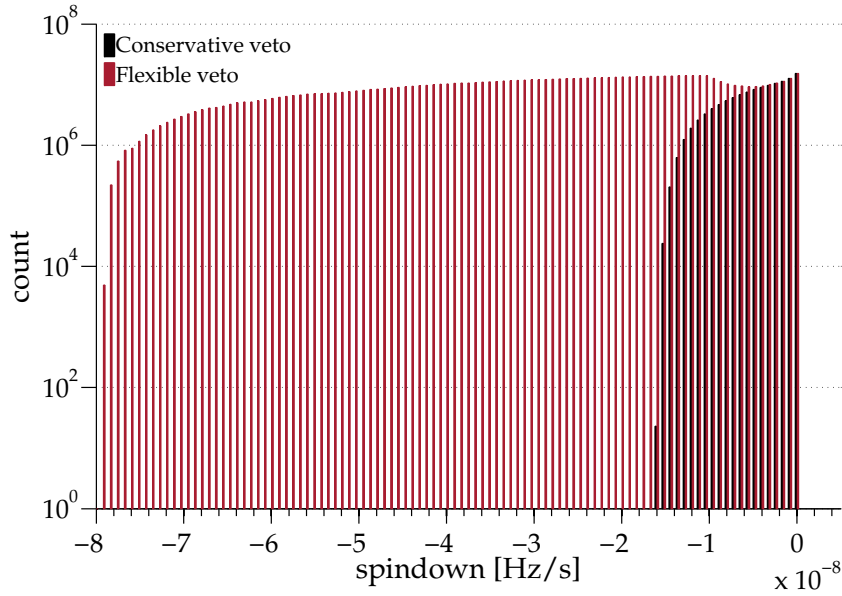
Figure 6.1.6: The histograms illustrate the benefit of the flexible known lines cleaning procedure: the black histogram contains all remaining candidates after the conservative known lines cleaning, the red histogram contains all candidates after the flexible known lines cleaning. The small sink at $\sim -1 \times 10^{-8}$ Hz/s $\leq \dot{f} \leq 0$ Hz/s is due to the remaining effect of the 1 Hz lines.

spindown for both the conservative and the flexible known lines cleaning procedure applied to the list of candidates and illustrates the benefit of the improved procedure. A small depression in the red histogram for spindown values $\sim -1 \times 10^{-8}$ Hz/s $\leq \dot{f} \leq 0$ Hz/s is due to the remaining effect of the 1 Hz line cleaning.

6.2   Clustering of Candidates

A gravitational wave signal will produce significant values of the detection statistic not only at the template with the best parameter match, but also at the neighboring templates in frequency and spindown. Figure 6.2.1 shows the values of the detection statistic in frequency-spindown space resulting from a search on data containing an injected signal and no noise.

The basic appearance of the plot does not change with the sky position, frequency or spindown within the searched parameter space. Only the strength of the
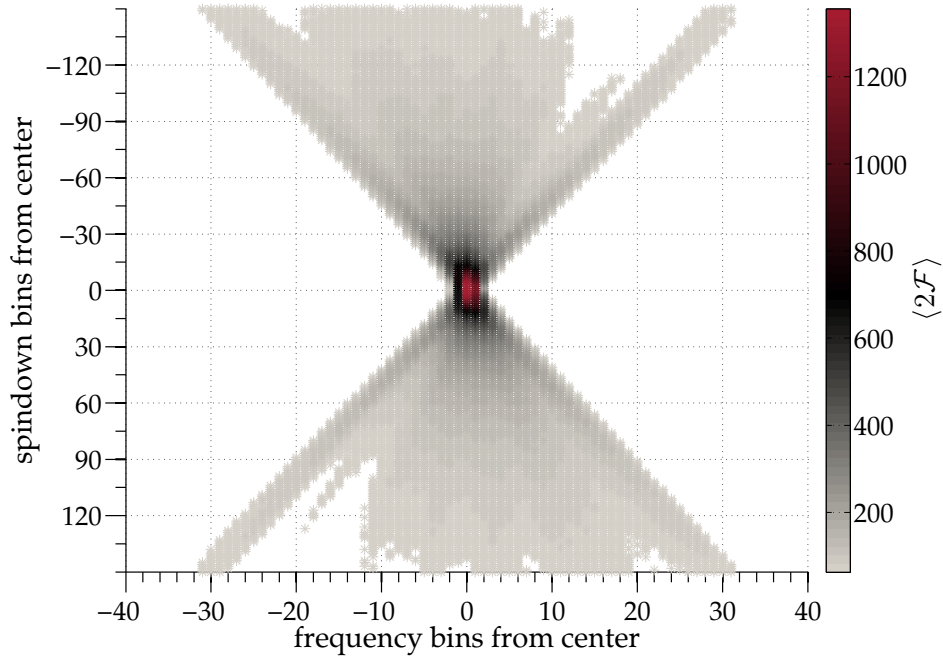
Figure 6.2.1: The figure shows a typical signal in the frequency-spindown plane. The $\langle 2\mathcal{F}\rangle$ values are color-coded. The central part of the signal that contains all candidates with $\langle 2\mathcal{F}\rangle$ values larger than $0.5\langle 2\mathcal{F}\rangle_{\mathrm{max}}$ has the shape of a rectangular box with the loudest candidate being at the center.

injected signal influences the outcome, changing the number of affected templates. That is, a signal in Gaussian noise appears shrunken or expanded in frequency-spindown space. However, the key features of the structure remain. Figure 6.2.1 demonstrates that a great number of templates have increased $\langle 2\mathcal{F}\rangle$ values due to the same signal. We have to assume that multiple candidates in the resulting candidates top lists of the search can be ascribed to the same origin as well. Therefore, it is reasonable to group multiple candidates which likely originate from the same cause and keep only a single representative candidate. This procedure effectively reduces the total number of candidates, which is desirable for the subsequent post-processing.

The following clustering procedure is implemented: from the list of all candidates surviving the known lines cleaning the candidate with the largest $\langle 2\mathcal{F}\rangle$ value is taken and chosen to be the first representative for the first cluster. All candi-

dates that lie within a predefined distance in frequency and spindown (this will be explained later) are associated with this cluster. Those candidates are removed from the list. Among the remaining candidates the one with the largest $\langle 2\mathcal{F} \rangle$ value is identified and taken as the representative of the second cluster. Again, all candidates within a certain distance are associated to that cluster and removed from the list. This procedure is repeated until all candidates have either been chosen as representatives or are associated to a cluster.

To obtain the cluster box dimensions in frequency and spindown, 200 different realizations of continuous gravitational wave signals without noise are created and the data analyzed with the standard search technique. Then the distance distribution between the most significant candidate and the candidates with a detection statistic value no less than half of the most significant one is studied. Figure 6.2.2 shows the results. The upper plot shows the distribution of the distances in frequency bins, the lower plot that in spindown bins. In all cases, the candidates of interest are located within three frequency bins from the representative. The number of candidates increases quickly to $> 99\%$ within the first two bins. Less clear is the shape of the second plot. A steep slope towards high percentages is again visible, but this time with a saturation that starts at the ~ 12th bin from the representative's spindown value. $> 90\%$ of the templates that pass the 50% threshold are included already within the inner 12 bins. This saturation then stretches out for 24 further bins until it finally reaches the 100% mark. Different options exist now: the box size could be set to 2 frequency bins $\times 13$ spindown bins. This would be a very conservative approach with a "soft" reduction of the total number of candidates. On average, this cluster size contains only $\sim 90\%$ of the templates that pass the 50% threshold. Another option would be to set the box size to 3 frequency bins $\times 36$ spindown bins. This box size contains *all* templates with $\langle 2\mathcal{F} \rangle$ values that cross the threshold and the total number of candidates left after the clustering procedure is applied would decrease drastically. Another option is a setup somewhere in between these two extrema.

The decision is made in favor of a compromise between the two options: the size of the cluster box is defined as 2 frequency bins and 25 spindown bins to both sides of the representative candidate. This box covers about 70% of the box with
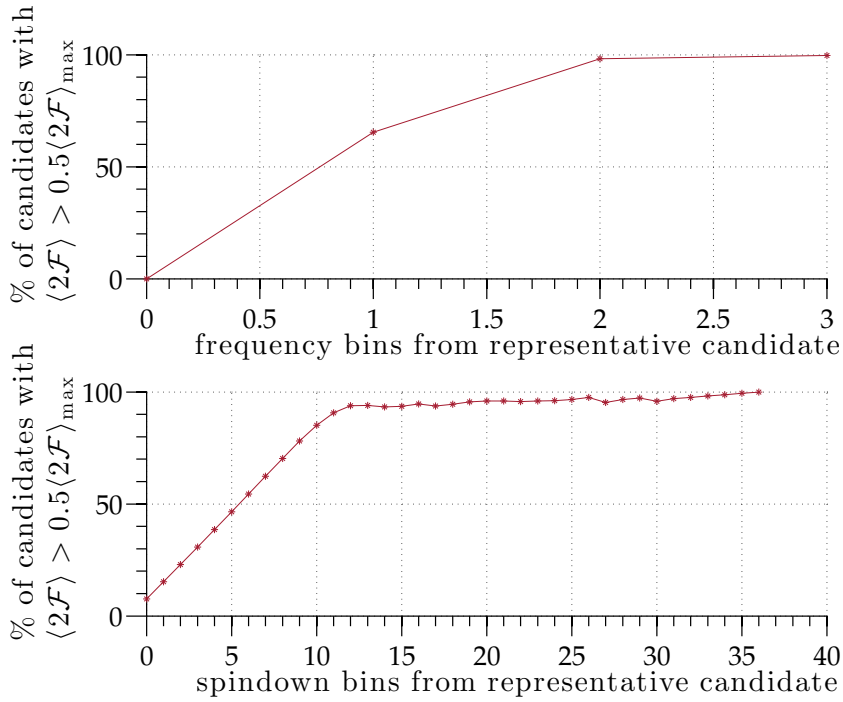
Figure 6.2.2: The plot shows the fraction of candidates with $\langle 2\mathcal{F} \rangle$ values larger than half of maximum as a function of frequency (top) and spindown (bottom).

the most effective values (3×36). The number of spindown bins (25) is found to be right in the center of the saturation area. With this choice we believe to have found the best compromise between effectiveness and safety.

Figure 6.2.3 shows the same gravitational wave signal that was already presented in Figure 6.2.1. This time it shows a zoom into the center of the signal and contains an additional frame that denotes the cluster box. All candidates with frequency and spindown parameters within this box are ascribed to the representative candidate. While in the above discussion, the size on the cluster box appeared to be conservatively small, in this example all candidates with values $\langle 2\mathcal{F} \rangle \gtrsim 700$ are well within the box.

After applying the clustering procedure to the list of candidates the total number of candidates left for further post-processing checks is reduced to $296\,815\,037$ representatives which is about $\sim 28\%$ of the total number of candidates and $\sim 33\%$ of the candidates left after the flexible known lines cleaning procedure.
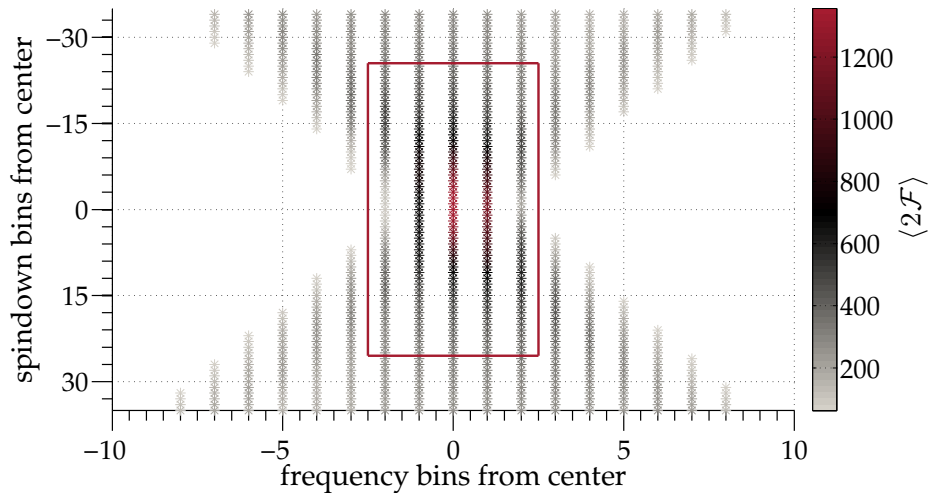
Figure 6.2.3: The figure shows again the gravitational wave signal from Figure 6.2.1. This time zoomed into the center of the signal, with the clustering box added as the red frame. All candidates that are within this box are ascribed to the representative candidate.

6.3   The $\mathcal{F}$-Statistic Consistency Veto

After reducing the number of candidates by applying the clustering procedure, $\sim 3 \times 10^8$ candidates are left to be investigated. The $\mathcal{F}$-statistic consistency veto provides a powerful test to unveil terrestrial disturbances that show up as candidates with large $\langle 2\mathcal{F} \rangle$ values by requiring consistency among separate results from the two interferometers involved in the analysis. Local disturbances are more likely to affect the data record of only one detector or at least (in case of an earthquake or storm) show up with different strengths in the two detectors. In contrast, a gravitational wave will be visible in the data of both detectors with consistent properties.

The veto itself is very simple: for each of the candidates the single-interferometer $\langle 2\mathcal{F} \rangle$ values are computed. The results are compared with the initial multi-interferometer $\langle 2\mathcal{F} \rangle$ result. If any of the single-interferometer values is higher than the multi-interferometer value we conclude that its origin is local and the associated candidate is ruled out as being due to a gravitational wave.

After applying this veto the list of candidates for further post-processing con-

tains $261\,655\,549$ candidates, $\sim 25\%$ of the total number of candidates. About 12% of the cluster representatives are vetoed.

FALSE DISMISSAL AND VETO SAFETY

The veto was tested on the set of test injections as described in Table 6.0.1 with signal strengths of $h_0^{90\%}$ and with the other parameters randomly distributed within the search parameter space. None of the 500 signal injections is vetoed. That is, the false dismissal rate of this veto is $< 0.2\%$ for the tested population of signals. This confirms the robustness of the veto, which is, at the same time, reducing the number of candidates by $\sim 12\%$. This veto has been used in past searches [3, 29].

6.4 SETTING A SIGNIFICANCE THRESHOLD

After the $\mathcal{F}$-statistic consistency veto $261\,655\,549$ candidates are left for further investigations. This is a too large number for the further post-processing steps that are performed, so we concentrate on a significant subset of these candidates. Candidates are defined significant if their $\langle 2\mathcal{F} \rangle$ value is above the expectation value for the loudest expected candidate in Gaussian noise minus three standard deviations, assuming all templates as independent. The expectation value for the largest $\langle 2\mathcal{F}^* \rangle$ value and its variance over $N = 4\,355\,231\,668\,681$ independent trials on Gaussian noise is (see Section 5.8.2):

$$E\left[\langle 2\mathcal{F}^* \rangle\right] = 4.881 \quad \text{and} \quad \sigma^2\left[\langle 2\mathcal{F}^* \rangle\right] = 0.036. \tag{6.1}$$

Figure 6.4.1 shows the probability density function (Equations 5.27 and 5.28) of the highest value of the $\langle 2\mathcal{F} \rangle$-statistic, $\langle 2\mathcal{F}^* \rangle$, for Gaussian noise. The solid black line denotes the expectation value $E\left[\langle 2\mathcal{F}^* \rangle\right]$. The threshold that separates *significant* candidates from *non-significant* candidates is then defined as the expectation value of $\langle 2\mathcal{F}^* \rangle$ minus three standard deviations, $E\left[\langle 2\mathcal{F}^* \rangle\right] - 3\sigma = 4.773$, denoted in the plot by the dashed black line. All candidates with $\langle 2\mathcal{F} \rangle$ values below that threshold are not considered in further investigations. This reduces the remaining number of candidates significantly to 27607.
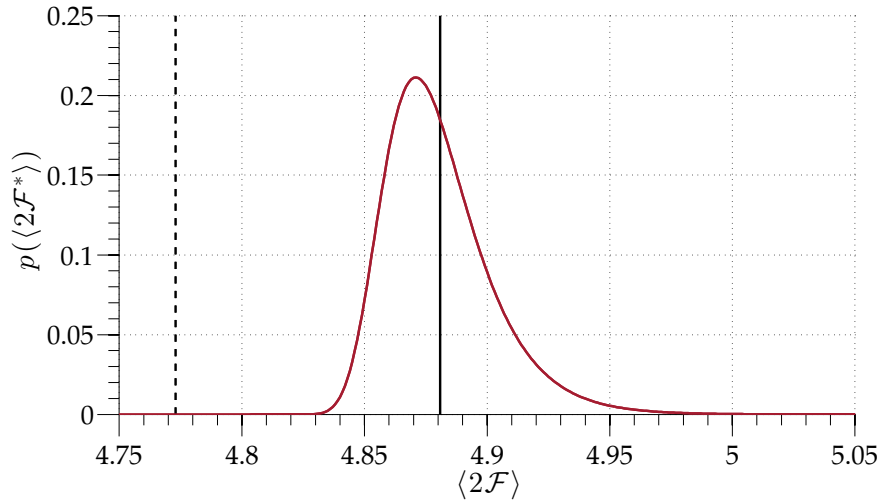
Figure 6.4.1: The plot shows the probability density function for Gaussian noise of the highest $\langle 2\mathcal{F}\rangle$ value over $N \sim 4.4 \times 10^{12}$ trials, $p(\langle 2\mathcal{F}^*\rangle)$. The solid black line denotes the expectation value, $E\left[\langle 2\mathcal{F}^*\rangle\right] = 4.881$ and the dashed black line the significance threshold that is three standard deviations below the expectation value.

The exact value of the threshold is a compromise between efficiency and the desire to investigate candidates with as low $\langle 2\mathcal{F}\rangle$ values as possible. It could be lowered further, but for even lower $\langle 2\mathcal{F}\rangle$ values it would be very hard to set up an appropriate follow-up search[2].

FALSE DISMISSAL

The selection of a significant subset is not a veto, because the candidates with lower $\langle 2\mathcal{F}\rangle$ values are not ruled out as gravitational wave candidates. Therefore it is not appropriate to give a false dismissal rate. Nevertheless, it is interesting to investigate what fraction of the injected signal population passes this selection. Therefore, the selection is also applied to the set of 500 test signals and four of them are lost.

---

[2]If even weaker $\langle 2\mathcal{F}\rangle$ values need to be investigated, longer data stretches are necessary for the follow-up in order to reach significant $2\mathcal{F}$ result values. Longer observation times increase the number of templates which, in turn, increases the largest expected values in Gaussian noise. This prevents weak signals to stand out from the background. Also data spans longer than the provided data might be necessary. And even if such data were available, such a search would be computationally very intensive.

That is, 0.8% of the signal injections are lost at this stage.

Discussion

In the process of this research the author was often asked why this step was performed at such a late stage of the post-processing. The main argument in favor of an early application of this threshold is that valuable computation time could have been saved. In principle, of course, this is true. Applying the selection first of all would have avoided spending computation time on the steps that have been performed so far on the non-significant candidates. But this is not what was done, because the goal of this work has always been to try and consider candidates with as low $\langle 2\mathcal{F} \rangle$ values as possible to increase the chance of a detection. We do not expect to find a gravitational wave signal with large significance – such signals would have been detected by the all-sky searches. Instead we believe that less strong signals are more likely to be present in the data. Therefore, the decision was made in favor of a late application of this selection step, which allowed us to tune this threshold according to the available set of candidates and computation power. An early application of this selection, for example as a first step, could have resulted in a higher threshold and a shorter list of potential gravitational wave signals to post-process. It is questionable that we would have gone back to adjust the threshold and repeat all subsequent steps. Furthermore, it is interesting to have a larger data set for further investigation of the vetoes on a broad range of candidates.

6.5 The Segment Resolution Veto

The search reports back the average over the 630 $2\mathcal{F}$-statistic values computed for each data segment (see Section 4.4). The relative weight of the different contributions to this average is invisible. This information is important, though, because it gives insight into the nature of a candidate. A continuous gravitational wave signal will be present throughout the whole observation time of almost two years, while terrestrial disturbances are usually of much shorter duration. However, a strong enough disturbance can determine a large $\langle 2\mathcal{F} \rangle$ value, even though only few segments effectively contribute to it. The following veto aims at uncovering extreme behaviors of this type and discard the associated candidates.

It is very difficult to get information about the properties of such disturbances, as it is not possible to simulate them without prior knowledge. It is unknown to us for how long such disturbances last on average and, hence, how many segments typically are affected. After extensive manual studies of the remaining few thousand candidates, it turns out that in most cases only one single segment shows a suspiciously large $2\mathcal{F}$ value. The overabundance of candidates showing such specific property finally yields in the definition of this veto: for all candidates the 630 data segments are coherently analyzed, giving 630 single $2\mathcal{F}$ values. The highest value is removed and a new average over the remaining 629 segments is computed and compared to the significance threshold (see Section 6.4). Candidates with a reduced average value that is not significant anymore are discarded[3]. Figure 6.5.1 shows a typical example of a candidate whose resulting $\langle 2\mathcal{F}\rangle$ value was caused by only one single segment which had a tremendously large $2\mathcal{F}$ value.

Applying the segment resolution veto reduces the number of candidates for further post-processing from 27607 to 1138 candidates (about 4%). This veto is simple but very effective because, in fact, most of the loud spectral disturbances in the data are rather short lived. The remaining candidates are investigated in a follow-up search (see Section 6.6).

FALSE DISMISSAL AND VETO SAFETY

This veto was applied to the set of 496 injected signals which are left after applying the significance threshold. None of the signals is discarded by this veto and, therefore, the false dismissal rate for the given signal population is $< 0.2\%$.

---

[3]The veto presented here appears to be very simple. This is the result of a time consuming study which also included second order spindown signals. Although those signals are not targeted by this search, they play an important role in astrophysical models that predict gravitational wave emission for high spindown signals such as those we search for (further discussion on second order spindown signals can be found in Chapter 8). The long way that finally led to the definition of this veto shall not be given in detail here, but the interested reader can find information in Appendix A.7.
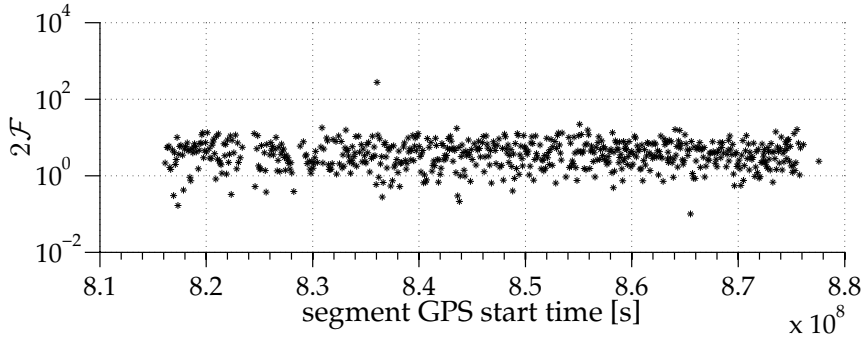
Figure 6.5.1: A typical candidate that gets vetoed by the segment resolution veto. The plot shows the $2\mathcal{F}$ values of a single candidate, calculated for the 630 data segments, over the start time of each segment.

6.6 THE COHERENT FOLLOW-UP SEARCH

The final list of candidates that can not be ruled out as gravitational wave signals contains 1138 candidates. Figure 6.6.1 shows the analysis result of Gaussian data with an additional injected gravitational wave signal (its position is denoted by the yellow star) with a strength at the detectability limit (*below* the upper limit $h_0^{90\%}$), $h_0 = 3 \times 10^{-25}$. Its maximum $\langle 2\mathcal{F} \rangle$ value of 4.72 is below the significance threshold of 4.773 (see Section 6.4). The shape of the signal is less symmetric and clear than that of a strong signal (compare Figure 6.2.1) but still shows a central maximum with an accumulation of templates around it. White space denotes templates whose $\langle 2\mathcal{F} \rangle$ values were too low to make it into the top list of parameter space points returned by the job. The bottom line of this plot is to show that gravitational wave signals might be inside the data but too faint to show up with significant $\langle 2\mathcal{F} \rangle$ values. Such weak signals are even more likely to exist than signals that show up with large significance.

The used hierarchical analysis technique is a powerful way to analyze large numbers of templates, but, as discussed in Section 5.7, this benefit comes at the cost of reduced sensitivity. A hierarchical analysis does not recover weak signals with the same significance as a coherent search technique could do, also it does not estimate the parameters of a signal as precisely as a coherent analysis would. Therefore, the
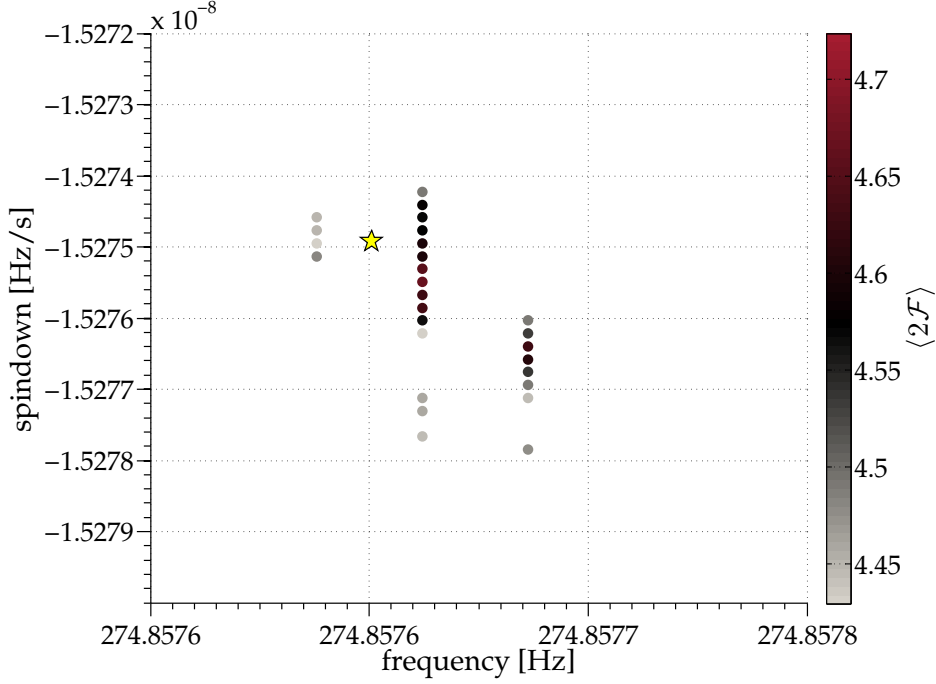
Figure 6.6.1: A faint gravitational wave signal, injected with at frequency $f = 274.85765$ Hz and spindown -1.52749×10^{-8} Hz/s with a strength of $h_0 = 3 \times 10^{-25}$ into Gaussian data shows up with insignificant $\langle 2\mathcal{F} \rangle$ values. The maximum $\langle 2\mathcal{F} \rangle$ value within this structure is 4.72, which is below the significance threshold. Such weak signals are more likely to exist in the data than strong signals that result in significant $\langle 2\mathcal{F} \rangle$ values.

remaining candidates are tested with a coherent follow-up search[4]. The increased sensitivity of the coherent follow-up search can be used to rule out candidates as gravitational wave signals that fall short of the projected detection statistic value: for a given $\langle 2\mathcal{F} \rangle$ value under certain assumptions it is possible to calculate the expected $2\mathcal{F}_{\text{coh, exp}}$ result of a follow-up search. The follow-up search is performed and the ratio of the loudest candidate found, $2\mathcal{F}_{\text{coh}}^*$, and the expected value is computed:

$$\mathcal{R} = \frac{2\mathcal{F}_{\text{coh}}^*}{2\mathcal{F}_{\text{coh, exp}}}. \tag{6.2}$$

A threshold $\mathcal{R}_{\text{thr}}$ is set on $\mathcal{R}$ and the candidates with $\mathcal{R} < \mathcal{R}_{\text{thr}}$ are ruled out as

---

[4]The used analysis program is called `lalapps_ComputeFStatistic_v2` and is available as part of the LALSuite, also see Appendix A.2.

gravitational wave candidates. In the following sections the details of this follow-up search and the determination of the threshold $\mathcal{R}_{\text{thr}}$ are described.

6.6.1   ESTIMATING $2\mathcal{F}_{\text{COH, EXP}}$

As mentioned above, having $\langle 2\mathcal{F} \rangle$ from the original search makes is possible to estimate the outcome of the coherent follow-up search. The expected $2\mathcal{F}$ value is composed of the number of degrees of freedom (in this case four) plus the non-centrality parameter, λ^2, which is the SNR, hence, gives a measure of the strength of a signal (see Section 4.3). λ^2 scales linearly with the observation time. A candidate that results in a value $\langle 2\mathcal{F} \rangle$ in the initial analysis using the amount of data T_{seg} in each segment is expected to show up with $2\mathcal{F}_{\text{coh, exp}}$ in the coherent analysis using T_{coh} data:

$$2\mathcal{F}_{\text{coh, exp}} \simeq \left(\langle 2\mathcal{F} \rangle - 4 \right) \frac{T_{\text{coh}}}{T_{\text{seg}}} + 4. \qquad (6.3)$$

As discussed in Section 5.5.1, the 630 data segments used for the original search were selected based on their predicted $\langle 2\mathcal{F} \rangle$ values. The result is a set of data segments during which the coupling between the detector and the source was particularly good. This results in increased $\langle 2\mathcal{F} \rangle$ values for signals to what would have been obtained otherwise. A simple extrapolation of these $\langle 2\mathcal{F} \rangle$ values, to predict the result of a fully coherent search, implicitly folds in the assumption that this data quality applies also to the follow-up search. This assumption does not hold for the coherent search data set, which is a contiguous span over many weeks. To quantify this effect on $2\mathcal{F}_{\text{coh, exp}}$ an *antenna pattern correction* κ is computed and folded in at the calculation of the expected $2\mathcal{F}_{\text{coh, exp}}$ value. κ is the ratio between the sum over the antenna pattern functions (Equation 4.5) for each SFT used by the coherent follow-up search i and the original search j, respectively:

$$\kappa = \frac{\sum_i \left(F_+^2 + F_\times^2 \right)_{i,\text{coh}}}{\sum_j \left(F_+^2 + F_\times^2 \right)_{j,\text{orig}}} \qquad (6.4)$$

The antenna pattern correction can now be added to Equation 6.3 and the expected

$2\mathcal{F}_{\text{coh, exp}}$ value can be computed with:

$$2\mathcal{F}_{\text{coh, exp}} = \kappa \cdot \left(\left(\langle 2\mathcal{F} \rangle - 4 \right) \frac{T_{\text{coh}}}{T_{\text{seg}}} \right) + 4. \qquad (6.5)$$

6.6.2   THE TEMPLATE SETUP

The parameters of the candidate are only approximations of the real signal's parameters. As was shown in Section 6.2, in the hierarchical analysis in the presence of a loud signal, multiple neighboring templates show increased $\langle 2\mathcal{F} \rangle$ values. In fact, the candidates are each a representative of a cluster that extends ± 2 frequency bins and ± 25 spindown bins on either sides of its nominal parameters. The true signal parameters are expected to lie within this cluster-box. A natural choice is to perform the follow-up search covering this parameter space region, but this adds a large number of templates to the coherent search, hence increasing the computational cost and the expected $2\mathcal{F}$ value in Gaussian noise. Since the cluster dimensions were determined based on a generic maximum SNR loss of 50% we decided to study the distance distribution of recovered signals with respect to the actual signal parameters.

A Monte-Carlo study is performed in which 100 signals with frequency, spindown and nuisance parameters $(\psi, \phi_0, \cos\iota)$ are randomly distributed within the search parameter space. The gravitational wave signal injections have a random mismatch in sky position up to $R \leq 10^{-3}$ rad. The noise is fake Gaussian data. The strength of the signals varies between 2×10^{-25} and 3.5×10^{-25}. These values correspond to resulting $\langle 2\mathcal{F} \rangle$ values around ~ 5 on average[5]. The data are searched with the template grid resolution of the initial search (see Equation 5.15) in a box of 50 frequency bins and 100 spindown bins centered around the injection. Then the distance in frequency and spindown between the loudest candidate and the injection parameters is evaluated. The distributions of these distances are shown in the histograms in Figure 6.6.2 for frequency and spindown bins, respectively. In all cases, the distance is smaller or equal to two frequency and five spin-

---

[5]At the time this study was performed, the $h_0^{90\%}$ value was not yet derived. The deviation of the resulting $\langle 2\mathcal{F} \rangle$ values is quite large, mostly because the signal strength is arbitrarily distributed indpendent on the frequency.
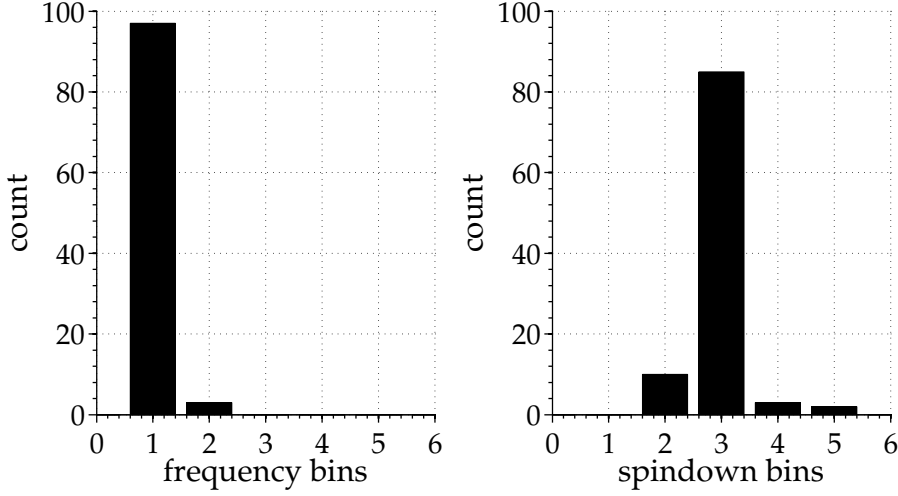
Figure 6.6.2: The two histograms show the distances between the highest template and the injection in frequency and spindown bins, respectively.

down bins. Consequently, the frequency and spindown ranges for the coherent follow-up search are set to be:

$$\Delta f = 5\,\delta f = 5\,T_{\text{seg}}^{-1},$$
$$\Delta \dot{f} = 11\,\delta \dot{f}_{\text{fine}} = 11\,\gamma^{-1}T_{\text{seg}}^{-2}. \tag{6.6}$$

This region in parameter space is covered by a refined template grid (with respect to the original template grid), with resolutions given by:

$$\delta f_{\text{coh}} = \left(2\,T_{\text{span,coh}}\right)^{-1}, \quad \delta \dot{f}_{\text{coh}} = \left(2\,T_{\text{span, coh}}^2\right)^{-1}. \tag{6.7}$$

The resolution in spindown is comparable to the fine grid resolution of the initial search. The frequency resolution, however, is much finer. This results in $N_f = 1879$ frequency and $N_{\dot{f}} = 241$ spindown templates.

In the initial search, a single sky template covers the full area of $R \lesssim 8\,\text{pc}$ around the template's parameters (see Section 5.6.1). The same does not apply for the coherent search, hence, a small sky grid is placed around the coordinates of Sgr A*. A Monte-Carlo study is performed to investigate the effect of mismatches in the sky position on the computed $2\mathcal{F}_{\text{coh}}$ values: 100 signals with uniformly distributed
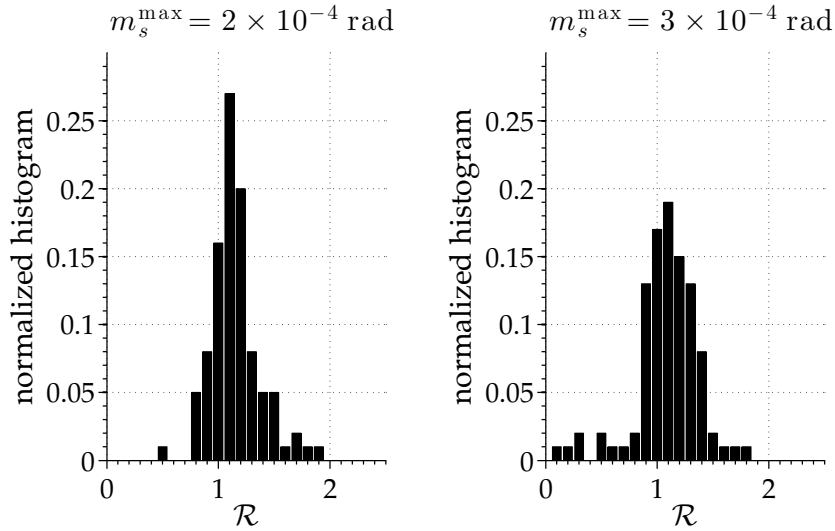
Figure 6.6.3: The plots show the distributions of $\mathcal{R}$ for two example studies. The left histogram was created with the results from a study where the maximum mismatch in sky position was 2×10^{-4} rad, the right histogram with a maximum allowed sky mismatch of 3×10^{-4} rad.

parameters within the search parameter space are injected into Gaussian data. The data is then analyzed first with the hierarchical search technique and then coherently in the region defined by Equation 6.6 around the injection, using a template grid with resolutions defined in Equation 6.7, and the loudest candidate is recovered. This analysis is conducted nine times with different mismatches in sky position between the injection and the template: first, without any sky mismatch, then, in each repetition, with an allowed maximum sky mismatch increased by 10^{-4} rad with respect to the previous turn. After each analysis $\mathcal{R}$ is computed. Figure 6.6.3 shows the distributions of two example runs: the one with $m_s^{\mathrm{max}} = 2 \times 10^{-4}$ rad and the one with $m_s^{\mathrm{max}} = 3 \times 10^{-4}$ rad. These two were chosen because the transition from acceptable to unacceptable sky mismatch takes place: while the distribution of $\mathcal{R}$ for a mismatch in sky position of $m_s^{\mathrm{max}} = 2 \times 10^{-4}$ rad is still quite narrow with a clearly located peak, the histogram for $m_s^{\mathrm{max}} = 3 \times 10^{-4}$ rad is much broader and less nicely shaped. For larger mismatches this effect increases. Having in mind that a threshold shall be set on $\mathcal{R}$, the mismatch in sky position should be no larger than $m_s^{\mathrm{max}} = 2 \times 10^{-4}$ rad.

The dimension and resolution of the sky grid used for the coherent follow-up search is a compromise between large sky coverage, a desired small number of templates, an acceptable sky mismatch and the limitation of computational resources. Covering the full region of 8 pc around Sgr A* is computationally infeasible. Also, the number of templates would vastly increase, leading to a high expected value $2\mathcal{F}^*_{\mathrm{coh}}$ for Gaussian noise. Therefore, the covered region is limited to $R \lesssim 3$ pc around the coordinates of Sgr A*[6], which translates into 7.2×10^{-4} rad in both right ascension and declination, centered around the Galactic Center. Dividing this region into 36 equally spaced sky points leads to an acceptable resolution of 1.2×10^{-4} rad which doesn't degrade the mismatch performance.

The total number of templates $N_{\mathrm{coh}} = N_f \times N_{\dot{f}} \times N_{\mathrm{sky}} = 16\,302\,204$ yields a largest expected $2\mathcal{F}^*_{\mathrm{coh}}$ value in case of purely Gaussian noise and, under the assumption that the N_{coh} templates are independent of $2\mathcal{F}^*_{\mathrm{coh,\,exp}} = 40 \pm 4$. The assumption that the templates are independent, however, does not hold for the chosen template grid and, hence, it slightly overestimates the actual expected value. The *effective* number of independent templates can be estimated by a fit of the actual distribution. The actual distribution is obtained by a Monte-Carlo study in which 1000 different realizations of purely Gaussian data are analyzed, using the template setup of the coherent follow-up search. Figure 6.6.4 shows the distribution of the largest $2\mathcal{F}^*_{\mathrm{coh}}$ found in each analysis. The measured mean value is 35 ± 3. Thus, the effective number of templates can be estimated to be roughly $N_{\mathrm{eff}} \sim 0.1\,N_{\mathrm{coh}}$.

6.6.3 THE REQUIRED OBSERVATION TIME

The main requirement for the follow-up search to succeed is that the setup allows a signal to stand out from the noise with high significance. The largest value expected in the case of Gaussian noise is $\sim 35 \pm 3$, as was discussed in Section 6.6.2. The 1σ-uncertainty of the predicted value $2\mathcal{F}_{\mathrm{coh,\,exp}}$ can empirically be estimated to be of the order 20%. In order to stick out clearly from the noise a signal should therefore be recovered with high significance, for example reach values of $2\mathcal{F}_{\mathrm{coh}} \sim$

---

[6]This includes all three parts of Sgr A: the inner center, the minispiral of Sgr A West and the supernova remnant Sgr A East (see Section 2.3).
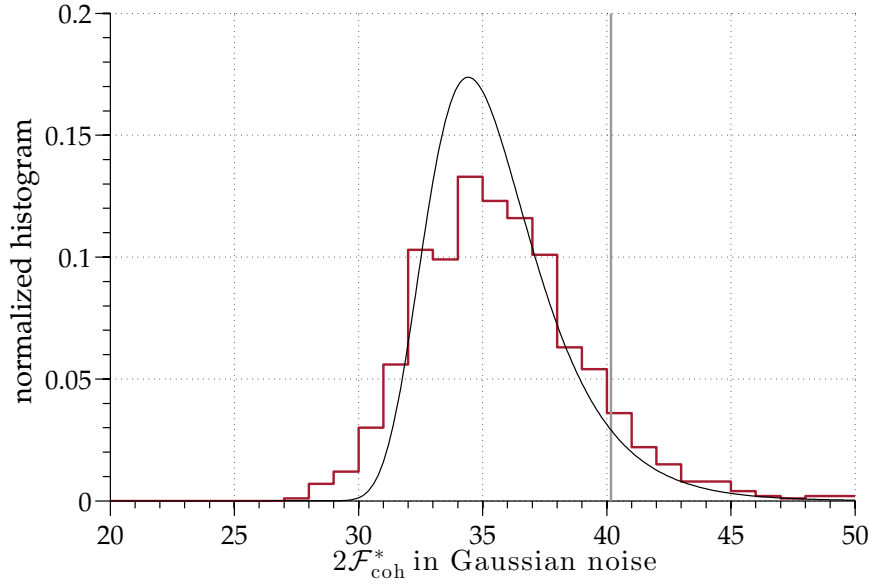
Figure 6.6.4: The histogram shows the distribution of the resulting maximum $2\mathcal{F}^*_{\text{coh}}$ values of the coherent analysis of 1000 different realizations of pure Gaussian noise, using the coherent follow-up template spacings (red line). The measured mean value of this distribution is 35 ± 3, which is lower than the predicted value of $2\mathcal{F}^*_{\text{coh, exp}} = 40 \pm 4$ (gray line). The reason is the dependency of the templates. The number of effective independent templates can be estimated by to $N_{\text{eff}} \sim 0.1 \, N_{\text{coh}}$ (black line).

110 in the coherent follow-up search. Rearranging Equation 6.5 and inserting the required value of 110 for $2\mathcal{F}_{\text{coh, exp}}$ gives the required minimum observation time for the coherent follow-up search:

$$T_{\text{coh}} \simeq \frac{(110 + 4)}{(\langle 2\mathcal{F}\rangle - 4)} \frac{T_{\text{seg}}}{\kappa}. \tag{6.8}$$

For signals that resulted in $\langle 2\mathcal{F}\rangle$ values around ~ 4.8 and for an expected $\kappa \sim 0.7$ (this choice will be confirmed below) this results in $T_{\text{coh}} \sim 90$ days.

The chosen data set for the follow-up search comprises data from the H1 and L1 detectors and spans the time between February 01, 2007, at 15:02 GMT and May 02, 2007, at 15:02 GMT. It contains a total of 6522 SFTs (3489 from H1 and 3033 from L1) which is an average of 67.9 days from each detector. The data is chosen by the same procedure as described in Section 5.5.1, but this time set $\mathcal{C}$

is created by grouping the SFTs into segments of 90 days. Neighboring segments overlap each other by $24\,\text{h}$. The antenna pattern correction for this data set can be computed with Equation 6.4 and results in:

$$\kappa = 0.68. \qquad (6.9)$$

6.6.4   DEFINING THE THRESHOLD $\mathcal{R}_{\text{THR}}$

As explained in Section 6.6.2, a candidate is kept as a potential gravitational wave signal when $\mathcal{R} > \mathcal{R}_{\text{thr}}$. The threshold is obtained empirically by running a Monte-Carlo study with 1000 signal injections in Gaussian noise. The parameters of the different realizations of the signal injections are randomly distributed within the parameter space of the initial search. Two separate data sets are created within this study: one that matches the original data set (in terms of SFT start times) and one that matches the 90-day coherent data set. The strength of the signals varies between 2×10^{-25} and 2.5×10^{-25}. Analyzing the first data set with the original search results in $\langle 2\mathcal{F} \rangle$ values for the recovered signals between 4.35 and 7.30 with a mean value of 5.17. The analysis of the second data set with the coherent follow-up search (as described above) results in $2\mathcal{F}_{\text{coh}}$ values with a mean of ~ 137. Figure 6.6.5 shows the distribution of the resulting values of $\mathcal{R}$. The plot shows that $\mathcal{R} < 0.5$ for only four out of the 1000 injected signals, hence, the threshold is defined as $\mathcal{R} = \mathcal{R}_{\text{thr}} = 0.5$. This implies a false dismissal rate of 0.4%.

6.6.5   FALSE ALARM OF $\mathcal{R}_{\text{THR}}$

Although the coherent follow-up search is defined to *rule out* candidates as gravitational wave signals rather than *confirming* any detection, a candidate that passes this test would be exciting. To estimate the chance of a false alarm event a Monte-Carlo study is performed on purely Gaussian data. The most conservative false alarm probability is obtained by assuming that the candidates has an original $\langle 2\mathcal{F} \rangle$ value at the significance threshold. Such a candidates represents the lowest $\langle 2\mathcal{F} \rangle$ values considered in this search. For those candidates $\langle 2\mathcal{F} \rangle = 4.773$. The expected $2\mathcal{F}_{\text{coh, exp}}$ value for the coherent follow-up search for such candidates is $2\mathcal{F}_{\text{coh, exp}} = 105.83$. Now, 1000 different realizations of pure Gaussian noise
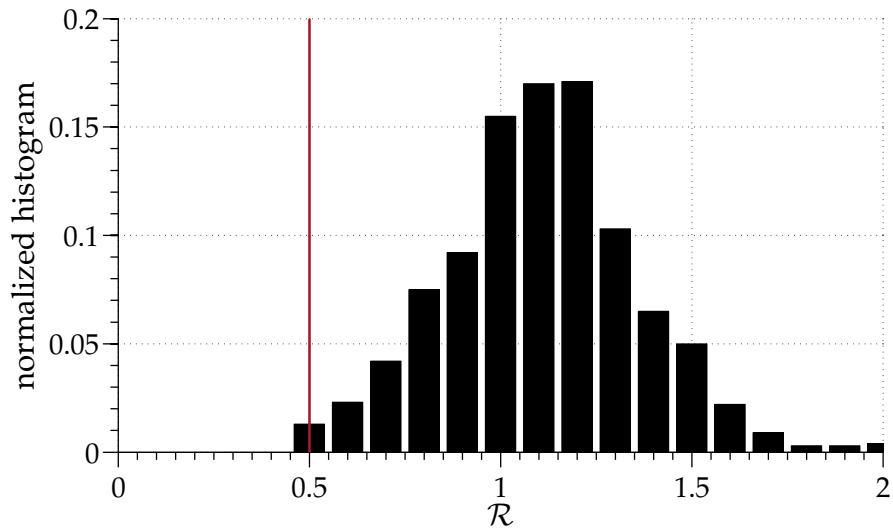
Figure 6.6.5: The plot shows the distribution of $\mathcal{R}$ for 1000 different realizations of Gaussian noise with injected signals having parameters randomly distributed within the search parameter space are created and each in turn analyzed. The strength of the signals varies between 2×10^{-25} and 2.5×10^{-25}. The resulting $\langle 2\mathcal{F} \rangle$ values of the hierarchical search are distributed between 4.35 and 7.30 with a mean value of 5.17. Those values are used to compute the expected value $2\mathcal{F}_{\text{coh, exp}}$ for each candidate. The candidates are then followed-up with the coherent search and the largest $2\mathcal{F}_{\text{coh}}$ value of the searched templates is recovered. The threshold is set to $\mathcal{R}_{\text{thr}} = 0.5$ (red line). Only four of the 1000 signals have $\mathcal{R} < \mathcal{R}_{\text{thr}}$, implying a false dismissal rate of 0.4%.
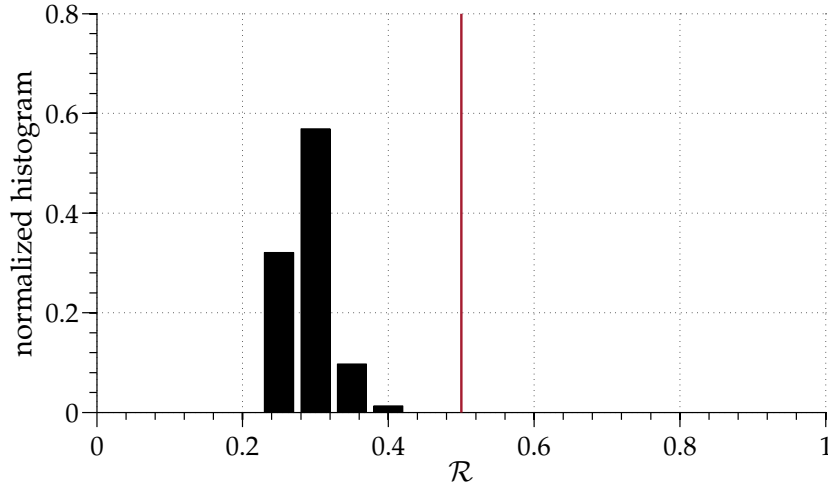
Figure 6.6.6: To estimate the false alarm rate of the coherent follow-up search a Monte-Carlo study over 1000 different realizations of pure Gaussian noise is performed. We assume the candidate to follow-up to have the smallest $\langle 2\mathcal{F} \rangle$ value that this search considers, 4.773. From this the expected $2\mathcal{F}$ value for the follow-up search can be computed. The data sets are searched over with the follow-up search setup and the largest candidates are identified. The distribution of the resulting $\mathcal{R}$ values is shown in this plot. None of the candidates would falsely pass this veto. The resulting false alarm rate is $\leq 0.1\%$.

are created and searched with the coherent follow-up search setup. The loudest candidate is identified and $\mathcal{R}$ is computed. Figure 6.6.6 shows the resulting distribution. The false alarm rate of this veto is $\leq 0.1\%$ which confirms the strength of this follow-up search.

6.6.6 THE RESULTS

The coherent follow-up search is conducted for all 1138 candidates surviving the previous post-processing steps. All but six candidates are discarded. The properties of these candidates are shown in Table 6.6.1. These six candidates can be ascribed to a PSR3 that was made during the fifth Science Run (see Section 6.7). No gravitational wave signal is found in the data set for the searched population of signals.

f [Hz]	α [RAD]	δ [RAD]	$\dot{f}$ [10^{-9} Hz/s]	$2\mathcal{F}_{\mathrm{coh}}$
108.87502619	4.6496	-0.5061	-2.304388655401	178.71
108.87601115	4.6502	-0.5066	-2.422130463848	182.62
108.87627424	4.6502	-0.5066	-2.451940128168	299.83
108.87432273	4.6500	-0.5060	-2.233178423458	172.26
108.87487243	4.6496	-0.5065	-2.287273177437	185.74
108.87451753	4.6498	-0.5065	-2.244262149283	198.42

Table 6.6.1: The table shows the parameters of six candidates that pass the coherent follow-up search. All candidates are located at similar frequency and spindown values. It turns out that these candidates can be ascribed to hardware injection PSR3, as will be shown in Section 6.7.

Certainly, more than these six candidates have to be ascribed to PSR3. In fact, 1079 candidates lie within the immediate neighborhood of the hardware injection in frequency and spindown. The other 59 candidates are independent on PSR3. Figure 6.6.7 shows the computed $\mathcal{R}$ values of these candidates. Some of them have a value of $\mathcal{R}$ quite close to $\mathcal{R}_{\mathrm{thr}} = 0.5$, however, the very low false dismissal rate of this veto gives a good case to rule out these candidates as gravitational wave signals.

6.7   HARDWARE INJECTIONS DURING SCIENCE RUN S5

Over the course of the fifth Science Run ten different gravitational wave signals have been simulated in the data set by adding signals to the interferometer length sensing and control system that cause mirror motions equal to the motions expected by a continuous gravitational wave passing by the interferometer. The parameters of the various hardware injections are randomly distributed within the parameter space that can be searched analyzing data from the LIGO detectors. Hardware injections provide a test set of fake signals and are especially useful for the testing of all-sky searches. Targeted searches can only benefit from them if the injected signals incidentally have parameters within the search parameter space such that it is recovered by the analysis.
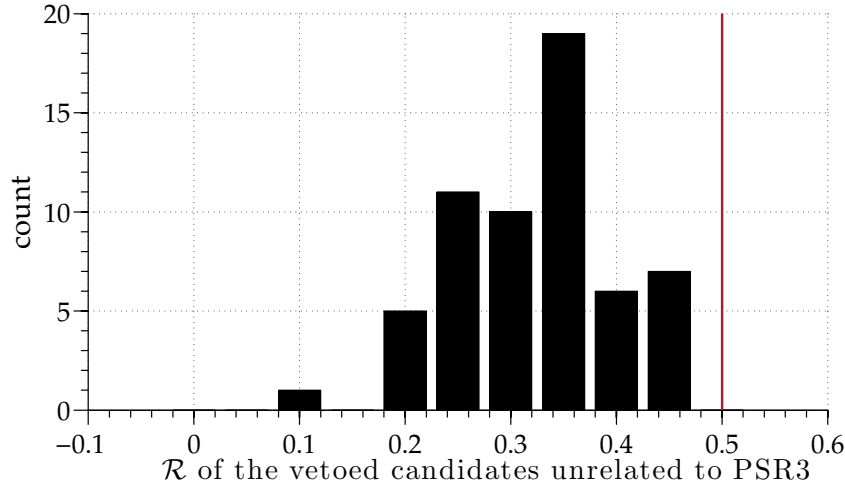
Figure 6.6.7: The distribution of the $\mathcal{R}$ values of the candidates which can not be ascribed to PSR3 and don't pass the coherent follow-up search.

6.7.1   THE PULSAR HARDWARE INJECTION PSR3

Even though five of the ten hardware injections simulate pulsars that have frequency and spindown parameters within the parameter space covered by this search, most of them have sky locations far away from the Galactic Center. However, one of the hardware injections (PSR3) mimics a pulsar that is close enough in sky position and loud enough such that this search recovers it from the noise. The exact properties of PSR3 are shown in Table 6.7.1.

The distance between the sky coordinates of PSR3 and the sky template used in this search is ~ 1.537 rad in right ascension and ~ 0.077 rad in declination, which is larger than the sky region that this search covers. However, the injected signal is very strong (the plus- and cross-polarizations translate into an implied strength of $h_0 \sim 1.63 \times 10^{-23}$) which is why various of the searched templates show an increased $\langle 2\mathcal{F} \rangle$ value.

Figure 6.7.1 shows the resulting $\langle 2\mathcal{F} \rangle$ values of the initial analysis in a frequency band 108.81 Hz $\leq f \leq 108.88$ Hz and in a spindown band -3×10^{-9} Hz/s $\leq \dot{f} \leq 10^{-9}$ Hz/s. The $\langle 2\mathcal{F} \rangle$ values of the templates are color-coded. The highest $\langle 2\mathcal{F} \rangle$ value within the whole structure that is measured is 11.47, which is signif-

VALUE	PROPERTY
751680013	Pulsar reference time t_{ref} in SSB frame $[\mathrm{GPS\ sec}]$
3.2766×10^{-20}	Plus-polarization signal amplitude
-5.2520×10^{-21}	Cross-polarization signal amplitude
0.444280306	Polarization angle ψ
5.53	Phase at reference time t_{ref}
108.8571594	Gravitational wave frequency at t_{ref} $[\mathrm{Hz}]$
-0.583578803	Declination $[\mathrm{rad}]$
3.113188712	Right ascension $[\mathrm{rad}]$
-1.46×10^{-17}	First spindown parameter $[\mathrm{Hz/s}]$
0.0	Second spindown parameter $[\mathrm{Hz/s}^2]$
0.0	Third spindown parameter $[\mathrm{Hz/s}^3]$

Table 6.7.1: The parameters of the hardware injection PSR3.

icantly lower than the expected $\langle 2\mathcal{F} \rangle$ value (of about $\gtrsim 2000$ in case of a perfect signal-template-match) due to the fact that the searched parameter space does not include the signal's parameters. However, since the signal is so loud, even a small waveform match produces a significant candidate. The structure extends over many bins in frequency and spindown and does not show the typical structure and shape of a gravitational wave signal that matches the searched parameter space (compare, for example, with Figure 6.2.1). The frequency and spindown parameters of PSR3 are denoted by the little yellow star.

To prove that the surviving candidates can be ascribed to hardware injection PSR3 we create a data set containing a software generated signal with the parameters of PSR3 on fake Gaussian noise at the level of the actual data. A major complication is that the hardware injections were not turned on over the full time of S5. Instead they were turned on and off multiple times, different between the two detectors. The epoch in which PSR3 was present starts for Hanford on April 18, 2006, at 16:23:06 UTC and ends on October 01, 2007, at 19:15:31 UTC. This spans a time of 531.1 days. During that time the injection was turned on for 265.7 days, hence, reaching a duty cycle for H1 of $\sim 50\%$. In Livingston this epoch was from April 18, 2006, at 16:38:28 UTC to October 01, 2007, at 19:18:40 UTC with a coverage of 290.7 days, which corresponds to a duty cycle for L1 of $\sim 55\%$. Out
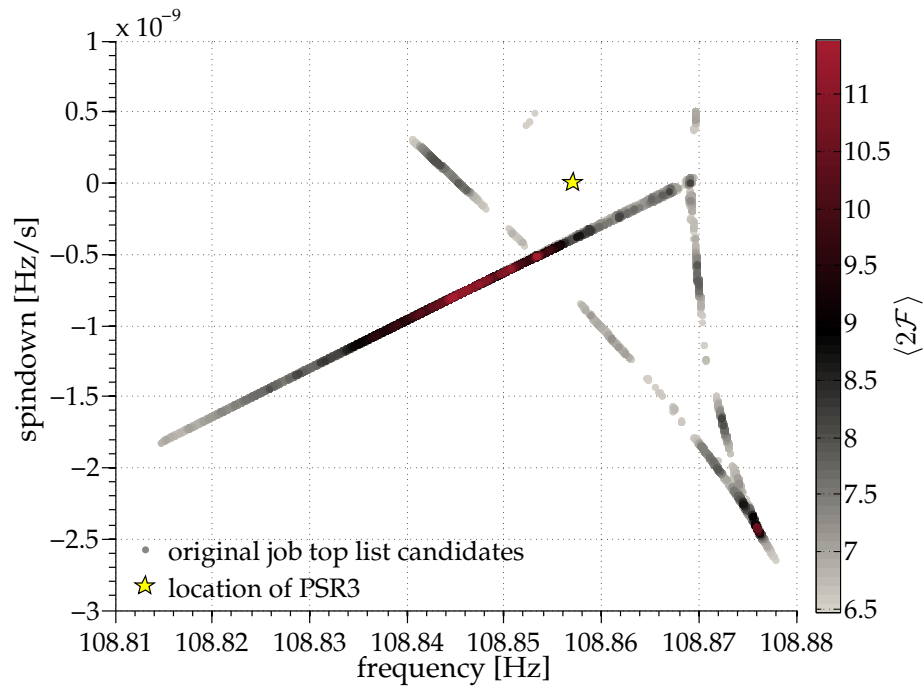
Figure 6.7.1: This plot shows the initial search results in the frequency and spindown regions surrounding hardware injection PSR3. Each color-coded data point represents a candidate that was significant enough to be reported back by the original analysis and, hence, is part of the top list. PSR3 appears as a largely extended structure with high $\langle 2\mathcal{F} \rangle$ values. The maximum $\langle 2\mathcal{F} \rangle$ value reaches 11.47, which is ~ 180 standard deviations above the expectation value of the loudest candidate in Gaussian noise. The shape and structure is not comparable to the structure we expect from gravitational wave signals within the search parameter space. The yellow star denotes the location of PSR3. None of the candidates stored in the top list is located in the immediate neighborhood of that position.

of the 11883 H1 SFTs used in the search the injection was turned on for more than 50% of the time in 4908 SFTs. Out of the 9580 L1 SFTs used in this search the injection was turned on for more than half of the time in 4355 SFTs.

To simulate the injection a data set needs to be created that folds in the information about the on- and off-times of PSR3. The created data set contains a software injection like PSR3 only in those SFTs when the original hardware injection was turned on for more than half of the time. For the reasons explained above, this is not an exact simulation of the data, but it approximates the behavior of the hardware injection in an adequate way. Figure 6.7.2 shows the resulting $\langle 2\mathcal{F} \rangle$ values of the analysis of that data set, zoomed in with respect to Figure 6.7.1 to the location of the six surviving candidates, which are denoted by the little yellow stars. The black circles show the position of the original top list candidates within the frequency range of interest (those candidates are the same as the ones plotted in Figure 6.7.1). On top of that the candidates resulting from the analysis of the simulation are plotted with their $\langle 2\mathcal{F} \rangle$ values being color-coded. The position of the original candidates agrees very well with that of the candidates obtained by the simulation. The six surviving candidates are mostly located at regions of local increase in significance. This test shows clearly that the six candidates can be ascribed to PSR3.

6.8   SUMMARY OF THE POST-PROCESSING

The development of the vetoes presented in this chapter has allowed to probe the existence of a gravitational wave candidate in the data set down to three standard deviations below the expectation for Gaussian noise.

The analysis covers a total of $\sim 4.4 \times 10^{12}$ templates which are split into 10678 single jobs. The highest 10^5 candidates of each job are reported back. These $\sim 10^9$ candidates are investigated in an elaborate post-processing. In order to handle such a large number of candidates, automatisms have to be developed and implemented. The goal of these is to effectively reduce the number of candidates, while, at the same time, ensure that no real gravitational wave signal is dismissed accidentally. False dismissal studies are performed to test each single step of the pipeline and to
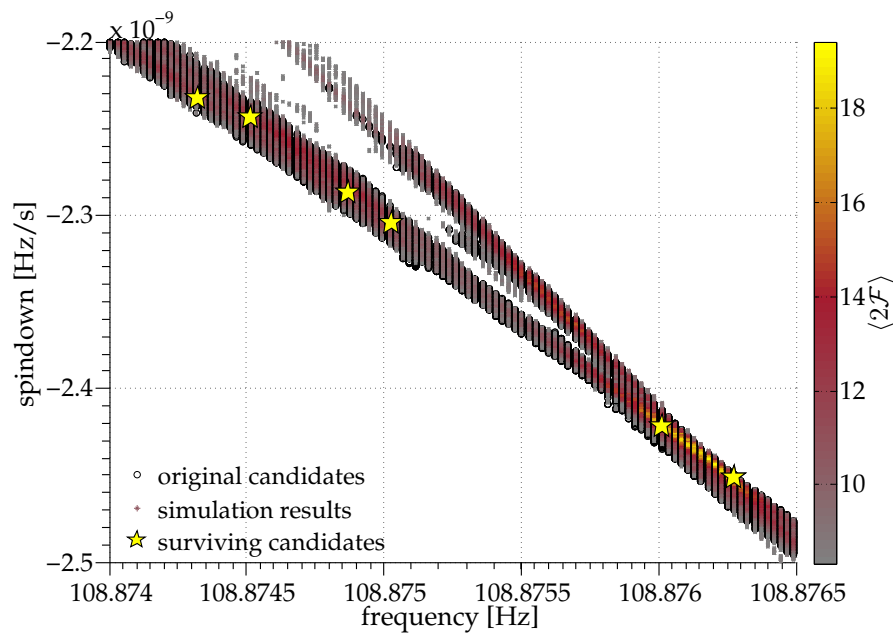
Figure 6.7.2: Results of the simulation of PSR3. PSR3 is simulated by injecting a signal into a pure Gaussian noise data set that matches the data set used for the initial analysis. The signal is injected into all SFTs in which the original hardware injection PSR3 was turned on for more than 50% of the time. The data set is analyzed using the setup of the initial search and the resulting top list of candidates is stored. The frequency and spindown parameters of the reported candidates (color-coded) agree well with the candidates ascribed to PSR3 (black circles). The six candidates (little yellow stars) that survive all post-processing steps are right within the structure that is obtained by the simulation and can therefore be ascribed to PSR3.

guarantee the safety of the different vetoes.

An overview of the different post-processing steps and their impact on the number of surviving candidates is given in Table 6.8.1. At first, the list is cleaned from known detector artifacts. Then, candidates that can be ascribed to the same signal are combined and only a single representative candidate is kept. From the remaining candidates those which show up more significantly in the data of one of the two detectors rather than in the combined data set of the two detectors can be ruled out as real gravitational wave signals. In a similar way, candidates that display an accumulation of significance in a very short time rather than a constant rate of accumulation over the entire observing time are removed from the list of possible gravitational wave signals. A coherent follow-up search with a fine template grid around each candidate and over a time span of 90 days permits the investigation of low-significance candidates. The only six candidates that pass all vetoes can be ascribed to a hardware injection performed during S5.

Figure 6.8.1 shows the distributions of the $\langle 2\mathcal{F} \rangle$ values of the surviving candidates after each of the post-processing steps (note the different scale of the axes in the first sub-figure). The black solid line in all of the plots denotes the significance threshold at 4.773. The upmost plot shows the 10^9 candidates that are reported back from the search. The distribution shows a long tail to the right with extremely large $\langle 2\mathcal{F} \rangle$ values. All candidates with $\langle 2\mathcal{F} \rangle \gtrsim 12.6$ are ascribed to known detector artifacts which is clearly visible by comparison with the second plot that shows the candidates after the known lines cleaning. The clustering changes the shape of the distribution as one would expect it by a uniform reduction of candidates at all $\langle 2\mathcal{F} \rangle$ values. It does not change the specifics of the distribution. The $\mathcal{F}$-statistic consistency veto reduces very efficiently high outliers and lowers the right tail. At this point the candidates with values smaller than the significance threshold are not further considered. Since we can't make any statements about them we do not consider them as being ruled out as gravitational wave signals. They are thus shown in the last sub-figure as the shaded gray area. The effect of the segment resolution veto surprises at first, because it seems to divide the surviving candidates into three sub-groups. This becomes clear when looking at the details of the surviving candidates: all candidates with $\langle 2\mathcal{F} \rangle \geq 6$ can be ascribed to PSR3. That means, the last plot shows the PSR3 candidates and a remaining group of 59 candidates that

POST-PROCESSING STEP	NUMBER OF SUR-VIVING CANDIDATES	TOTAL [%]	RELATIVE [%]
Analyzed number of templates	4 355 231 668 681	–	–
Reported candidates	1 067 800 000	100	100
Known lines cleaning	889 650 421	83	83
Clustering	296 815 037	28	33
$\mathcal{F}$-statistic consistency veto	261 655 549	25	88
Significance threshold	27607	$\mathcal{O}(10^{-3})$	0.01
Segment resolution veto	1138	$\mathcal{O}(10^{-4})$	4
Coherent follow-up search	6	$\mathcal{O}(10^{-5})$	0.5

Table 6.8.1: The different steps of the post-processing and the impact on the surviving number of candidates. The first column gives the post-processing step that has been applied. After applying that step the number of surviving candidates is that of the second column. The third column gives the percentage of the surviving candidates with respect to 1 067 800 000, the number of candidates to start with. The fourth column gives the percentage of surviving candidates with respect to the number that was available before applying each veto.

is close to the expectation value for pure Gaussian noise. These candidates were then ruled out by the coherent follow-up search.

After all, none of the candidates could be uncovered as a gravitational wave signal.

The existence of a hardware injection fairly close to the covered parameter space is a coincidence. Its recovery – although its parameters are not covered by the search – confirm that gravitational wave signals with comparable properties would be detected by this search. The only six candidates that pass the complete post-processing can be ascribed to this hardware injection.

The developed tools are effective and efficiently implemented. They may thus be used in future work of comparable gravitational wave analyses. The final step that remains for this search is to set upper limits on the gravitational wave strain amplitude for signals from the Galactic Center.
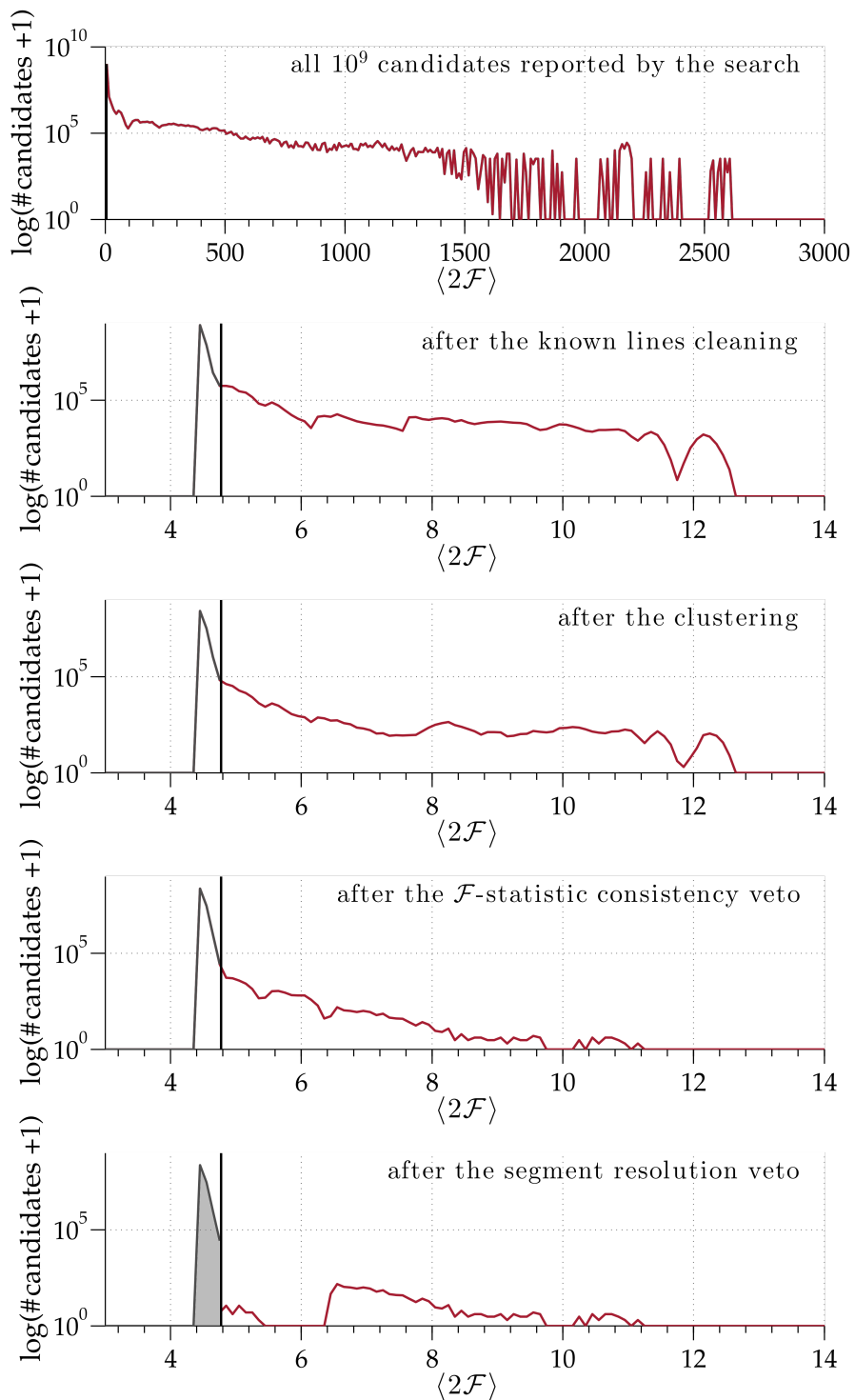
Figure 6.8.1: The distributions of the $\langle 2\mathcal{F} \rangle$ values of the surviving candidates after each of the major steps in the post-processing pipeline. For further explanation see the text.

Our imagination is the only limit to what we can hope to have in the future.

Charles Kettering

7

Upper Limits

This search did not detect any gravitational wave signal. Hence, 90% confidence upper limits are placed on the amplitude of the gravitational waves with parameters covered by the search. In the following we describe how, in order to place upper limits, the parameter space is divided into smaller subsets. Then the method that is used to derive the upper limits is presented and validated. Finally, the upper limits on the targeted signal population are presented.

7.1 THE CONSTANT-η SETS

The entire search frequency band is divided into smaller *sets* and a separate upper limit value is assigned to each of these. The partitioning of the parameter space can be done in different ways, each of which has different advantages and disadvantages. Past searches have often divided the parameter space into equally sized frequency bands. For example, the Einstein@Home all-sky searches have divided the frequency band into 0.5 Hz-wide sub-bands. For a search like this, where the

spindown range grows with frequency, such an approach would lead to significantly larger portions of parameter space for sub-bands at higher frequencies. A slightly different approach is followed for this search, dividing the parameter space into sets containing an approximately constant number of templates. The main advantage of this approach is the approximately constant false alarm rate over all sets. The total number of templates N is divided into 3000 sets of $\sim \eta$ templates. This results in sets small enough that the noise spectrum of the detectors is about constant over the frequency band of each set. From Equation 5.12 we have:

$$\eta = \eta_f \times \eta_{\dot{f}} \times \eta_{\text{sky}} = \frac{\Delta f}{\delta f} \times \frac{\Delta \dot{f}}{\delta \dot{f}} \times 1 = \frac{f_{\text{max}}^2 - f_{\text{max}} f_{\text{min}}}{(200 \text{ yr}) \, \delta f \, \delta \dot{f}}. \qquad (7.1)$$

Hence, for a given minimum frequency f_{min} the maximum frequency f_{max} associated with a set is:

$$f_{\text{max}} = \frac{f_{\text{min}}}{2} + \sqrt{\left(\frac{-f_{\text{min}}}{2}\right)^2 + \eta \, (200 \text{ yr}) \, \delta f \, \delta \dot{f}}. \qquad (7.2)$$

The total number of templates $N = 4\,355\,231\,668\,681$ is this way sorted into the 3000 sets, each containing $\eta = 1\,451\,743\,890$ templates[1].

Valid Sets

Because of known detector artifacts in the data (see Section 6.1), not each of these sets is assigned an upper limit value. Some sets entirely comprise frequency bands excluded from the post-processing by the known lines cleaning procedure. For those bands it is impossible to judge whether an increased $\langle 2\mathcal{F} \rangle$ value is the result of a disturbance or a gravitational wave signal. Therefore, no statement about the existence of a gravitational wave signal in such sets can be made and, hence, no upper limit value can be assigned to those sets. Other sets are only partially affected by the known artifacts and an upper limit value can still be assigned on the *valid* part of the parameter space. That is, upper limit values are computed only for the parameter sub-space of the set that passes the known lines cleaning proce-

---

[1]The last set has ~ 1000 templates less, but that is negligible.

dure. However, in order to keep the parameter space volume associated with each set about constant, upper limit values are assigned only on sets with as few *invalid* parameter space templates as possible.

Figure 7.1.1 gives an overview of the invalid parameter space per set. Each black data point denotes the amount of invalid parameter space for one set. The additional red lines show the known spectral artifacts of the detector. The 60 Hz power lines are clearly visible, as well as, for example, the calibration line at 393.1 Hz (compare Tables A.6.1 and A.6.2). The effect of the presence of the 1 Hz harmonics is visible throughout the whole frequency range.

An upper limit value is assigned to all sets for which the maximum amount of invalid parameter space is lower than a given threshold which yet needs to be defined. Figure 7.1.2 shows the cumulative distribution of the invalid parameter space of the 3000 sets. The distribution has a steep slope (about 115 segments are lost for every 1% reduction in the allowed invalid parameter space portion) up to the 13% value. After reaching the 13% value the slope becomes a lot shallower: less than 6 segments are lost for every 1% reduction in the allowed invalid parameter space portion. The shape of the distribution clearly suggests to pick the threshold at 13% thereby which we keep the maximum number of segments while minimizing the invalid parameter space that we accept per segment. As a result, an upper limit value is placed only on sets comprising at least 87% of valid parameter Space, i.e. 2549 sets ($\sim 85\%$ out of the original sets).

7.2   THE METHOD

The standard frequentist upper limit procedure (as it can be found in various searches, from [21] to [3]) consists of injecting a certain number ($\mathcal{O}(100)$) of signals into the original data set used for the search. The injected signals have parameters (frequency f, spindown $\dot{f}$, right ascension α, declination δ, inclination angle $\cos\iota$, initial phase ϕ_0 and polarization ψ) randomly distributed within the searched parameter space. All signals are injected with the same strength h_0. A small region around the injections in frequency and spindown (and for the all-sky searches also in sky) is then analyzed and the loudest candidate is identified. This
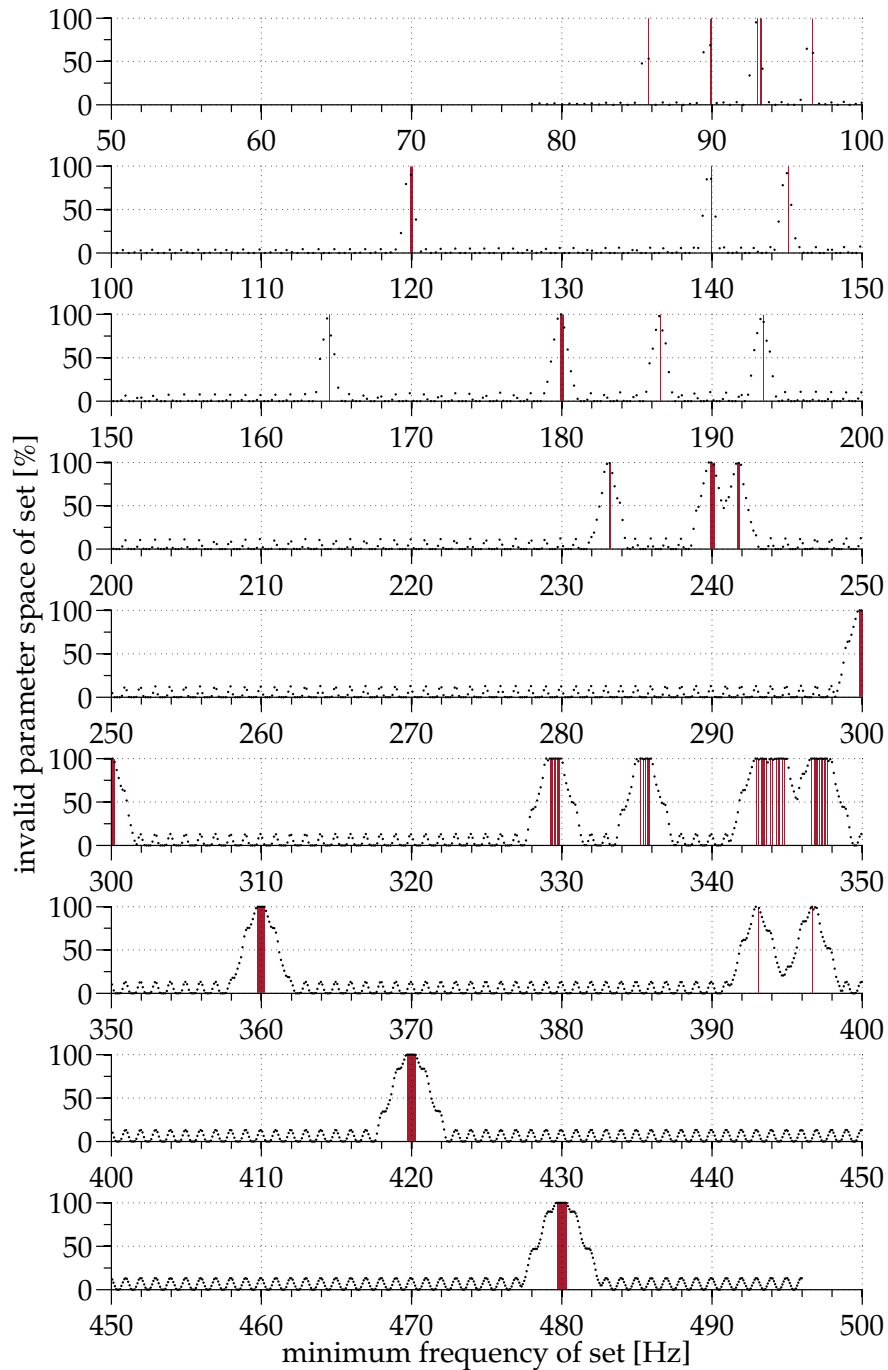
Figure 7.1.1: The plot shows the amount of invalid parameter space per set over frequency. Red lines denote the frequency bands that include known detector artifacts. The periodical variations show the effect of the 1% harmonics. They are modulated on top of the stronger lines, like the calibration line at 393.1 Hz or the 60 Hz power lines.
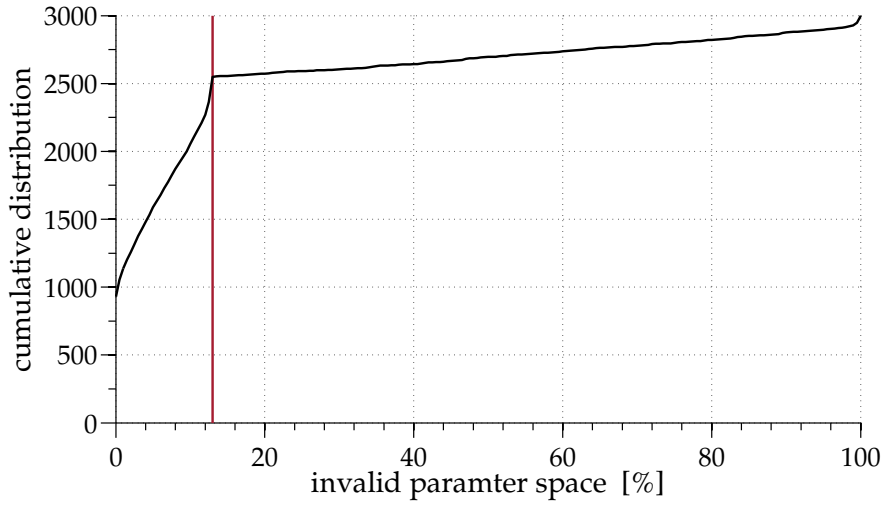
Figure 7.1.2: The cumulative distribution of the invalid parameter space per set (black line). The distribution shows a steep increase towards the 13% threshold (red line). After reaching that threshold, the distribution has a shallow knee up to the 100% loss. Including sets with higher amount of invalid parameter space has no advantage, but lowering the threshold rapidly decreases the number of sets on which upper limit statements are placed. The characteristic shape of this distribution simplifies the choice of the threshold.

candidate then undergoes the complete post-processing pipeline. If it survives all vetoes, and if its $\langle 2\mathcal{F} \rangle$ value exceeds the $\langle 2\mathcal{F} \rangle$ of the most significant surviving candidate from the search in that set, then such injection is counted as *recovered*. The fraction of all recovered injections gives the *confidence* value $c(h_0)$. The h_0 value that leads to a 90% confidence value is $h_0^{90\%}$. If a signal of that strength had been present in the data, in 90% of the possible signal realizations this would have resulted in a more significant loudest candidates than what was measured. Thus, the presence of a signal of strength $h_0^{90\%}$ or louder in the data set is excluded and $h_0^{90\%}$ is the 90% confidence upper limit value on the gravitational wave amplitude for the set.

The $h_0^{90\%}$ value is unknown and differs across the different sets because of the varying sensitivity of the instrument with frequency. Therefore, in general several 100 injection trials at different h_0 values have to be carried out to bracket the 90% confidence. Then an interpolation can be utilized to estimate the $h_0^{90\%}$. This standard approach is extremely time consuming. In the following, a less demanding

approach is presented.

ANALYTIC UPPER LIMITS

After conducting the standard upper limit approach for some sample sets it turns out that in 98.1% of all cases in which a candidate is not recovered, it is because the candidate fails the comparison with the loudest surviving candidate from the search in that set. In 0.2% of the cases it is the single-interferometer consistency veto that discards the candidate and in 1.7% the candidate it is lost at the segment resolution veto step. These numbers mirror the very low false dismissal rates that were obtained for the vetoes at the $h_0^{90\%}$ level. It is computationally infeasible to perform a coherent follow-up search as part of the upper limit studies. However, the very low false dismissal rate of the follow-up veto (0.04%) implies that the impact on the upper limit values is negligible. The fact that only the strength of an injection and the comparison to a given threshold determines the final upper limit allows for another, computationally much less intense approach.

The basic idea is that it is not necessary to sample the different h_0 values with different realizations of the noise and nuisance parameters. Instead, the same noise and signal realizations can be re-used for different h_0 values to sample at virtually no cost the confidence versus h_0 value and find the desired $h_0^{90\%}$ value.

The relation between the measured $\langle 2\mathcal{F} \rangle$ value and the injection strength h_0 can to good approximation be described by the following relation:

$$\langle 2\mathcal{F} \rangle \simeq \mathcal{N} + \langle \mathcal{G} \rangle h_0^2, \tag{7.3}$$

where $\mathcal{N}$ represents the contribution of the noise and $\langle \mathcal{G} \rangle$ is a constant, averaged over the 630 segments, that depends on the signal parameters and on the time-stamps of the data. It is possible to obtain $\mathcal{N}$ and $\langle \mathcal{G} \rangle$ by injecting two signals with a different h_0 value, keeping *all* other parameters fixed. With this information it is possible to estimate $\langle 2\mathcal{F} \rangle$ for any value of h_0 for a particular combination of signal and nuisance parameters and for a given data set. With two sets of 100 injections and searches we produce 100 $\{\mathcal{N}, \langle \mathcal{G} \rangle\}$ couples. Fixing the value h_0 and using the $\{\mathcal{N}, \langle \mathcal{G} \rangle\}$ we obtain a collection of $\langle 2\mathcal{F} \rangle$ values and the confidence is immediately estimated by counting how many of these exceed the loudest measured one.

The $h_0^{90\%}$ value can be derived analytically, without the need of injecting further signals.

The analytic upper limit procedure requires only two cycles through the injection-analysis-procedure for each set. Having 2549 sets and 100 trials each, this gives 509 800 injections that need to be processed. Since some sets, at low and high frequencies are especially noisy, more than 100 injections are performed for those sets. A total of 796 400 injections were processed. Assuming ~ 3000 jobs running in parallel on the ATLAS compute cluster, the whole procedure takes about a week. This is significantly less than the time needed by the standard approach. The parameter ranges within which the parameters of the injected signals are distributed are shown in Table 7.2.1.

To estimate the uncertainty on the upper limit values we use a linear approximation to the curve $c(h_0)$ in the neighborhood of $h_0^{90\%}$. Figure 7.2.1 shows $c(h_0)$ in that region for a set at about 150 Hz. The 1σ uncertainty in $c(h_0)$ is given by the standard expression for the standard deviation of a binomial variable:

$$\sigma = \sqrt{N_{\text{trials}}\, p(p-1)} = \sqrt{100 \times 0.9 \times 0.1} = 3. \tag{7.4}$$

with $p = 0.9$ (since we are close to 90% confidence) and $N_{\text{trials}} = 100$. A 3% error on the confidence corresponds to an uncertainty of $\lesssim 5\%$ on $h_0^{90\%}$, as is illustrated in Figure 7.2.1.

The results obtained by the analytic upper limit procedure are verified on a sam-

PARAMETER	RANGE
Signal strength	$h_0 = \{5, 7\} \times 10^{-25}$
Sky position [rad]	$\sqrt{\alpha^2 + \delta^2} \leq 2 \times 10^{-4}$ rad from Galactic Center
Frequency [Hz]	within set frequency band
Spindown [Hz/s]	$0 \leq \dot{f} \leq (-f_{\text{max}}^{\text{set}}/200\,\text{yr})$, for the $f_{\text{max}}^{\text{set}}$ of the set
Polarization angle	$0 \leq \psi \leq 2\pi$
Initial phase constant	$0 \leq \phi_0 \leq 2\pi$
Inclination angle	$-1 \leq \cos \iota \leq 1$

Table 7.2.1: The parameters of the signal population of the upper limit study.
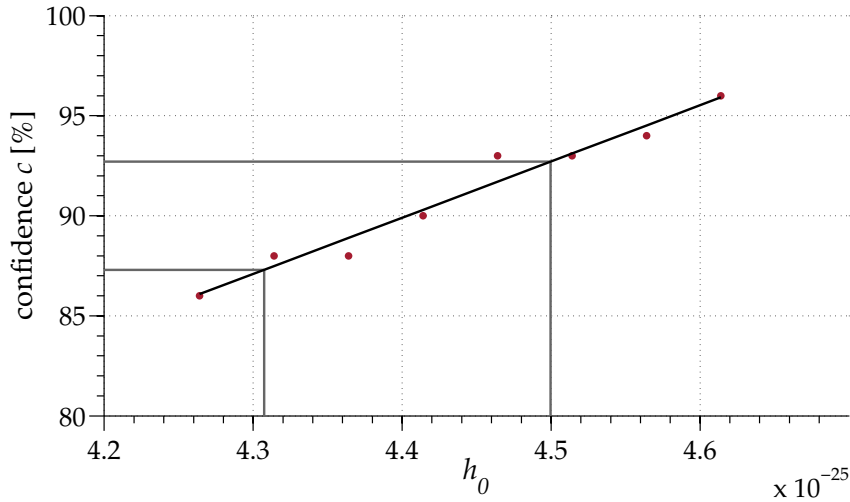
Figure 7.2.1: The plot shows the resulting confidence values for different h_0 values for one example set. By fitting a straight line to the data points in a small enough region around the 90% confidence value the 3% error on the confidence can be translated into an uncertainty of $\lesssim 5\%$ on $h_0^{90\%}$.

ple base by injecting signals corresponding to the signal population described in Table 7.2.1 at a strength of $h_0^{90\%}$ into the search data set and computing the corresponding confidence values using the standard frequentist procedure. Table 7.2.2 shows the results for 10 different, randomly chosen sets. In all but two cases the measured confidence lies within 1σ statistical uncertainty value based on 100 trials. In the other two sets the confidence is larger than 90% plus one standard deviation, hence, the computed upper limits are conservative.

7.3   RESULTS

The analytic upper limits procedure described above results in the upper limits presented in Figure 7.3.1. The tightest upper limit is $\sim 3.34 \times 10^{-25}$ at $\sim 149\,\mathrm{Hz}$, in the most sensitive spectral region of the LIGO detectors. The large values of the upper limit values close to $350\,\mathrm{Hz}$ are due to spectral residuals of the detectors' violin modes. In ten sets within this region, the data is so disturbed that no upper limits can be placed. Therefore, upper limit values are reported for 2539 sets.

SET ID	$f_{\text{MIN}}^{\text{SET}}$ [Hz]	$h_0^{90\%}$	THRESHOLD	$c(h_0^{90\%})$ [%]
57	103.12	5.85×10^{-25}	4.75292	93
254	162.42	3.67×10^{-25}	4.709811	92
363	187.34	3.80×10^{-25}	4.70976	88
631	237.77	4.50×10^{-25}	4.739409	92
1025	296.74	5.52×10^{-25}	4.749726	90
1586	364.61	7.13×10^{-25}	4.744572	90
1672	373.93	6.75×10^{-25}	4.698406	90
2302	436.16	7.77×10^{-25}	4.721777	93
2695	470.83	8.49×10^{-25}	4.730347	94
2972	493.81	1.18×10^{-24}	4.71697	100

Table 7.2.2: Validation of the $h_0^{90\%}$ value for ten sample sets. For each of the sets 100 gravitational wave signals have been injected at the $h_0^{90\%}$ level into the search data set. The confidence is the fraction of these injections that was recovered with a higher $\langle 2\mathcal{F} \rangle$ value than that of the loudest surviving candidate of that set.
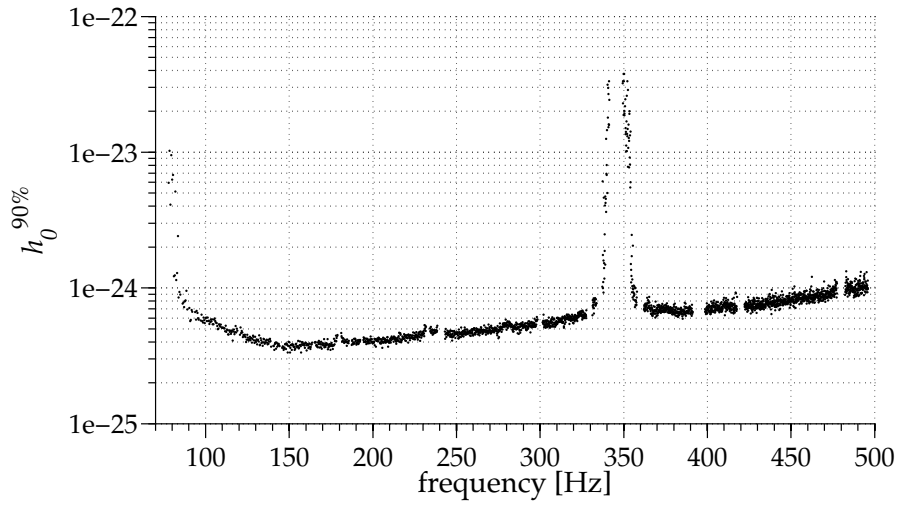
Figure 7.3.1: This plot shows the 90% confidence upper limits on the intrinsic gravitational wave strain h_0 from a population of signals with parameters within the search space. The tightest upper limit is $\sim 3.34 \times 10^{25}$ at ~ 149 Hz. The large values of the upper limit values close to 350 Hz are due to spectral residuals of the detectors' violin modes.

8

Second Order Spindown

At the time the search was set up, no hierarchical analysis code was available that could perform a search over second order spindown values. The implementation of such a function is non-trivial and has only very recently been added to the analysis program. All results presented in this work relate to a population of signals that does not include a second order spindown. This is reasonable within each coherent search segment: the largest second order spindown that over a time T_{seg} produces a frequency shift, $\ddot{f}T_{\text{seg}}^2$, that is less than one half of a frequency bin is:

$$\ddot{f}T_{\text{seg}}^2 \leq \frac{1}{2T_{\text{seg}}}.\qquad(8.1)$$

Inserting the segment length used for this search, $T_{\text{seg}} = 11.5$ h, the maximum second order spindown that satisfies Equation 8.1 is $\ddot{f} \sim 7 \times 10^{-15}$ Hz/s^2. Using the standard expression for the second order spindown,

$$\ddot{f} = n\frac{\dot{f}^2}{f},\qquad(8.2)$$

and substituting $|\dot{f}/f| = 1/200$ yr, a braking index $n = 5$, and $\dot{f} = -7.86 \times 10^{-8}$ Hz/s (the largest spindown covered by the search), implies that the highest $\ddot{f}$ that should have been considered is $\ddot{f} \sim 6 \times 10^{-17}$ Hz/s^2. We conclude that for the coherent searches over 11.5 hours not including the second order spindown does not preclude the detection of systems in the covered search space with second order spindown values of the order $\sim 6 \times 10^{-17}$ Hz/s^2.

Due to the long observation time T_{obs} (almost two years), the second order spindown should, however, not be neglected in the incoherent combination. The minimum second order spindown signal that is necessary to move the signal by a frequency bin δf within the observation time is:

$$\ddot{f}_{\text{min}} = \frac{\delta f}{T_{\text{obs}}^2} \sim 6 \times 10^{-21} \text{ Hz/s}^2. \qquad (8.3)$$

This means, the presented results are surely valid for all signals with second order spindown values smaller than 6×10^{-21} Hz/s^2.

To quantify more precisely the impact of signals with higher second order spindown values than 6×10^{-21} Hz/s^2 on the results of this search, we compute the confidence at a fixed $h_0^{90\%}$ value for populations of signals with a second order spindown. The results are summarized in Table 8.0.1. It turns out that signals with a second order spindown lower or equal $\ddot{f} \leq 5 \times 10^{-20}$ Hz/s^2 do not impact the results presented in this work. This value is larger than all reliably measured values of known neutron stars as of today, where the maximum value measured is $\ddot{f} \simeq 1.2 \times 10^{-20}$ Hz/s^2 [89], see Figure 8.0.1.

However, the standard class of signals with large spindown values is expected to also have high values of the second order spindown (see Equation 8.2). Not having included a second order spindown parameter in the search means that not a standard class of objects, but rather a population with apparently very low braking indices is targeted. Such anomalous braking indices may appear, for example, for stars with either a growing magnetic surface field, or a growing moment of inertia. Under these circumstances the relationship between observed spindown and ellipticity may break. The ellipticity of the star might be large enough that gravitational waves, even at a distance as far as the Galactic Center, can be measured at a spindown value that would not imply such strong gravitational waves in the

$\ddot{f}\,[\mathrm{Hz/s^2}]$	$c(\ddot{f})\,[\%]$	
6×10^{-21}	93.2	The minimum $\ddot{f}$ to influence incoherent step.
1×10^{-20}	93.5	Typical known $\ddot{f}$ values are below this boundary.
5×10^{-20}	89.3	The maximum $\ddot{f}$ without impact on the results.
1×10^{-19}	85.1	
5×10^{-19}	69.1	
1×10^{-18}	58.2	
5×10^{-18}	25.9	
1×10^{-17}	11.7	
5×10^{-17}	0.2	$\ddot{f}$ corresponding to n of order unity.

Table 8.0.1: The degradation in confidence for a signal population with randomly distributed parameters within the search space and an additional, varying second order spindown. The injections are performed at $h_0^{90\%}$. The confidence remains $\sim 90\%$ until the second order spindown takes values of about 5×10^{-20} Hz/s^2. After that it falls rapidly. A signal population that corresponds to the spindown limit with braking indices of order unity would result in a higher upper limit value $h_{0,\ddot{f}}^{90\%}$.

standard picture.

8.1 PROBING THE SEARCH

A population of stars that is represented by Equation 8.2 with standard braking indices (of order unity) is not optimally covered by this search. Without further investigation, no statements about such a population can be made. To remedy this, in the following, the different post-processing stages of this search are applied to a set of test data that includes such a signal population.

A set of 500 signal injections is created with the parameters given in Table 8.1.1 and strengths at the 90% confidence level $h_0^{90\%}$. The second order spindown values of the injections are uniformly distributed within a range limited by the $\ddot{f}$ value of Equation 8.2 with a braking index of $n = 5$.

The data is analyzed using the original template setup of the corresponding job of the search and the highest $\langle 2\mathcal{F}\rangle$ value within a region as large as the cluster size
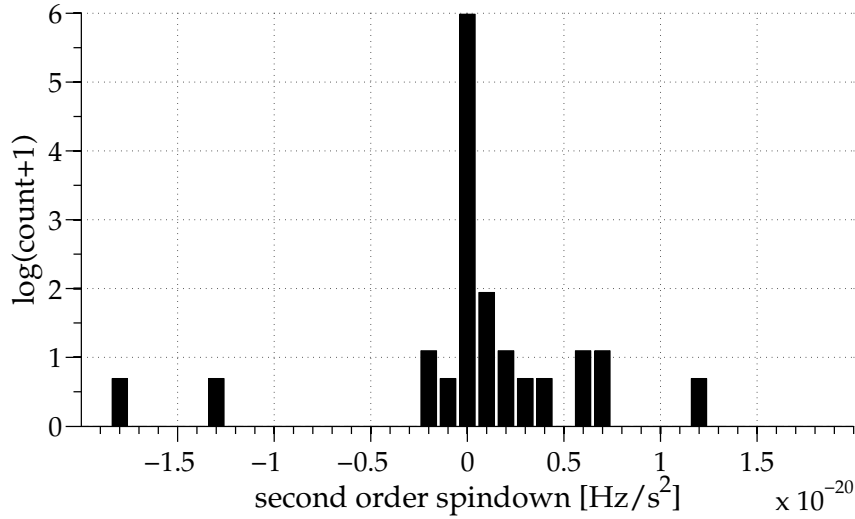
Figure 8.0.1: The histogram shows the distribution of all reliably measured second order spindown signals from the ATNF pulsars [89] as of today. Most values lie in the range -2×10^{-21} Hz/s$^2 \leq \ddot{f} \leq 7 \times 10^{-21}$ Hz/s^2. All second order spindown values are smaller than the maximum second order spindown that does not affect the presented results, 5×10^{-20} Hz/s^2.

around the injection spot is recovered. In 36 cases this region is empty. The reason is that the signals are so weak either that other (noise) templates within the parameter space fill up the according job top list or that due to the second order spindown the signal could not be recovered at the correct frequency and spindown. First, the recovered 464 candidates are tested with the $\mathcal{F}$-statistic consistency veto (Section 6.3). The application of that veto reduces the number of candidates to 458. The resulting false dismissal rate is 1.3%. The next step of the post-processing is the selection of the most significant subset with a significance threshold at 4.773 (Section 6.4). 70.3% of the signals are above this threshold. Then the segment resolution veto (Section 6.5) is applied to the 322 recovered injections that pass the significance threshold. 9 signals are lost, which gives a false dismissal rate of 2.8%. Such false dismissal rates are acceptable.

More problematic is the last veto which is applied as part of the coherent follow-up search. Coherent searches require a better parameter match in order to obtain large resulting significance values. Therefore, we expect a very high false alarm rate for this veto. Obtaining the false dismissal rates for a variety of different second

PARAMETER	RANGE
Signal strength	$h_0^{90\%}$
Sky position [rad]	$\sqrt{\alpha^2 + \delta^2} \leq 10^{-3}$ rad from Galactic Center
Frequency [Hz]	$78\,\text{Hz} \leq f \leq 496\,\text{Hz}$
First order spindown [Hz/s]	$0 \leq \dot{f} \leq (-f_{\text{max}}^{\text{set}}/200\,\text{yr})$, for $f_{\text{max}}^{\text{set}}$ of the set
Second order spindown [Hz/s²]	$0 \leq \ddot{f} \leq \left(n(\dot{f}_{\text{max}}^{\text{set}})^2/f_{\text{min}}^{\text{set}}\right)$
Braking index	$n = 5$
Polarization angle	$0 \leq \psi \leq 2\pi$
Initial phase constant	$0 \leq \phi_0 \leq 2\pi$
Inclination angle	$-1 \leq \cos\iota \leq 1$

Table 8.1.1: Parameters of the false dismissal study test set. 500 signals have been injected into Gaussian noise with parameters within the searched parameter space and an additional second order spindown that fulfills the spindown limit Equation 8.2 for braking indices as high as $n = 5$.

order spindown values is computationally very demanding. Therefore, the study is restricted to a few samples. It turns out that the false dismissal remains very low for second order spindown signals with values lower or equal $5 \times 10^{-20}\,\text{Hz/s}^2$. In a study over 1000 injections no candidate was lost, hence the false dismissal rate is $\leq 0.1\%$. In contrast to that, the false dismissal rate for a signal population with second order spindown values of $4 \times 10^{-17}\,\text{Hz/s}^2 \leq \ddot{f} \leq 5 \times 10^{-17}\,\text{Hz/s}^2$ is about 82%.

8.2 UPPER LIMITS ON A SECOND ORDER SPINDOWN POPULATION

In the post-processing of the search, the application of the $\mathcal{F}$-statistic consistency veto, the selection of the significant subset and the segment resolution veto reduce the number of candidates to 1138. Out of these candidates, 1079 can be ascribed to hardware injection PSR3. 59 candidates remain and cannot safely be ruled out as potential gravitational wave signals with a second order spindown, because the false dismissal rate of the veto applied within the follow-up search is very high for a population of signals with braking indices of order unity. Therefore, no statement about these candidates can be made. Thus, the upper limits for a second order spindown population need to be based including these candidates. The 59 candi-

dates are sorted among 35 sets, hence, about 1.3% of the sets are affected by this. The impact is quite small as these candidates do not have large $\langle 2\mathcal{F} \rangle$ values: Figure 8.2.1 compares the distribution of the loudest survivors of the 35 original sets with that of the 35 sets including the 59 candidates that can't be ruled out as gravitational wave signals. Since all candidates considered in this search (above the significance threshold) are ruled out by the post-processing, the original 35 candidates have values below the significance threshold at 4.773. The new candidates, however, are candidates above that threshold because they belong to the significant subset considered by this search. Interestingly, four of these candidates are above the expectation value for Gaussian noise and three are even three standard deviations above the expectation value. A future follow-up study of these candidates which considers second order spindown values is in the planning stage and provides an exciting project. The final upper limit results for a "standard" signal population with second order spindown values are shown in Figure 8.2.2.
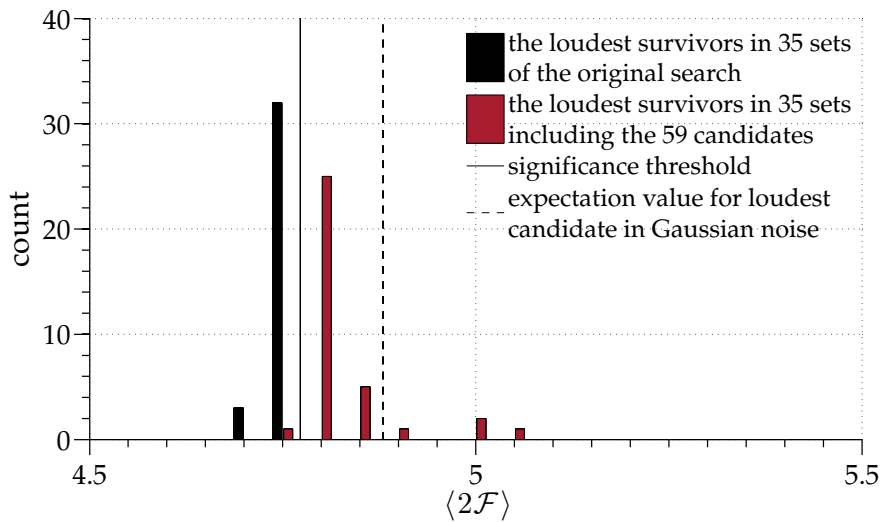
Figure 8.2.1: For a population of signals with second order spindown values of order unity, 59 candidates cannot be ruled out as being gravitational wave signals. These can be sorted into 35 sets and replace the loudest survivors that were used for the comparison within the upper limit procedure in these sets. The black histogram shows the distribution of the $\langle 2\mathcal{F} \rangle$ values of the "original" candidates used for the comparison, and the red histogram that of the "new" ones. The usage of the "new" candidates does not have a large impact on the resulting upper limits. However, four of the values are above the expectation value for Gaussian noise. A future follow-up study on these 59 candidates including second order spindown signal templates provides an interesting project.
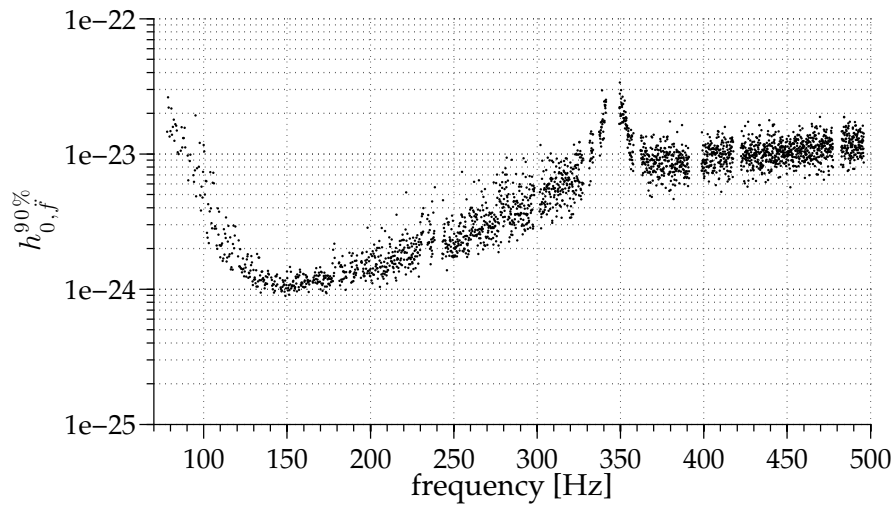
Figure 8.2.2: Upper limits for a population of signals consistent with Equation 8.2 using $n = 5$. The resulting second order spindowns are of the order of a few $\sim 10^{-17}$ Hz/s^2. The upper limits are by a factor of ~ 2 higher than the upper limits presented for the targeted population. In addition, the 59 candidates that can't be ruled out as gravitational wave signals with second order spindown are included in these upper limits, affecting 35 different sets. An additional coherent follow-up search that includes second order spindown is necessary to make statements about such signals.

'Now to sum it up,' said Bernard. 'Now to explain to you the meaning of my life. [...] The illusion is upon me that something adheres for a moment, has roundness, weight, depth, is completed. This, for the moment, seems to be my life.'

Virginia Woolf, *The Waves*

9
Conclusion

Although this is the most sensitive targeted search for continuous gravitational waves to date, no evidence for a gravitational wave signal within 3 pc of Sgr A* was found in the searched data for the targeted population. No other directed search has targeted the Galactic Center before. Therefore, the tightest upper limits came from the all-sky searches. The h_0 upper limit in the frequency range 152.5 - 153.0 Hz from [3] is 7.6×10^{25}. The results presented here tighten this constraint by about a factor of two. This improvement was possible because of the longer data set used and because of the comparatively low number of templates which allowed to investigate candidates with very low $\langle 2\mathcal{F} \rangle$ values. The choice of a hierarchical search technique has also been an advantage: for comparison, the targeted search for a continuous gravitational wave signal from Cas A, which used 12 days of the same data as this search, and analyzed them with a fully coherent method, resulted in a 95% confidence at ~ 150 Hz of 7×10^{25} [7]. The improvement in sensitivity compared to the search of [7] is gained by having used much more data and thanks to the low-threshold post-processing. An additional benefit comes from

the fact that the 630 data segments were chosen based on the coupling between the detector and the source, whereas [7] used a contiguous data set over several days in which such effects average out.

Following [120] and [3], the gravitational wave amplitude upper limits can be expressed as $h_0^{90\%} = H\sqrt{S_h/T_{\text{data}}}$, where S_h is the detector noise and $T_{\text{data}} = N_{\text{seg}}T_{\text{seg}}$. The factor H can be used for a direct comparison of different searches, with low values of H implying, at fixed $\sqrt{S_h/T_{\text{data}}}$, a more effective search [102]. This search has a value of $H \sim 77$, which is an improvement of almost a factor two compared to [3], where H varies within ~ 141 and ~ 150 with about half of the data. This confirms that the improvement in sensitivity for this search with respect to [3] can be ascribed to an overall intrinsically more sensitive technique being employed, for the reasons explained above.

Assuming a value for the moment of inertia, the upper limits on h_0 can be recast as upper limits on the pulsar ellipticity, $\epsilon^{90\%}$ (see Equation 5.5). For standard neutron stars the maximum predicted ellipticity is a few times 10^{-6} [74]. The upper limits on ϵ presented in Figure 9.0.1 are about an order of magnitude higher than this over most of the searched frequency band. Exotic star models do not exclude solid stars which could sustain ellipticites up to a few 10^{-4} [72, 85, 93], well within the range that our search is sensitive to. However, since the predictions refer to the maximum values that model could sustain, our non-detections do not constrain the composition of neutron stars or any fundamental property of quark matter. We have considered a range of variability for the moment of inertia of the star between 1 - 3 I_{fid}: [113] predicts moments of inertia larger than I_{fid} for stars with masses $\geq 1 M_\odot$, which means for all neutron stars for which the masses could be measured. [46] have estimated the moment of inertia for various EOS and predict a maximum of $I = 2.3 \times I_{\text{fid}}$. [80] found the highest moment of inertia to be $I = 3.3 \times I_{\text{fid}}$ for EOS G4 in [81]. Figure 9.0.1 shows these upper limits for values of the moment of inertia between 1 and 3 $I_{\text{fid}} = 10^{38}$ kg m^2. The upper limits for $I = I_{\text{fid}}$ range from $\sim 7.7 \times 10^{-3}$ at 78 Hz to $\sim 2.8 \times 10^{-5}$ at 496 Hz. The most constraining value is $\sim 8.7 \times 10^{-6}$ at ~ 438 Hz for $3 \times I_{\text{fid}}$.

For frequencies in the range 50 - 500 Hz the lower limits on the distance derived in [3] at the spindown limit range between 3.9 and 0.5 kpc, but because of the smaller spindown range the corresponding spindown ellipticities are lower, down
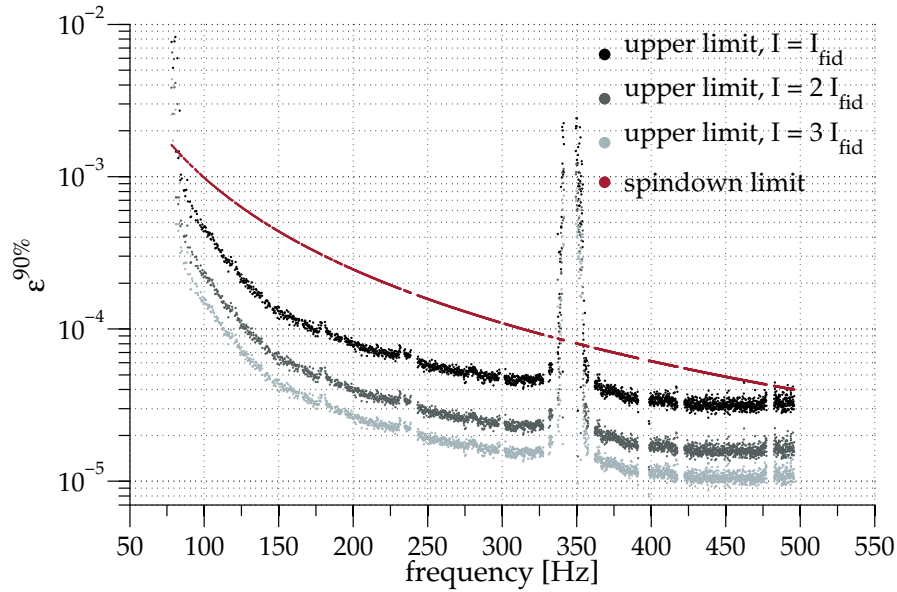
Figure 9.0.1: The plot shows the $h_0^{90\%}$ upper limits on the ellipticity ϵ for our target population of sources, at a distance $r = 8.3$ kpc. The upper curve is the spindown limit ellipticity from Equation 5.2, that is, the maximum ellipticity that a source at that frequency could have. It is the maximum ellipticity for two reasons: it is the *spindown limit* ellipticity that corresponds to the *highest spindown* value searched for at every frequency.

to 7×10^{-6} at 500 Hz, with respect to the ellipticity upper limit values that result from this search. This reflects a different target population: closer by and with lower ellipticities in [3], farther away, at the Galactic Center, and targeting younger stars, in this analysis. We note that the $h_0^{90\%}$ upper limits presented here could also be reinterpreted as limits on different ellipticity-distance values (as done in Figure [13] of [16]) for sources lying along the *direction* to the Galactic Center.

This search did not include second order spindown values. This is reasonable within each coherent search segment, as was shown in Chapter 8. The longest T_{seg} before a second order spindown needs to be considered can be evaluated by requesting a frequency shift due to the second order spindown that is less than one half of a frequency bin. This yields a maximum segment length of 26.8 h. The segment length of this search is well within this limit. However residuals from second order spindowns in this range still affect the detection efficiency of the incoher-

ent combination step. The degradation in detection efficiency is negligible up to second order spindown values of 5×10^{-20} Hz/s^2, which is larger than all reliably measured values of known pulsars as of today. Such a signal population corresponds to the spindown limit with very low braking indices. Current estimates of h_0 upper limits derived for a population of signals with second order frequency spindown corresponding to a braking index of order unity are at 150 Hz about a factor of two higher than those presented for the targeted population. This is an important fact to keep in mind when interpreting or comparing the presented results. Assuming a population of signals with braking indices of order unity, 59 candidates can not be ruled out as gravitational wave candidates, because the false dismissal rate of the coherent follow-up veto is incredibly high. Therefore, a coherent follow-up search that includes a large enough range in second order spindown is in the planning stage and will be performed in the near future. Such a follow-up is promising, but time consuming and exceeds the scope of this work. An additional collaborative search for coincident X-ray signals in RXTE data is planned. The detection of an X-ray signal from the Galactic Center for the parameters of any of the 59 candidates would be intriguing. On the other hand, the absence of such X-ray signals would not allow us to draw conclusion about the existing stars at the Galactic Center or within the line of sight.

The Advanced LIGO and Advanced Virgo detectors are expected to be operational by 2016 and to have reached their final sensitivity by 2019. The new detectors will be an order of magnitude more sensitive than the previous generation. Extrapolating from these results, a similar search on data from advanced detectors should be able to probe ellipticity values of normal neutron stars at the Galactic Center and even lower ellipticity values for closer objects.

A

Appendix

A.1 Computational Cost of the Search

The analysis algorithm used for the search is available in the LALSuite[1] under the name `lalapps_HierarchSearchGCT`. The analysis program reads in the available data (stored as 1800 s-long Short Fourier Transforms SFT) and performs on each single segment a coherent $2\mathcal{F}$-statistic search. The internal structure is as follows: the outmost loop cycles through the coarse grid spindown values. Within this loop is another one over the data segments. This loop, in turn, contains two further, serial loops: one over the frequency bins and one over the fine spindown grid bins. The computational cost of the code, T_{runtime}, can be estimated by a timing procedure which measures the duration of each single loop in an appropriate

---

[1]The LALSuite is a library of gravitational wave data analysis routines written in C following the ISO/IEC 9899:1999 standard (more commonly known as C99) which is available at https://www.lsc-group.phys.uwm.edu/daswg/projects/lalsuite.html.

test setup and can be expressed as:

$$T_{\text{runtime}} = N_{\text{det}} \left(k_1 N_{\text{SFT}} + k_2 \frac{f_{\text{max}}}{\tau \delta \dot{f}} \right.$$
$$\left. \times \; k_3 \; N_{\text{seg}} \left(\frac{k_4 (f_{\text{max}} - f_{\text{min}})}{\delta f} + k_5 \gamma \frac{f_{\text{max}} - f_{\text{min}}}{\delta f} \frac{f_{\text{max}}}{\langle n_{\text{min}} - 1 \rangle \tau \delta \dot{f}} \right) \right) \tag{A.1}$$

$$+ \, k_6, \tag{A.2}$$

where N_{det} is the number of detectors of which the data is analyzed, N_{SFT} is the number of SFT data files, f_{min} and f_{max} are the minimum and maximum frequency searched over, N_{seg} is the number of segments in which the data are divided, δf and $\delta \dot{f}$ are the resolutions in frequency and spindown, respectively, and $\langle n_{\text{min}} - 1 \rangle \tau$ defines the covered spindown range through the braking index n and the spindown age τ. k_1 to k_6 are the six timing constants derived by the timing test runs:

$$k_1 = 6.25 \times 10^{-4}, \quad k_2 = 1.06, \quad k_3 = 1.04,$$
$$k_4 = 6.46, \times 10^{-6} \quad k_5 = 7.97, \times 10^{-8} \quad k_6 = 4.73. \tag{A.3}$$

Since the structure of the analysis program has undergone various major changes during the past two years, including a complete restructuring of the different loops, Equation A.1 does not apply to current versions of the program anymore.

A.2   LALSuite Programs used

Most of the code that was used to prepare the search and conduct the post-processing of the analysis results were self-written python routines. However, in some important steps were conducted with codes from the LALSuite[1] which are organized within a Git[2] repository. The revision of that repository that was used at the time the search was performed is

$$\textbf{SHA1:}11c17498b9c2b1774bc8e14646b7d5a47d72ff35.$$

Routines that were used within this work are:

- `lalapps_HierarchSearchGCT`
  Used in the above revision of the main search and in revision f776289b034e0aaea786d1d933f19c6a7baf73f7 (after bugs have been fixed and more functionality was added) for the post-processing, and for all studies in which data was analyzed in the same way as in the original search: mismatch studies, false dismissal studies, validation studies, and the upper limit procedure.

- `lalapps_PredictFStatistic`
  Used to select the data segments by computing the expected $2\mathcal{F}$ value for a given data segment and an assumed gravitational wave signal coming from a given sky position.

- `lalapps_Makefakedata_v4`
  This is a data creation tool; used to create the fake data sets (like pure Gaussian noise data sets and data sets with additional injections) and for the injection of signals into the original search data set.

- `lalapps_ComputeFStatistic_v2`
  Used for the computation of single-segment and single-detector $2\mathcal{F}$ values by a coherent analysis of the single data segments and for the coherent follow-up search.

---

[2]Git is a distributed revision control and source code management tool.

- `lalapps_ComputePSD`

  Used to create the amplitude spectral density of the used data set (see Figure 5.5.5).

- `lalapps_PrintDetectorState`

  Used to compute the antenna pattern functions for the data selection and for the computation of the antenna pattern correction κ (see Equation 5.13 and 6.4).

A.3 THE START TIMES OF THE 630 DATA SEGMENTS

START TIMES	CONT.	CONT.	CONT.	CONT.	CONT.
816141791	816319991	816397391	816494591	816575591	816661991
816834791	816922991	817005791	817101191	817182191	817261391
817353191	817439591	817518791	817610591	817781591	817873391
817959791	818042591	818213591	818298191	818384591	818474591
818557391	818647391	818726591	818818391	818902991	818987591
819077591	819246791	819329591	819419591	819504191	819590591
819676991	819761591	819849791	819930791	820020791	820098191
820279991	820357391	820456391	820540991	820627391	820708391
820798391	820888391	820967591	821057591	821142191	821232191
821313191	821399591	821487791	821665991	821739791	821840591
821917991	822004391	822097991	822178991	822265391	822351791
822434591	822607391	822772991	822868391	822952991	823041191
823201391	823399391	824504591	824599991	824767391	824846591
824927591	825022991	825116591	825204791	825467591	825541391
825624191	825699791	825978791	826066991	826137191	826232591
826311791	826486391	826574591	826660991	826745591	826828391
826927391	827017391	827092991	827177591	827263991	827357591
827433191	827523191	827620391	827688791	827778791	827863391
827946191	828034391	828228791	828833591	829134191	829326791
829414991	829497791	829672391	829758791	829846991	829936991
830039591	830097191	830205191	830277191	830449991	830784791
830881991	830964791	831058391	831313991	831400391	831479591
831569591	831655991	831744191	831846791	831925991	832186991
832255391	832446191	832516391	832703591	832771991	832863791
832946591	833052791	833124791	833211191	833293991	833371391
833459591	833553191	833664791	833731391	833803391	833891591
833979791	834064391	834147191	834330791	834411791	834573791
834667391	834753791	834868991	834933791	835020191	835102991
835189391	835273991	835362191	835524191	835610591	835704191
835788791	835875191	835963391	836049791	836130791	836218991
836308991	836386391	836487191	836560991	836623991	836728391
836816591	836897591	836992991	837082991	837169391	837352991
837426791	837511391	837601391	837682391	837768791	837925391
838024391	838108991	838195391	838283591	838364591	838546391
838636391	838720991	838801991	838882991	838976591	839043191

Table A.3.1: The start times of the 630 used data segments: start times 1-210.

START TIMES	CONT.	CONT.	CONT.	CONT.	CONT.
839149391	839235791	839320391	839408591	839491391	839581391
839649791	839750591	839835191	839912591	840007991	840097991
840184391	840250991	840353591	840439991	840526391	840618191
840699191	840787391	840949391	841127591	841219391	841305791
841390391	841462391	841559591	841647791	841728791	841822391
841888991	841993391	842067191	842157191	842252591	842342591
842421791	842511791	842596391	842671991	842761991	842853791
842936591	843031991	843114791	843199391	843276791	843368591
843465791	843539591	843629591	843746591	843802391	843881591
843973391	844056191	844146191	844234391	844329791	844403591
844486391	844581791	844665591	844752791	844828391	844925591
845010191	845181191	845352191	845440391	845523191	845613191
845694191	845776991	845965991	846048791	846129791	846214391
846300791	846390791	846477191	846559991	846648191	846732791
846813791	846988391	847080191	847164791	847251191	847339391
847506791	847602191	847769591	847846991	847938791	848023391
848106191	848196191	848280791	848372591	848457191	848541791
848629991	848714591	848804591	848881991	848973791	849058391
849144791	849229391	849317591	849402191	849492191	849574991
849664991	849740591	849837791	849924191	850006991	850093391
850172591	850264391	850350791	850435391	850523591	850611791
850690991	850784591	850869191	850955591	851040191	851119391
851383991	851472191	851562191	851646791	851727791	851819591
851898791	851990591	852071591	852159791	852246191	852332591
852417191	852508991	852589991	852764591	852850991	852935591
853025591	853108391	853196591	853275791	853365791	853452191
853815791	854082191	854145191	854238791	854326991	854404391
854487191	854571791	854667191	854748191	854834591	854926391
855009191	855090191	855176591	855262991	855352991	855451991
855532991	855619391	855694991	855775991	855873191	855939791
856053191	856128791	856213391	856301591	856386191	856470791
856555391	856650791	856735391	856818191	856899191	856987391
857075591	857161991	857248391	857331191	857419391	857505791
857586791	857676791	857764991	857865791	857935991	858043991
858130391	858191591	858277991	858324791	858366191	858452591

Table A.3.2: The start times of the 630 used data segments: start times 211-420.

START TIMES	CONT.	CONT.	CONT.	CONT.	CONT.
858540791	858623591	858709991	858798191	858841391	858880991
858972791	859059191	859147391	859188791	859228391	859314791
859361591	859401191	859455191	859510991	859572191	859663991
859739591	859833191	859915991	859998791	860088791	860176991
860274191	860347991	860434391	860518991	860603591	860693591
860778191	860878991	860947391	861037391	861118391	861202991
861289391	861382991	861480191	861552191	861638591	861726791
861811391	861895991	861969791	862088591	862149791	862243391
862333391	862414391	862498991	862587191	862691591	862738391
862848191	862936391	863013791	863101991	863202791	863294591
863361191	863409791	863449391	863508791	863622191	863708591
863787791	863899391	863967791	864055991	864140591	864223391
864302591	864392591	864444791	864504191	864565391	864653591
864745391	864826391	864914591	864993791	865114391	865224191
865270991	865434791	865512191	865600391	865719191	865780391
865852391	865949591	866032391	866120591	866199791	866318591
866379791	866457191	866538191	866633591	866719991	866795591
866862191	866975591	867150191	867236591	867322991	867405791
867583991	867648791	867754991	867848591	867927791	868010591
868068191	868177991	868271591	868357991	868446191	868534391
868611791	868874591	868957391	869047391	869095991	869135591
869220191	869283191	869389391	869477591	869563991	869652191
869736791	869817791	869887991	869983391	870078791	870168791
870255191	870343391	870426191	870492791	870588191	870687191
870773591	870859991	870946391	871034591	871097591	871201991
871282991	871372991	871462991	871549391	871630391	871704191
871804991	871891391	871974191	872062391	872152391	872236991
872307191	872370191	872409791	872454791	872494391	872584391
872665391	872757191	872800391	872841791	872910191	873012791
873093791	873181991	873268391	873356591	873441191	873518591
873590591	873703991	873788591	873871391	873959591	874045991
874121591	874216991	874299791	874387991	874472591	874524791
874564391	874609391	874648991	874726391	874816391	874904591
874985591	875079191	875174591	875246591	875334791	875422991
875514791	875665991	875772191	875854991	876123191	877579391

Table A.3.3: The start times of the 630 used data segments: start times 421-630.

A.4   Data Preparation

The `lalapps_HierarchSearchGCT` analysis program revision that was used for the search was not able to select data from a given directory by, for example, a list that contains the start times of the segments of interest. That is, if the code was pointed to a directory containing SFTs, it would read in all data that is inside that directory. Then the analysis program would pick the SFTs and distribute them over the different segments itself, based on the segment duration (`--tStack` option) and on the number of desired segments (`--nStacksMax` option). This would be done in the following way: it would start with the first SFT that it finds (first in terms of start time) and define the start time of the first segment to be that time. From the segment duration it would compute the end time of that segment. Then it would assign to that segment all SFTs whose data falls within the duration of that segment. The start time of the next segment would then be the start time of the next available SFT (so there might be a gap between the first and the second segment). The data assigned to the second segment would be that from all SFTs whose data falls within the start time of the second segment and the start time of the second segment plus the segment duration. This process would be repeated until the desired number of segments has been constructed. As a consequence, if the user has a specific set of SFTs that one wishes to be used, the `lalapps_HierarchSearchGCT` analysis program needs to be pointed to a directory that contains only such SFTs.

To prepare such a set of data the start point is the science data of S5. As described in Section 5.5, science data is already a selection of the total data that the detectors collect. From those data files we extract only the times that the search will analyze, based on the selection procedure described in Section 5.5.1. The data are stored in the frequency domain, as $1800\,\mathrm{s}$ time baseline Fourier transforms spanning the whole frequency range. We divide them into $1\,\mathrm{Hz}$ band files and choose only those from the frequency band considered in the search. Without the division we would have a single gigantic data file that would lead to unnecessary memory issues when being read by the analysis program.

A.5 THE SYSTEMATIC SHIFT OF THE ANALYSIS RESULTS

For both the comparison with the outcome of a test search with the theoretical expectation (see Figure 5.8.2 and 5.8.3) and the estimate of the effective number of templates used in the search, the resulting $\langle 2\mathcal{F}\rangle$ values need to be corrected for a known systematic bias which is due to the specific implementation of the $2\mathcal{F}$-statistic in the used analysis program. This systematic bias is well understood and documented [99].

For this search the bias has a value of 0.02. Figure A.5.1 shows again the two comparisons of Figure 5.8.2 and 5.8.3, this time without this correction.
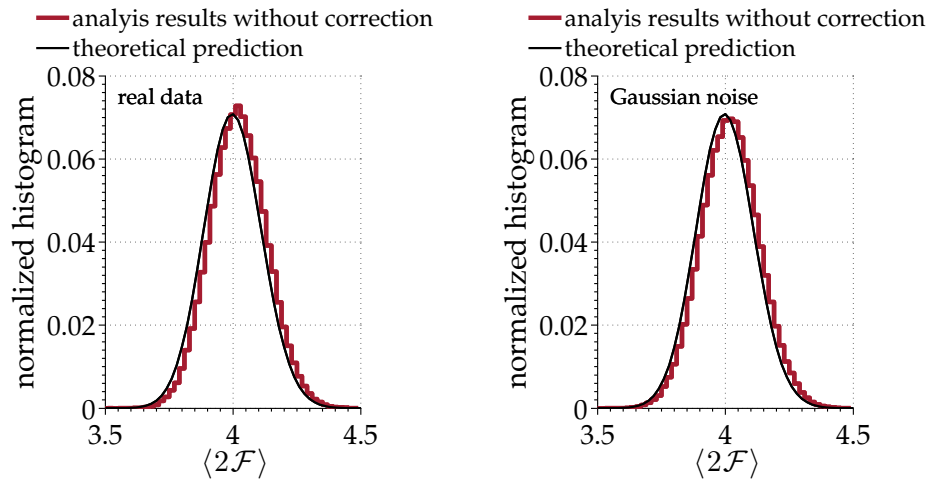
Figure A.5.1: These two plots show the same Figures as in Section 5.8, but this time not correcting for the systematic bias in the analysis results. The histograms are shifted by 0.02 towards larger values.

A.6   KNOWN DISTURBANCES

f	#H	f_{LOW}	f_{HIGH}	CAUSE
1.0	1000	0.9999194	1.0000806	Electronics
60	121	59.96	60.04	Mains Power
93.2903	1	93.2758	93.3048	Optical Lever A
96.7082	1	96.6959	96.7205	Optical Lever B
139.9387	1	139.92	139.958	Optical Lever A
145.0622	1	145.047	145.078	Optical Lever B
186.5874	1	186.565	186.61	Optical Lever A
193.4164	1	193.395	193.437	Optical Lever B
233.2314	1	233.185	233.277	Optical Lever A
241.7774	1	241.713	241.842	Optical Lever B
329.2339	2	329.226	329.242	Violin BS (Wire)
329.3409	2	329.333	329.349	Violin BS (Wire)
329.4025	2	329.389	329.416	Violin BS (Wire)
335.276	1	335.266	335.286	Violin RM (Wire)
335.4100	1	335.396	335.424	Violin RM (Wire)
335.5950	1	335.580	335.610	Violin RM (Wire)
335.7770	1	335.762	335.792	Violin RM (Wire)
342.9424	1	342.925	342.96	Violin Side (Wire)
343.0980	1	343.085	343.111	Violin Mode (Wire)
343.355	1	343.345	343.365	Violin (Wire)
343.4726	1	343.461	343.484	Violin Mode (Wire)
343.6231	1	343.61	343.637	Violin Mode (Wire)
344.266	1	344.256	344.276	Violin (Wire)
344.4132	1	344.402	344.424	Violin Mode (Wire)
346.6349	1	346.613	346.657	Violin Mode (Wire)
346.8060	1	346.794	346.818	Violin Side (Wire)
346.8727	1	346.86	346.886	Violin Side (Wire)
346.9151	1	346.905	346.925	Violin Mode (Wire)
346.9650	1	346.955	346.975	Violin Mode (Wire)
347.0370	1	347.027	347.047	Violin Mode (Wire)
396.7000	1	396.693	396.707	Calibration line

Table A.6.1: The known spectral lines within the search frequency band present in L1 during S5. Columns are the central frequency, the number of harmonics, the low and high frequency sides of the band and the origin of the disturbance.

f	#H	f_{LOW}	f_{HIGH}	CAUSE
1.0	1000	0.9999194	1.0000806	Electronics
60	121	59.96	60.04	Mains Power
85.80	1	85.79	85.81	LVEA RackMag (Electronics)
89.9	1	89.84	89.96	5V lsc aux lo Power Supply
93.05	1	93.04	93.06	BSC 10 MI Cand MAG
93.25	1	93.24	93.26	MMT 1-2-3 Shadow Sensors
139.95	1	139.94	139.96	+15V Supply Ripple
164.52	1	164.51	164.53	dscl 2+5V (Electronics)
329.51	2	329.50	329.52	Violin BS (Wire)
329.58	1	329.56	329.59	Demod Mag (Electronics)
329.59	2	329.58	329.60	Violin BS (Wire)
329.70	2	329.68	329.71	Violin BS (Wire)
329.78	2	329.76	329.79	Violin BS (Wire)
329.86	1	329.85	329.87	Demod Mag (Electronics)
335.6950	1	335.680	335.710	Violin RM (Wire)
335.7230	1	335.708	335.738	Violin RM (Wire)
335.7410	1	335.726	335.756	Violin RM (Wire)
335.8200	1	335.805	335.835	Violin RM (Wire)
343.2879	1	343.271	343.305	Violin (Wire)
343.4145	1	343.404	343.425	ETMX? Violin Mode (Wire)
343.9272	1	343.917	343.938	ETMX? Violin (Wire)
344.0584	1	344.048	344.069	ETMX? ViolinMode (Wire)
344.5247	1	344.509	344.54	ETMX? Violin (Wire)
344.6685	1	344.657	344.68	ETMY Violin (Wire)
344.7186	1	344.702	344.735	ETMY ViolinMode (Wire)
344.8280	1	344.819	344.837	ETMY? ViolinMode (Wire)
347.1824	1	347.17	347.194	ITMX? Violin (Wire)
347.3107	1	347.3	347.321	ITMX? ViolinMode (Wire)
347.3635	1	347.35	347.377	Violin (Wire)
347.5099	1	347.499	347.521	ITMX? ViolinMode (Wire)
347.5818	1	347.567	347.596	Violin (Wire)
347.6860	1	347.674	347.698	ITMY? ViolinMode (Wire)
347.7230	1	347.713	347.733	ITMY ViolinMode (Wire)
393.1000	1	393.093	393.107	Calibration line

Table A.6.2: The known spectral lines within the search frequency band present in H1 during S5. CColumns are the central frequency, the number of harmonics, the low and high frequency sides of the band and the origin of the disturbance (marked with a question mark if origin could not finally be confirmed).

A.7 Tuning the Segment Resolution Veto for Second Order Spindown Signals

While being aware of the fact that this search is not set up to detect signals with high values of the second order spindown, they play an important role in the standard picture of gravitational wave creation. Therefore, a lot of effort went into the development of the segment resolution veto in order to find an approach that does not have a too large false dismissal rate for second order spindown signals as well as the targeted population of signals. The approach that was finally used indeed has a very small false dismissal rate even for high second order spindown signals of 2.8%. Figure A.7.1 shows the per-segment $2\mathcal{F}$ values from an analysis that considered only the first order spindown (like our search) of a data set that contains a second order spindown signal. The x-axis is the GPS start time of the 630 single segments. Due to the second order spindown, the signal sweeps through the frequency-spindown parameter space of the search during less than $1/3$ of the segments which are the ones between GPS time $\sim 8.4 \times 10^8$ s and $\sim 8.5 \times 10^8$ s and which display enhanced values of $2\mathcal{F}$.

The extent of the enhanced values depends on the signal's parameters and Figure A.7.1 is meant as a pictorial representation of the behavior of the signals with a second order spindown. The example signal shown in Figure A.7.1 has a frequency $f = 82.13$ Hz, a spindown value $\dot{f} = -1.13 \times 10^{-08}$ Hz/s, and a second order spindown of $\ddot{f} = -1.79 \times 10^{-18}$ Hz/s^2. The veto described in Section 6.5 is robust and safe because it relies on there being just a single $2\mathcal{F}$ value much above the average which is highly unlikely even among the highest second order spindown signals.
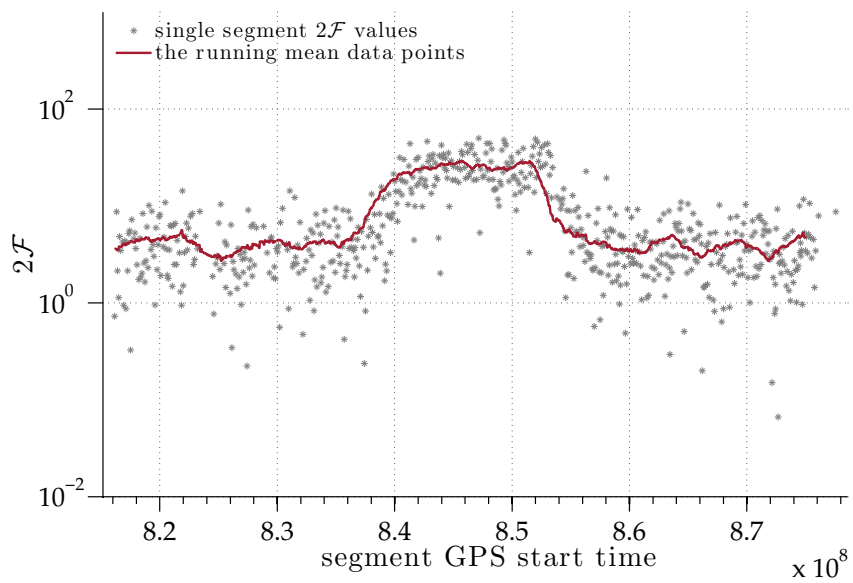
Figure A.7.1: A typical second order spindown signal. The plot shows the resulting $2\mathcal{F}$ values of the coherent analyses of the 630 data segments over the start time of each segment as black dots. On top the result of a running mean using a window size of 62×11.5 hours is shown in red color.

A.8   Doppler Effects on the Spindown

The targeted star population orbits the black hole at the center of the Galaxy in very small orbits. Due to the tight orbits, very fast motions are expected. These motions could, in principle, have a significant effect on the apparent first and second order frequency derivatives. Estimating the gravitational potential of the black hole at $0.38\,\mathrm{pc}$ (the extension of the central cluster, see Section 2.3), yields:

$$\frac{GM}{rc^2} = 5.04 \times 10^{-7}, \tag{A.4}$$

with a mass of the black hole of $M \sim 4 \times 10^6\,M_\odot$. The acceleration of a test mass in the gravitational potential is

$$a = \dot{v} = \frac{MG}{r^2}, \tag{A.5}$$

hence, the effect on the first frequency derivative can be estimated to be:

$$\dot{f} \sim \frac{GM}{r^2}\frac{f}{c} \sim 1.3 \times 10^{-12}\,\mathrm{Hz/s}. \tag{A.6}$$

The Doppler effect does not impact the first order spindown, because it is negligible with respect to the covered values. The same estimate can be done for the second order frequency derivative. With

$$\dot{a} = \ddot{v} = \frac{GM}{r^3}\dot{r}, \tag{A.7}$$

the effect on the second order spindown is of the order:

$$\ddot{f} \sim \frac{GM}{r^3}\frac{f}{c^2}\frac{v}{c} \sim 2.34 \times 10^{-23}\,\mathrm{Hz/s^2}, \tag{A.8}$$

where the velocity dispersion is obtained from [64] and estimated with $v^2 = GM/r$. The contribution of the Doppler effect of the central black hole to the second order spindown values is negligible.

Acronyms

ATLAS   The ATLAS compute cluster at the Max-Planck-Institut für Gravitationsphysik (Albert-Einstein-Institut) in Hanover, Germany. 50, 62, 115

BS   Beam splitter 23

eLISA   Evolved LISA is a planned space-based Michelson interferometer which consists of one mother- and two daughter spacecraft separated by a distance of 10^6 km. See also *NGO*. 23

EOS   Equation of state of a neutron star 11, 13

ESA   European Space Agency 23

ETM   End test mass of a Michelson interferometer 26

GEO600   600-m long gravitational wave detector installed near Hanover, Germany. 22

H1   4-km long gravitational wave detector at the LIGO Hanford Observatory, Washington. 24, 30, 51, 52, 54–56, 96, 102, 104, 141, 146

H2   2-km long gravitational wave detector which was formerly installed within the same vacuum system as H1 at the LIGO Hanford Observatory, Washington. 24, 29

ITM   Input test mass of a Michelson interferometer 26

KaGra   Future gravitational wave detector located in the Kamioka mine, Japan, which is expected to start its operation in 2018. 22

L1   4-km long gravitational wave detector at the LIGO Livingston Observatory in Louisiana. 24, 30, 51, 52, 54–56, 96, 102, 104, 140, 146

LALSuite	The LALSuite is a library of gravitational wave data analysis routines written in C following the ISO/IEC 9899 : 1999 standard (more commonly known as C99) and is available at www.lsc-group.phys.uwm.edu/daswg/projects/lalsuite.html. 52, 90, 131, 133, 146
LIGO	Laser Interferometer Gravitational-Wave Observatory 10, 22, 24, 25, 27, 29, 30, 51, 100, 116, 130, 146, 147
LISA	Laser Interferometer Space Antenna 22, 23
LSC	LIGO Scientific Collaboration 161
MC	Mode cleaner 26
MLE	Maximum likelihood estimators 40
MMT	Mode matching telescope 26
NASA	National Aeronautics Space Administration 23
NGO	NGO is a planned space-based Michelson interferometer which consists of one mother- and two daughter spacecraft separated by a distance of 10^6 km. See also *eLISA*. 23
PD	Photo diode 28
PSR3	The pulsar hardware injection PSR3 was induced into the H1 and L1 detectors by adding signals to the interferometer length sensing and control system that cause mirror motions equal to the motions expected by a continuous gravitational wave passing by the interferometer. PSR3 mimics a pulsar with frequency and spindown parameters within the searched parameter space. It's location in sky is close enough to the coordinates of Sgra that it was recovered by this search. xiv, 99–106, 123, 146
RM	Recycling mirror 26
S5	The fifth Science Run of the LIGO detectors. It started on November 4, 2005, at 16:00 UTC at Hanford and on November 14, 2005, at 16:00 UTC at Livingston. S5 ended on October 1, 2007, at 00:00 UTC. See also *Science Run*. 25, 30, 51, 52, 54–56, 102, 106, 138, 140, 141, 146

Science Run   The time periods in which the gravitational wave detectors are focused on collecting science data, only interrupted by four hours weekly maintenance work, are called Science Runs. Until today, the LIGO detectors have performed six Science Runs: S1 (23.08.2002 - 09.09.2002), S2 (14.02.2003 - 14.04.2003), S3 (31.10.2003 - 09.01.2003), S4 (22.02.2005 - 23.03.2005), S5 (04.11.2005 - 30.07.2007) and S6 (07.07.2009 - 20.10.2010). For more information about the detectors and the different Science Runs the interested reader is referred to [31]. 25, 51, 55, 56

SFT   Short Fourier transform 52–58, 68, 76, 91, 96, 97, 104, 105, 131, 132, 138

Sgr A*   Sagittarius A* 2, 17–19, 45, 53, 58–60, 93, 95, 127

SNR   Signal-to-noise ratio 41, 91, 92

SSB   Solar system barycenter frame 34, 35, 102

TAMA300   Gravitational wave detector located at the Mitaka campus of the National Astronomical Observatory of Japan. 22

TM   Test mass 23

Virgo   3-km-long gravitational wave detector in Cascina, Italy. 10, 22, 130

References

[1] J. Aasi et al., *Searching for continuous gravitational waves from the Galactic Center*, in preparation, to appear in Physical Review D.

[2] J. Aasi et al., *The characterization of Virgo data and its impact on gravitational-wave searches*, Classical and Quantum Gravity, 29 (2012), p. 155002.

[3] J. Aasi et al., *Einstein@Home all-sky search for periodic gravitational waves in LIGO S5 data*, Physical Review D, 87 (2013), p. 042001.

[4] J. Aasi et al., *Search for Gravitational Waves from Binary Black Hole Inspiral, Merger and Ringdown in LIGO-Virgo Data from 2009-2010*, Physical Review D, 87 (2013).

[5] J. Abadie, B. P. Abbott, R. Abbott, M. Abernathy, T. Accadia, et al., *Directional limits on persistent gravitational waves using LIGO S5 science data*, Physical Review Letters, 107 (2011), p. 271102.

[6] J. Abadie et al., *Calibration of the LIGO Gravitational Wave Detectors in the Fifth Science Run*, Nuclear Instruments and Methods, A624 (2010), pp. 223–240.

[7] J. Abadie et al., *First search for gravitational waves from the youngest known neutron star*, Astrophysical Journal, 722 (2010), pp. 1504–1513.

[8] J. Abadie et al., *First search for gravitational waves from the youngest known neutron star*, Astrophysical Journal, 722 (2010), pp. 1504–1513.

[9] J. Abadie et al., *Predictions for the Rates of Compact Binary Coalescences Observable by Ground-based Gravitational-wave Detectors*, Classical and Quantum Gravity, 27 (2010), p. 173001.

[10] J. Abadie et al., *Search for gravitational-wave inspiral signals associated with short Gamma-Ray Bursts during LIGO's fifth and Virgo's first science run*, Astrophysical Journal, 715 (2010), pp. 1453–1461.

[11] J. Abadie et al., *A search for gravitational waves associated with the August 2006 timing glitch of the Vela pulsar*, Physical Review D, 83 (2011), p. 042001.

[12] J. Abadie et al., *Beating the spin-down limit on gravitational wave emission from the Vela pulsar*, Astrophysical Journal, 737 (2011), p. 93.

[13] J. Abadie et al., *Search for Gravitational Wave Bursts from Six Magnetars*, Astrophysical Journal, 734 (2011), p. L35.

[14] J. Abadie et al., *Search for gravitational waves from binary black hole inspiral, merger and ringdown*, Physical Review D, 83 (2011), p. 122005.

[15] J. Abadie et al., *All-sky search for gravitational-wave bursts in the second joint LIGO-Virgo run*, Physical Review D, 85 (2012), p. 122007.

[16] J. Abadie et al., *All-sky Search for Periodic Gravitational Waves in the Full S5 LIGO Data*, Physical Review D, 85 (2012), p. 022001.

[17] J. Abadie et al., *Implications For The Origin Of GRB 051103 From LIGO Observations*, Astrophysical Journal, 755 (2012), p. 2.

[18] J. Abadie et al., *Search for Gravitational Waves from Intermediate Mass Binary Black Holes*, Physical Review D, 85 (2012), p. 102004.

[19] J. Abadie et al., *Search for Gravitational Waves from Low Mass Compact Binary Coalescence in LIGO's Sixth Science Run and Virgo's Science Runs 2 and 3*, Physical Review D, 85 (2012), p. 082002.

[20] J. Abadie et al., *Upper limits on a stochastic gravitational-wave background using LIGO and Virgo interferometers at 600-1000 Hz*, Physical Review D, 85 (2012), p. 122001.

[21] B. P. Abbott et al., *Setting upper limits on the strength of periodic gravitational waves using the first science data from the GEO 600 and LIGO detectors*, Physical Review D, 69 (2004), p. 082004.

[22] B. P. Abbott et al., *First all-sky upper limits from LIGO on the strength of periodic gravitational waves using the Hough transform*, Physical Review D, 72 (2005), p. 102004.

[23] B. P. Abbott et al., *Searches for periodic gravitational waves from unknown isolated sources and Scorpius X-1: Results from the second LIGO science run*, Physical Review D, 76 (2007), p. 082001.

[24] B. P. ABBOTT ET AL., *Upper limit map of a background of gravitational waves*, Physical Review D, 76 (2007), p. 082003.

[25] B. P. ABBOTT ET AL., *All-sky search for periodic gravitational waves in LIGO S4 data*, Physical Review D, 77 (2008), p. 022001.

[26] B. P. ABBOTT ET AL., *Beating the spin-down limit on gravitational wave emission from the Crab pulsar*, Astrophysical Journal Letters, 683 (2008), p. L45.

[27] B. P. ABBOTT ET AL., *All-sky LIGO Search for Periodic Gravitational Waves in the Early S5 Data*, Physical Review Letters, 102 (2009), p. 111102.

[28] B. P. ABBOTT ET AL., *Beating the Spin-Down Limit on Gravitational Wave Emission from the Crab Pulsar*, Astrophysical Journal, 706 (2009), p. L203.

[29] B. P. ABBOTT ET AL., *Einstein@Home search for periodic gravitational waves in early S5 LIGO data*, Physical Review D, 80 (2009), p. 042003.

[30] B. P. ABBOTT ET AL., *Einstein@Home search for periodic gravitational waves in LIGO S4 data*, Physical Review D, 79 (2009), p. 022001.

[31] B. P. ABBOTT ET AL., *LIGO: The Laser interferometer gravitational-wave observatory*, Reports on Progress in Physics., 72 (2009), p. 076901.

[32] B. P. ABBOTT ET AL., *Search for gravitational-wave bursts associated with gamma-ray bursts using data from LIGO Science Run 5 and Virgo Science Run 1*, Astrophysical Journal, 715 (2010), pp. 1438–1452.

[33] B. P. ABBOTT ET AL., *Searches for gravitational waves from known pulsars with S5 LIGO data*, Astrophysical Journal, 713 (2010), p. 671.

[34] B. P. ABBOTT ET AL., *Searches for gravitational waves from known pulsars with S5 LIGO data*, Astrophysical Journal, 713 (2010), pp. 671–685.

[35] B. P. ABBOTT ET AL., *Implementation and testing of the first prompt search for gravitational wave transients with electromagnetic counterparts*, ArXiv e-print, 1109.3498 (2011).

[36] R. ADHIKARI, A. BENGSTON, Y. BUCHLER, T. DELKER, D. REITZE, Q. S. D. TANNER, AND S. YOSHIDA, *Input Optics Final Design*, LIGO technical document T980009-01-D.

[37] S. ADRIAN-MARTINEZ ET AL., *A First Search for coincident Gravitational Waves and High Energy Neutrinos using LIGO, Virgo and ANTARES data from 2007*, ArXiv e-print, 1205.3018 (2012).

[38] O. D. Aguiar, *The Past, Present and Future of the Resonant-Mass Gravitational Wave Detectors*, Research in Astronomy and Astrophysics, 11 (2011), pp. 1–42.

[39] N. Andersson, *A New class of unstable modes of rotating relativistic stars*, Astrophysical Journal, 502 (1998), pp. 708–713.

[40] N. Andersson, K. Kokkotas, and B. F. Schutz, *Gravitational radiation limit on the spin of young neutron stars*, Astrophysical Journal, 510 (1999), p. 846.

[41] N. Andersson and K. D. Kokkotas, *The R-mode instability in rotating neutron stars*, International Journal of Modern Physics D, 10 (2001), pp. 381–442.

[42] W. Baade and F. Zwicky, *Supernovae and cosmic rays*, Physical Review, 45 (1934).

[43] F. K. Baganoff, Y. Maeda, M. Morris, M. Bautz, W. Brandt, W. Cui, J. Doty, E. Feigelson, G. Garmire, S. Pravdo, et al., *Chandra X-ray spectroscopic imaging of Sagittarius A* and the central parsec of the galaxy*, The Astrophysical Journal, 591 (2003), p. 891.

[44] E. E. Becklin and G. Neugebauer, *Infrared Observations of the Galactic Center*, Astrophysical Journal, 151 (1968), p. 145.

[45] B. Behnke and M. A. Papa, *Post-Processing Methods to increase the Sensitivity of targeted Continuous Gravitational Wave Searches*, in preparation.

[46] M. Bejger, T. Bulik, and P. Haensel, *Moments of inertia of the binary pulsars J0737-3039A,B and the dense matter EOS*, Monthly Notices of the Royal Astronomical Society, 364 (2005), p. 635.

[47] L. Bildsten, *Gravitational radiation and rotation of accreting neutron stars*, Astrophysical Journal Letters, 501 (1998), p. L89.

[48] M. A. Bizouard and M. Alessandra Papa, *Searching for gravitational waves with the LIGO and Virgo interferometers*, ArXiv e-prints, 1304.4984 (2013).

[49] E. D. Black, *An introduction to Pound-Drever-Hall laser frequency stabilization*, American Journal of Physics, 69 (2001), pp. 79–87.

[50] S. Bowyer, E. T. Byram, T. A. Chubb, and H. Friedman, *Lunar occultation of X-ray emission from the Crab nebula*, Science, 146 (1964), pp. 912–917.

[51] P. R. Brady and T. Creighton, *Searching for periodic sources with LIGO. II: Hierarchical searches*, Physical Review D, 61 (2000), p. 082001.

[52] P. R. Brady, T. Creighton, C. Cutler, and B. F. Schutz, *Searching for periodic sources with LIGO*, Physical Review D, 57 (1998), pp. 2101–2116.

[53] S. M. Carroll, *Lecture notes on general relativity*, (1997).

[54] J. M. Cordes and G. Greenstein, *Pulsar timing. IV – Physical models for timing noise processes*, Astrophysical Journal, 245 (1981), pp. 1060–1079.

[55] C. Cutler and B. F. Schutz, *The Generalized $\mathcal{F}$-statistic: Multiple detectors and multiple GW pulsars*, Physical Review D, 72 (2005), p. 063006.

[56] J. S. Deneva, J. M. Cordes, and T. J. W. Lazio, *Discovery of Three Pulsars from a Galactic Center Pulsar Population*, Astrophysical Journal, 702 (2009), pp. L177–L181.

[57] R. W. P. Drever, J. L. Hall, F. V. Kowalski, J. Hough, G. M. Ford, A. J. Munley, and H. Ward, *Laser phase and frequency stabilization using an optical resonator*, Applied Physics B: Lasers and Optics, 31 (1983), pp. 97–105.

[58] A. Eckart and R. Genzel, *Observations of stellar proper motions near the galactic centre*, Nature, 383 (1996), pp. 415–417.

[59] A. Eckart, R. Schödel, and C. M. Straubmeier, *The black hole at the center of the Milky Way*, Imperial College Press, 2005.

[60] S. Fairhurst, *Improved source localization with LIGO India*, ArXiv e-print, 1205.6611 (2012).

[61] C.-A. Faucher-Giguere and V. Kaspi, *40 Years of Pulsars: The Birth and Evolution of Isolated Radio Pulsars*, ArXiv e-print, 0710.4518 (2007).

[62] D. Figer, *Massive Star Formation in the Galactic Center*, ArXiv e-print, 0803.1619 (2008).

[63] J. L. Friedman and S. M. Morsink, *Axial instability of rotating relativistic stars*, Astrophysical Journal, 502 (1998), p. 714.

[64] R. Genzel, F. Eisenhauer, and S. Gillessen, *The Galactic Center Massive Black Hole and Nuclear Star Cluster*, ArXiv e-print, 1006.0064 (2010).

[65] A. Ghez, B. Klein, M. Morris, and E. Becklin, *High proper-motion stars in the vicinity of sagittarius a*: Evidence for a supermassive black hole at the center of our galaxy*, The Astrophysical Journal, 509 (1998), p. 678.

[66] A. Ghez, M. Morris, E. E. Becklin, T. Kremenek, and A. Tanner, *The Accelerations of stars orbiting the Milky Way's central black hole*, Nature, 407 (2000), p. 349.

[67] R. Giacconi, H. Gursky, and B. B. Paolini, F. R. and99 Rossi, *Evidence for X-rays from sources outside the solar system*, Physical Review Letters, 9 (1962), pp. 439–443.

[68] S. Gillessen, F. Eisenhauer, S. Trippe, T. Alexander, R. Genzel, F. Martins, and T. Ott, *Monitoring stellar orbits around the massive black hole in the galactic center*, The Astrophysical Journal, 692 (2009), p. 1075.

[69] T. Gold, *Rotating neutron stars as the origin of the pulsating radio sources*, Nature, 218 (1968), pp. 731–732.

[70] P. Haensel, P. Haensel, A. Y. Potekhin, and D. G. Yakovlev, *Neutron Stars 1: Equation of State and Structure*, Astrophysics and Space Science Library, Springer, 2006.

[71] J. Hartle, *Gravity: An Introduction to Einstein's General Relativity*, Addison-Wesley, Boston, 2003.

[72] B. Haskell, N. Andersson, D. I. Jones, and L. Samuelsson, *Are Neutron Stars with Crystalline Color-Superconducting Cores Relevant for the LIGO Experiment?*, Physical Review Letters, 99 (2007), p. 231101.

[73] A. Hewish, S. J. Bell, P. J. D. H., S. P. F., and R. A. Collins, *Observation of a rapidly rotating radio source*, Nature, 217 (1968), pp. 709–713.

[74] C. J. Horowitz and K. Kadau, *Breaking Strain of Neutron Star Crust and Gravitational Waves*, Physical Review Letters, 102 (2009), p. 191102.

[75] V. S. Imshennik and D. K. Nadyozhin, *Supernova 1987A in the Large Magellanic Cloud: Observations and theory*, Uspekhi Fizicheskikh Nauk, 156 (1988), pp. 561–651.

[76] P. JARANOWSKI, A. KRÓLAK, AND B. F. SCHUTZ, *Data analysis of gravitational-wave signals from spinning neutron stars: The signal and its detection*, Physical Review D, 58 (1998), p. 063001.

[77] S. JOHNSTON ET AL., *Discovery of two pulsars towards the Galactic Centre*, Monthly Notices of the Royal Astronomical Society Letters, 373 (2006), pp. L6–L10.

[78] K. D. KOKKOTAS, T. A. APOSTOLATOS, AND N. ANDERSSON, *The inverse problem for pulsating neutron stars: a 'fingerprint analysis' for the supranuclear equation of state*, Monthly Notices of the Royal Astronomical Society, 320 (2001), pp. 307–315.

[79] B. KRISHNAN, A. M. SINTES, M. A. PAPA, B. F. SCHUTZ, S. FRASCA, AND C. PALOMBA, *Hough transform search for continuous gravitational waves*, Physical Review D, 70 (2004), p. 082001.

[80] B. D. LACKEY, *Undergraduate honors thesis*, Pennsylvania State University, (2006).

[81] B. D. LACKEY, M. NAYYAR, AND B. J. OWEN, *Observational constraints on hyperons in neutron stars*, Physical Review D, 73 (2006), p. 024021.

[82] L. D. LANDAU, *On the theory of stars*, Physikalische Zeitschrift der Sowjetunion, 1 (1932).

[83] M. B. LARSON AND B. LINK, *Simulation of glitches in isolated pulsars*, Monthly Notices of the Royal Astronomical Society, 333 (2002), pp. 613–622.

[84] U. LEE AND S. YOSHIDA, *r-modes of neutron stars with superfluid cores*, Astrophysical Journal, 586 (2003), pp. 403–418.

[85] L. LIN, *Constraining crystalline color superconducting quark matter with gravitational-wave data*, Physical Review D, 76 (2007), p. 081502.

[86] D. R. LORIMER, *Binary and Millisecond Pulsars*, Living Reviews in Relativity, 11 (2008).

[87] A. LYNE AND F. GRAHAM-SMITH, *Pulsar Astronomy*, Cambridge University Press, Cambridge, 3 ed., 2006.

[88] R. N. MANCHESTER, *Proceedings of the 12th Marcel Grossmann Meeting, Paris*, World Scientific, (2009).

[89] R. N. Manchester, G. B. Hobbs, A. Teoh, and M. Hobbs, *The ATNF Pulsar Catalogue*, Astronomical Journal, 129 (2005), pp. 1993–2006.

[90] P. N. McDermott, H. M. Van Horn, and C. J. Hansen, *Nonradial oscillations of neutron stars*, Astrophysical Journal, 325 (1988), pp. 725–748.

[91] C. W. Misner, K. S. Thorne, and J. A. Wheeler, *Gravitation*, W. H. Freeman, San Francisco, 1973.

[92] J. Neyman and E. S. Pearson, *On the Problem of the most Efficient Tests of Statistical Hypotheses*, The Royal Society, 231 (1933), pp. 289–337.

[93] B. J. Owen, *Maximum Elastic Deformations of Compact Stars with Exotic Equations of State*, Physical Review Letters, 95 (2005), p. 211101.

[94] B. J. Owen, L. Lindblom, C. Cutler, B. F. Schutz, A. Vecchio, et al., *Gravitational waves from hot young rapidly rotating neutron stars*, Physical Review D, 58 (1998), p. 084020.

[95] V. R. Pandharipande, D. Pines, and R. A. Smith, *Neutron star structure: theory, observation, and speculation*, Astrophysical Journal, 208 (1976), pp. 550–566.

[96] E. Pfahl and A. Loeb, *Probing the spacetime around Sgr A* with radio pulsars*, Astrophysical Journal, 615 (2004), pp. 253–258.

[97] H. J. Pletsch, *Parameter-space correlations of the optimal statistic for continuous gravitational-wave detection*, Physical Review D, 78 (2008), p. 102005.

[98] H. J. Pletsch and B. Allen, *Exploiting Large-Scale Correlations to Detect Continuous Gravitational Waves*, Physical Review Letters, 103 (2009), p. 181102.

[99] R. Prix, *$\mathcal{F}$-statistic bias in noise-estimator.* (last visited 2013-04-29) http://www.aei.mpg.de/~repr/EnoteEntries/FstatNoiseBias.pdf.

[100] R. Prix, *Search for continuous gravitational waves: Metric of the multidetector $\mathcal{F}$-statistic*, Physical Review D, 75 (2007), p. 023004.

[101] R. Prix, *Search for continuous gravitational waves: Metric of the multidetector $\mathcal{F}$-statistic*, Physical Review D, 75 (2007), p. 023004.

[102] R. Prix and K. Wette, *Estimating sensitivity of the Einstein@Home search S5R5*, LIGO Technical Document T1200272, (2012).

[103] K. Riles, *Gravitational Waves: Sources, Detectors and Searches*, ArXiv e-print, 1209.0667 (2012).

[104] ROG Collaboration, P. Astone, M. Bassan, E. Coccia, S. D. Antonio, V. Fafone, G. Giordano, A. Marini, Y. Minenkov, I. Modena, A. Moleti, G. V. Pallottino, G. Pizzella, A. Rocchi, F. Ronga, R. Terenzi, and M. Visco, *Analysis of 3 years of data from the gravitational wave detectors EXPLORER and NAUTILUS*, ArXiv e-prints, 1212.5202 (2012).

[105] B. Sathyaprakash and B. F. Schutz, *Physics, Astrophysics and Cosmology with Gravitational Waves*, Living Reviews in Relativity, 12 (2009).

[106] P. R. Saulson, *Fundamentals of Interferometric Gravitational Wave Detectors*, World Scientific, 1994.

[107] T. Schoerck, N. Christlieb, J. G. Cohen, T. C. Beers, S. J. Shectman, et al., *The stellar content of the Hamburg/ESO survey. V. The metallicity distribution function of the Galactic halo*, ArXiv e-print, 0809.1172 (2008).

[108] B. F. Schutz, *A First Course in General Relativity*, Cambridge University Press, 2009.

[109] D. A. Shaddock, *An Overview of the Laser Interferometer Space Antenna*, Publications of the Astronomical Society of Australia, 26 (2009), pp. 128–132.

[110] K. Somiya, *Detector configuration of KAGRA–the Japanese cryogenic gravitational-wave detector*, Classical and Quantum Gravity, 29 (2012), p. 124007.

[111] N. Stergioulas, *Rotating stars in relativity*, Living Reviews in Relativity, 6 (2003).

[112] t. V. C. The LIGO Collaboration, *The LSC-Virgo white paper on gravitational wave data analysis - Science goals, status and plans, priorities (2011/2012 edition)*, LIGO Report T1103322, Virgo Report VIR-0353A-11, (2011).

[113] S. E. Thorsett and D. Chakrabarty, *Neutron star mass measurements. 1. Radio pulsars*, Astrophysical Journal, 512 (1999), p. 288.

[114] A. Unsöld and B. Baschek, *Der neue Kosmos*, Springer-Verlag, 5 ed., 1991.

[115] R. M. Wald, *General Relativity*, University Of Chicago Press, 1984.

[116] A. Watts, B. Krishnan, L. Bildsten, and B. F. Schutz, *Detecting gravitational wave emission from the known accreting neutron stars*, Monthly Notices of the Royal Astronomical Society, 389 (2008), pp. 839–868.

[117] J. Weber, *Observation of the thermal fluctuations of a gravitational-wave detector*, Physical Review Letters, 17 (1966), pp. 1228–1230.

[118] S. Weinberg, *Gravitation and Cosmology: Principles and Applications of the General Theory of Relativity*, Wiley, New York, 1972.

[119] J. M. Weisberg and J. H. Taylor, *Relativistic Binary Pulsar B1913+16: Thirty Years of Observations and Analysis*, ASP Conference Series, 328 (2005), p. 25.

[120] K. Wette, *Estimating the sensitivity of wide-parameter-space searches for gravitational-wave pulsars*, Physical Review D, 85 (2012), p. 042003.

[121] C. M. Will, *The binary pulsar, gravitational waves, and the Nobel Prize*, Uspekhi Fizicheskikh Nauk, 37 (1994), pp. 697–704.

[122] M. Zimmermann, *Revised estimate of gravitational radiation from Crab and Vela pulsars*, Nature, 271 (1978).

Curriculum Vitæ

Personal Information

Berit Behnke
Born on June 13th, 1983, in Wolfenbüttel

Education

01/2009 - 04/2009	Participation in the *Astrowatch*-Program at the *LIGO Hanford Observatory*, Washington, USA
2008-2013	Doctoral studies at the *Leibniz Universität Hannover*, stipend of the *International Max Planck Research School on Gravitational Wave Astronomy*
2008	Diploma degree, *Universität Hamburg*, Title of diploma thesis: *Stabilization of the H2 LIGO detector in high power operation*
01/2008 - 04/2008	Participation in the *Astrowatch*-Program at the *LIGO Hanford Observatory*, Washington, USA
2007 - 2008	Stipend of the *International Max Planck Research School on Gravitational Wave Astronomy*
04/2005 - 10/2006	Research assistant at the astronomical observatory of the *Universität Hamburg*
2003 - 2008	Stipend of the *Siemens AG* within the *Young Ladies Network of Technology (Yolante)*
2002 - 2008	Diploma studies of physics, *Universität Hamburg*
2002	Abitur, *Gymnasium im Schloß*, Wolfenbüttel
10/2001	Advancement award of the *ministry of education and cultural affairs* for the research paper *Energiebilanzierung bei der Umkehrung des Peltier-Effektes*
1989 - 2002	Elementary and secondary school

Listing of Publications

My publications

- B. Behnke and M. A. Papa, *Post-Processing Methods to increase the Sensitivity of targeted Continuous Gravitational Wave Searches*, in preparation

- J. Aasi et al., *Searching for continuous gravitational waves from the Galactic Center*, in preparation, to appear in Physical Review D

- T. Schoerck, N. Christlieb, J. G. Cohen, T. C. Beers, S. J. Shectman, et al., *The stellar content of the Hamburg/ESO survey. V. The metallicity distribution function of the Galactic halo*, ArXiv e-print, 0809.1172 (2008)

Publications as member of the LIGO Scientific Collaboration (LSC)

- J. Aasi et al., *Search for Gravitational Waves from Binary Black Hole Inspiral, Merger and Ringdown in LIGO-Virgo Data from 2009-2010*, Physical Review D, 87 (2013)

- J. Aasi et al., *Einstein@Home all-sky search for periodic gravitational waves in LIGO S5 data*, Physical Review D, 87 (2013), p. 042001

- S. Adrian-Martinez et al., *A First Search for coincident Gravitational Waves and High Energy Neutrinos using LIGO, Virgo and ANTARES data from 2007*, ArXiv e-print, 1205.3018 (2012)

- J. Aasi et al., *The characterization of Virgo data and its impact on gravitational-wave searches*, Classical and Quantum Gravity, 29 (2012), p. 155002

- J. Abadie et al., *All-sky search for gravitational-wave bursts in the second joint LIGO-Virgo run*, Physical Review D, 85 (2012), p. 122007

- J. Abadie et al., *Search for Gravitational Waves from Intermediate Mass Binary Black Holes*, Physical Review D, 85 (2012), p. 102004

- J. Abadie et al., *Implications For The Origin Of GRB 051103 From LIGO Observations*, Astrophysical Journal, 755 (2012), p. 2

- J. Abadie et al., *Upper limits on a stochastic gravitational-wave background using LIGO and Virgo interferometers at 600-1000 Hz*, Physical Review D, 85 (2012), p. 122001

- J. Abadie et al., *Search for Gravitational Waves from Low Mass Compact Binary Coalescence in LIGO's Sixth Science Run and Virgo's Science Runs 2 and 3*, Physical Review D, 85 (2012), p. 082002

- J. Abadie et al., *All-sky Search for Periodic Gravitational Waves in the Full S5 LIGO Data*, Physical Review D, 85 (2012), p. 022001

- B. P. Abbott et al., *Implementation and testing of the first prompt search for gravitational wave transients with electromagnetic counterparts*, ArXiv e-print, 1109.3498 (2011)

- J. Abadie, B. P. Abbott, R. Abbott, M. Abernathy, T. Accadia, et al., *Directional limits on persistent gravitational waves using LIGO S5 science data*, Physical Review Letters, 107 (2011), p. 271102

- J. Abadie et al., *Beating the spin-down limit on gravitational wave emission from the Vela pulsar*, Astrophysical Journal, 737 (2011), p. 93

- J. Abadie et al., *Search for gravitational waves from binary black hole inspiral, merger and ringdown*, Physical Review D, 83 (2011), p. 122005

- J. Abadie et al., *Search for Gravitational Wave Bursts from Six Magnetars*, Astrophysical Journal, 734 (2011), p. L35

- J. Abadie et al., *A search for gravitational waves associated with the August 2006 timing glitch of the Vela pulsar*, Physical Review D, 83 (2011), p. 042001

- J. Abadie et al., *Calibration of the LIGO Gravitational Wave Detectors in the Fifth Science Run*, Nuclear Instruments and Methods, A624 (2010), pp. 223–240

- J. Abadie et al., *First search for gravitational waves from the youngest known neutron star*, Astrophysical Journal, 722 (2010), pp. 1504–1513

- J. Abadie et al., *Predictions for the Rates of Compact Binary Coalescences Observable by Ground-based Gravitational-wave Detectors*, Classical and Quantum Gravity, 27 (2010), p. 173001

- J. ABADIE ET AL., *Search for gravitational-wave inspiral signals associated with short Gamma-Ray Bursts during LIGO's fifth and Virgo's first science run*, Astrophysical Journal, 715 (2010), pp. 1453–1461

- B. P. ABBOTT ET AL., *Searches for gravitational waves from known pulsars with S5 LIGO data*, Astrophysical Journal, 713 (2010), pp. 671–685

- B. P. ABBOTT ET AL., *Search for gravitational-wave bursts associated with gamma-ray bursts using data from LIGO Science Run 5 and Virgo Science Run 1*, Astrophysical Journal, 715 (2010), pp. 1438–1452